PICOSECOND CATHODOLUMINESCENCE

THÈSE N^{O} 3206 (2005)

PRÉSENTÉE À LA FACULTÉ SCIENCES DE BASE

Institut de photonique et d'électronique quantiques

SECTION DE PHYSIQUE

ÉCOLE POLYTECHNIQUE FÉDERALE DE LAUSANNE

POUR L'OBTENTION DU GRADE DE DOCTEUR ÈS SCIENCES

PAR

Michele MERANO

laurea in fisica, Università degli Studi di Milano, Italie
et de nationalité italienne

acceptée sur proposition du jury:

Dr J.-D. Ganière, directeur de thèse
Prof. P. Buffat, rapporteur
Dr D. Le Si Dang, rapporteur
Prof. G. Mourou, rapporteur

Lausanne, EPFL
2005

Abstract

We have developed an original time resolved cathodoluminescence (TRCL) set-up with temporal performances similar to those of conventional time resolved optical techniques, keeping the capability to get structural information through the secondary electron mode of an electron microscope (SEM). This system allows for performing ultrafast spectroscopy on nanostructures leading insight into phenomena like transport, carrier capture and carrier recombination.

A traditional TRCL is based on the use of a SEM column equipped with an electrostatic beam blanking unit and a photon counting system for the detection. Electron pulses of rise and decay times $\sim$ 200 ps, varying width from 1ns to 1μs and a repetition rate up to 1 MHz are used for the excitation. Due to the long duration of the pulse compared to characteristic relaxation times, the system under investigation is set in a quasi-equilibrium state before the study of the luminescence decay. This leads to a non-straightforward interpretation of the temporal luminescence profile; moreover resolution is limited to 250 ps.

In order to overcome such limitations, we have replaced the thermionic electron gun of a SEM with a home-made ultrafast electron gun. Femtosecond mode-locked laser pulses are focused on a metal photocathode to create electron bunches. An extraction electrode and an anode accelerate photoelectrons up to 30 kV. The electron lens systems of the microscope column focus the photoelectron beam on the sample. Luminescence emitted as a consequence of the probe beam excitation is spectrally analyzed with a monochromator and it is then collected with a streak camera for temporal analysis.

This set up (picoCL) has achieved unprecedented combined spatial and temporal resolutions. The test for the spatial resolution is carried out on gold particles grown on a carbon substrate: a sample currently used to test commercial SEMs resolution. We prove that the ultrafast electron gun brightness is high enough to focus electrons on a probe diameter of 50 nm still having enough current to obtain a secondary electron image of the sample. The temporal width Δt of the electron pulses is measured by an indirect method. We compare the time resolved photoluminescence response (200 fs laser pulses excitation) of a semiconductor sample with that obtained with the picoCL. A Δt (FWHM) $= 12 \pm 1$ ps is found.

As a first study with the picoCL we investigate the time resolved luminescence emission from quantum structures located in InGaAs/AlGaAs tetrahedral pyramids. An $In_{0.10}Ga_{0.90}As$ quantum dot (QD) formed just below the top of the pyramid is connected to several types of low-dimensional barriers: InGaAs quantum wires (QWRs) on the edges of the pyramid, InGaAs quantum wells (QWs) on the (111)A facets and segregated AlGaAs vertical quantum wire (VQWR) and AlGaAs vertical quantum wells (VQWs) formed at the centre and at the pyramid edges.

PicoCL is successful in identifying the spectral features of the different nanostructures. Indeed the rise and decay times of their luminescence emissions vary strongly with the location of the excitation point on the pyramid. The intricate and complex carrier transport among the different quantum structures is enlightened: our results suggest the scenario that after excitation on the facet or on the edge of the pyramid, carriers diffuse towards the central structures (QD and VQWR) via the QWR. According to these findings we model the carrier diffusion along the QWR and fit our experimental data. A carrier mobility of 1300 cm^2/Vs is found.

Riassunto

Abbiamo sviluppato un originale strumento di catodoluminescenza risolta in tempo (TRCL), con una risoluzione temporale di 12 ps, e con la capacità al tempo stesso di ottenere informazioni sulla struttura del campione analizzato per mezzo dell'immagine a elettroni secondari di un microscopio elettronico a scansione (SEM). Questo sistema di spettroscopia ultrarapida permette di studiare fenomeni come il trasporto, la cattura e la ricombinazione dei portatori nelle nanostrutture a semiconduttore.

Un sistema di TRCL tradizionale sfrutta un'unità elettrostatica di "beam blanking" che viene inserita nella colonna di un microscopio elettronico. La detezione del segnale di luminescenza è fatta con un dispositivo per il conteggio di fotoni. Gli impulsi elettronici prodotti hanno tempi di salita e di discesa ~ 200 ps, durata compresa tra 1 ns e 1 μs e un tasso di ripetizione che può arrivare ad 1 MHz. Impulsi di questa durata, molto più lunga dei tempi di rilassamento caratteristici dei semiconduttori, forzano il campione in uno stato di quasi-equilibrio prima che lo studio del decadimento della luminescenza sia possibile. Questo rende particolarmente ostica l'interpretazione del profilo temporale della luminescenza; inoltre la risoluzione non può essere migliore di 250 ps.

Allo scopo di migliorare questi limiti abbiamo rimpiazzato il cannone termoionico di un SEM con un cannone eletronico ultrarapido che abbiamo sviluppato nel nostro laboratorio. Impulsi laser della durata di 200 fs sono focalizzati su un fotocatodo metallico. Un elettrodo di estrazione ed un anodo accelerano a 30 kV gli impusi elettronici cosí prodotti. Gli stessi sono focalizzati sul campione da analizzare per mezzo delle lenti elettroniche della colonna del microscopio. La luminescenza emessa a seguito dell'eccitazione operata dal fascio elettronico è analizzata spettralmente e temporalmente con un monocromatore e con una streak camera.

Questo strumento ha al tempo stesso una grande risoluzione spaziale e temporale. La risoluzione spaziale è stata testata su un campione di particelle d'oro cresciute su una matrice di carbonio: un campione normalmente usato per calibrare i SEMs commerciali. Siamo riusciti a dimostrare che la brillanza del cannone elettronico ultraveloce è grande a sufficienza da permettere di focalizzare gli elettroni su un diametro di 50 nm avendo ancora un'intensità di corrente che permette di ottenere immagini a elettroni secondari. La larghezza temporale Δt dell'impulso è misurata in modo indiretto. Abbiamo confrontato la fotoluminescenza risolta in tempo (200

fs di eccitazione laser) da un campione di GaN con la risposta ottenuta grazie alla picoCL. Troviamo per Δt un valore di 12 ± 1 ps (FWHM).

Come primo esperimento con la picoCL abbiamo studiato la diffusione e la ricombinazione dei portatori in piramidi di InGaAs/AlGaAs. Un quantum dot (QD) di $\mathrm{In_{0.10}Ga_{0.90}As}$ è cresciuto poco sotto il vertice della piramide ed è connesso con fili quantici (QWR) di InGaAs che corrono lungo gli spigoli della piramide, pozzi quantici (QW) di InGaAs che sono le pareti della stessa, un filo quantico verticale (VQWR) e pozzi quantici verticali (VQW) che si formano rispettivamente al centro e sugli spiogoli della piramide a seguito di segregazione di AlGaAs.

La picoCL ha successo nell'identificare le linee di emissione spettrale che corrispondono alle diverse nanostrutture. In effetti i tempi di salita e di discesa delle luminescenze variano fortemente in funzione del punto della piramide che viene eccitato. Il meccanismo di diffusione dei portatori nella piramide è messo in luce. A seguito di un'eccitazione su una faccia o su un bordo di una piramide, i portatori diffondono verso le strutture centrali (QD e VQWR) attrverso il QWR. Un modello di diffusione dei portatori lungo il QWR permette di fittare i nostri dati sperimentali. Ne risulta una mobilità di 1300 $\mathrm{cm^2/Vs}$.

Remerciements

En premier lieu, je tiens à remercier chaleureusement Jean Daniel Ganière, mon directeur de thèse, pour sa disponibilité et son soutien tout au long de ce travail. Je lui suis très reconnaissant d'avoir proposé le challenge de monter l'originale manip, sujet de cette thèse, et d'avoir partagé avec moi ses compétences techniques et ses connaissances scientifiques lors des longs entretiens suivant mes nombreuses intrusions dans son bureau.

Je remercie également Benoît Deveaud-Plédran pour m'avoir accueilli au sein de son laboratoire, pour son enthousiasme et ses extraordinaires compétences scientifiques. Benoît est un prof. spécial qui laisse beaucoup de liberté à ses doctorants et donne toujours des conseils vraiment précieux.

Un grand merci va aux trois post-doc: Pierre Renucci, Stéphane Collin et Andrea Crottini qui ont suivi mon travail de recherche pendent ces quatre ans. La collaboration avec eux a été très intense et c'est grâce à leur aide si j'ai pu obtenir des bons résultats. J'ai beaucoup profité de leur expérience au labo, et de leur aide pour préparer des conférences ou écrire des articles.

Ça a été un vrai plaisir pouvoir collaborer avec Samuel Sonderegger, Ferenc Fuzesi et Mondher Gatri qui ont développé une partie du set up. Ainsi que Pierre, Stéphane et Andrea ils sont devenus et ils vont rester des excellents amis.

Je ne veux pas oublier Nguyen Hoan et Jean Paul Hervé de la boîte OPEA (Paris), et nos techniciens Roger Rochat et Nicolas Leiser pour le support technique qui nous ont fourni. J'ai beaucoup apprécié leur disponibilité, leur expérience et leur savoir-faire.

Je considère une vraie fortune avoir eu la possibilité de faire mon doctorat à l'Institut de Photonique et d'Electronique Quantiques de l'EPFL. J'y ai trouvé en même temps une grande professionnalité et une ambiance fort amicale.

Finalement, je tiens à exprimer ma profonde reconnaissance à mes parents qui m'ont toujours soutenu au cours de ces années.

Contents

1 Introduction

Since the 1980's considerable effort has been devoted to the growth and characterization of semiconductor heterostructures of reduced dimensionality: quantum wires (QWRs) and quantum dots (QDs). Fabrication techniques of these structures have greatly improved with time, and the interest in their physical properties and their potential applications in novel optoelectronics devices has grown up. Today, nanostructures represent a very dynamic and rapidly developing research field of physics.

Semiconductor heterostructures are interesting for fundamental reasons. They can confine electrons to a region whose dimension is comparable to their de Broglie wavelength. In this way quantization effects are observable in the confinement direction. Quantum wires are used to confine electrons in a one-dimensional environment, quantum dots localize carriers in all three dimensions. In order to estimate the size of a nanostructure we have to evaluate the de Broglie wavelength [1]

$$\lambda = \frac{h}{\sqrt{3m_{eff}kT}} \tag{1.1}$$

where m_{eff} is the carrier effective mass and T is the solid temperature. For a semiconductor material, λ has a typical value of tens of nanometres at a temperature of a few K.

Among the possible applications of nanostructures, QDs have unique features that rend them potentially useful in quantum information processing [2]. At the moment promising scenarios for achieving quantum computation in a coupled quantum dot system have been proposed [3] and, even if none of the quantum computation schemes presented so far appear to be scalable to a larger number of coupled quantum bits in a straightforward way, this is a very active experimental and theoretical research field. Another important application for QD, also related to quantum information processing, is the generation of non-classical states of light such as single photon states [4]. Proposal to generate regulated single photons from a single quantum dot relies on electrical injection of single electron using resonant tunnelling [5], or carrier injection by non-resonant pulsed optical pumping [6].

Currently QDs or QWRs are not envisaged to replace the quantum wells semiconductor structures in traditional applications such as lasers, due to the large inhomogeneous size distribution (or size fluctuation for the QWRs) that is unavoidable with all growth techniques [2]. This aspect renders the single nanostructure characterization essential in understanding its basic physical properties and in testing its possible applications.

A complete characterization of a nanostructure involves the investigation of its structural, electronic and optical properties. Different experimental tools for testing the structure of a QD or a QWR are employed, we just cite direct imaging methods such as scanning tunnelling microscopy (STM), atomic force microscopy (AFM), transmission electron microscopy (TEM) and scanning electron microscopy (SEM). STM and AFM have in principle atomic resolution and, as well as SEM, are able to revel directly the morphology of a surface. TEM is used to inspect a nanostructure embedded in its nano-environment.

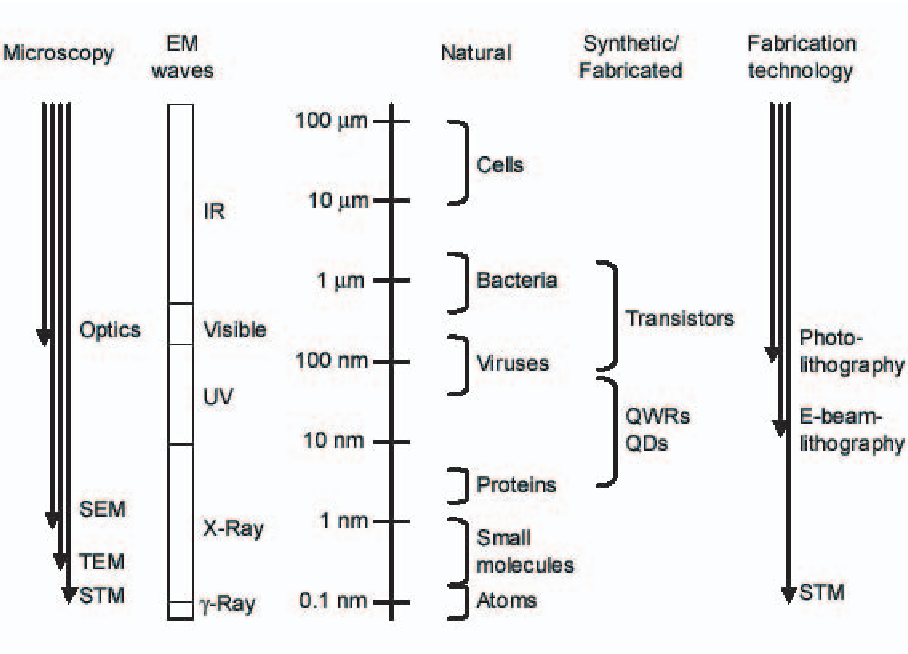

Figure 1.1: Down to the nanometric range: a perspective.

Electronic and optical properties of a single nanostructure are mainly studied with spectroscopic tools. Existing local luminescence probe techniques are: spatially localized micro-photoluminescence spectroscopy (μ-PL) using either strong focusing or masking; near-field optical microscopy (SNOM) to avoid the diffraction limitation of far-field optics; cathodoluminescence (CL), using focused energetic electrons in an electron microscope; and scanning tunneling luminescence (STL), using low-energy electrons injected or extracted from the tip of a STM [7].

The electron and hole states in a nanostructure are influenced by intrinsic properties like its size, its shape, the strain induced by the buffer over which it is grown. This implies that, for a reliable description of its electronic and optical properties, the probe used for investigation must provide also information on the nanostructure morphology. Quantum states of QDs and QWRs can also been influenced by extrinsic effects like impurities and structural defects of the crystalline matrix. More in general, it is not always possible to neglect the influence of the nano-environment on the heterostructures under investigation [1]. For all these reasons spatial resolution of the luminescence probe techniques is crucial.

Spectroscopic tools have additional unique strengths that make them capable of providing also fundamental information about non-equilibrium and transport properties of semiconductors. When combined with picosecond or femtosecond laser pulses, these techniques allow for studying the dynamics of carrier capture, energy relaxation and radiative recombination [8].

In this thesis we develop a new spectroscopic technique for characterizing semiconductor nanostructures. This system has at the same time a spatial resolution of tens of nanometres and a temporal resolution of 12 ps. It consists of an original time resolved CL set-up that combines spectroscopic strengths with spatial imaging techniques, to be a powerful tool for investigating phenomena related to relaxation and transport at the nano-scale level.

This thesis is organized as follow:

Chapter two discusses a traditional time resolved cathodoluminescence system. Performances of this technique are compared with those of our original set-up to highlight its specific properties.

Two chapters follow which provide a complete description of the set-up. *Chapter three* reports the design and the experimental test of the photoemission electron gun used for ultra-short pulses production.

Chapter four describes the installation of the picoCL set-up and its experimental performances evaluation.

In *chapter five* we report the results of the first study we performed with our system. We investigated InGaAs/AlGaAs pyramidal heterostructures. PicoCL is successful in characterizing the different nanostructures grown in one pyramid and it allows for describing the carrier transport in a system where QWs, QWRs and a QD coexist.

In *chapter six* we draw some conclusions.

2 Traditional TRCL

2.1 Introduction

This is a short chapter where we discuss the originality of the picosecond cathodoluminescence (picoCL) with respect to a traditional time resolved cathodoluminescence (TRCL) system. PicoCL performances are summarized.

2.2 Time resolved cathodoluminescence

In a traditional TRCL set up [9–19] a beam-blanking unit, located directly below the electron gun of a commercial SEM, is used to produce electron pulses (Fig. 2.1). A parallel plate capacitor scans the electron beam across a diaphragm. Pulses of rise and decay times $\sim$ 200 ps, varying width from $\sim$ 1 ns up to 10 μs, and a repetition rate of 1 kHz up to 1 MHz are obtained. The action of a blanking system determines an apparent movement of the electron gun crossover. Since the

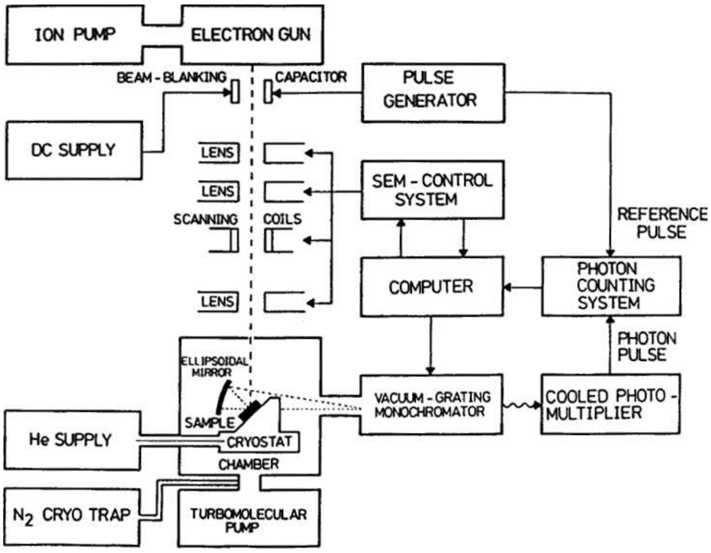

Figure 2.1: A traditional TRCL set up. Electron pulses are produced with a beam-blanking unit located directly below the electron gun.

final electron probe is a demagnified image of the crossover, the apparent movement of this one causes a shift of the electron probe on the specimen, which result in an increase of the effective probe size in the deflection directions. [20].

For instance in the Bimberg TRCL set up (the one reported in Fig. 2.1) the electron probe beam is always scanned over a small square of 7x7 μm^2 and the luminescence light presents a mean value of the properties of this area [21, 22]. Electron energies between 200 V to 40 kV at varying currents (10 pA to several nA) yielding intensities between 0.8 to 1800 W/cm^2 are used for excitation.

The vacuum system is modified and cryogenic shielding is introduced to suppress contamination of the samples at low temperatures. A continuous flow He cryostat is fitted to a standard specimen stage. The temperature is continuously variable in the range $5 \leqslant T \leqslant 300$ K.

The emitted light is focused by an elliptical mirror on to the entrance slit of a monochromator. The light is detected by a cooled photomultiplier with a GaAs cathode. The pulse generator, which triggers the beam-blanking unit, also triggers a photon-counting system via a delay line. The photon-counting system operates according to the method of delayed coincidence in an inverted mode, yielding an improved signal-to-noise ratio. The dynamic range of the detection system is 10^5.

The time resolution of a TRCL set up including photomultiplier and electronics is 250 ps. Due to the long duration of the electron pulse (1 ns at least), compared to characteristic relaxation times in semiconductors, the system under investigation is set in a quasi-equilibrium state before the study of luminescence decay. For this reason an interpretation of the time dependence of the luminescence intensity is not straightforward. All the information on the beginning of the excitation is indeed lost.

2.3 Picosecond cathodoluminescence: Performances

The originality of our picoCL with respect to a traditional TRCL set up resides in the way electron pulses are produced. A photoemission-based electron gun replaces the gun of a SEM. The photoelectric response of a large class of materials to a 200 fs laser excitation is very fast ($\leqslant$ 1 ps). In this way the excitation beam pulse width can be largely reduced. In the next two chapters we will give a detailed description of the picoCL system we mounted in our lab. We will show that the main performances of the system are:

- A spatial resolution of 50 nm in the secondary electron imaging mode
- A temporal resolution of ~10 ps
- Possibility of working in the spot mode of the SEM

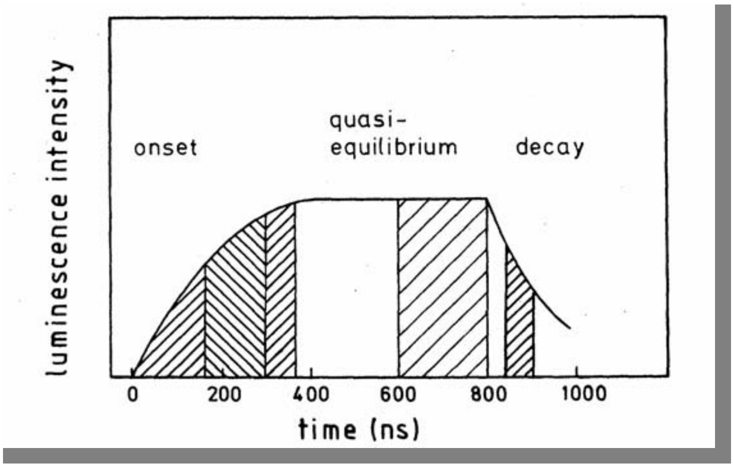

Figure 2.2: Cathodoluminescence response to 800 ns electron pulse. A “straightforward” interpretation of decay time is dubious if the system under investigation is not a two-level system.

- A spectral resolution of 1 meV
- NIR – UV spectral range
- 90 K – 300 K temperature range. (10 K – 300 K temperature range within one year).

3 High Brightness Picosecond Electron Gun

3.1 Introduction

Laser driven picosecond electron guns have current applications in many research fields. A picosecond or femtosecond laser pulse is used to create an electron pulse with a comparable time duration. Photoelectrons are then accelerated and focused by a suitable electron optical system.

Picosecond electron pulses are used in ultrafast electron diffraction (UED) to study the evolution of nuclear motions in chemical and photobiochemical reactions [23] [24] [25]. In general, the reaction is clocked by an initial fs laser pulse and the induced ultrafast structural changes are probed with an electron pulse. In UED fs laser pulses are generated from an amplified Ti: sapphire laser system and focused onto a back-illuminated gold or silver photocathode. An electron pulse width of some ps is obtained. The number of electrons per pulse is typically 25000 with a repetition rate of 1 kHz. Electrons are accelerated at 30 kV and are focused by a magnetic lens assembly.

A similar electron gun is used also for ultrafast reflection high-energy electron diffraction (RHEED) [26] [27] [28]. A picosecond laser pulse is split into two beams. The first interacts with the sample under study. The second activates the cathode of an electron gun creating a collimated and focused electron beam that probes the sample surface structure and temperature at different delay times.

The accelerator and FEL (Free Electron Laser) communities have considered laser driven electron guns for use as photoinjectors [29] [30]. The drive laser for the Los Alamos Advanced FEL is made of a Nd:YLF oscillator mode-locked at 108.33 Mhz and a double-pass amplifier. A Pockell cell switches out variable length macropulses to be frequency quadrupled by using a LBO crystal followed by a BBO crystal. A typical 10 μs macropulse consist of 1080 micropulses, each 7-14 ps in duration. Typical operations require 1-3 nC of charge per micropulse. The acceleration optical system consists of a high gradient radio-frequency linear accelerator capable of accelerating electrons to a maximun energy of 25 MeV. Many different photocathodes have been used as electron sources for FELs and other electron accelerator systems; K_2CsSb and Cu are the most successful.

Attempts to use picosecond electron guns in new research fields have been carried out also. An interesting example is a picosecond photoelectron scanning electron microscope for high-speed testing of integrated circuits, that was developed in IBM research center in 1987. This system, conceived as a tool for measuring high-speed electrical waveforms on circuits, replaced the electron gun of a SEM with a pulsed laser/photocathode combination. A temporal resolution of 5 ps and a spatial resolution of 0.1 μm was declared [31].

3.2 Electron gun requirements

As a first step towards picosecond CL, we designed and mounted a laser driven electron gun prototype. Three main objectives were envisaged:

- A gun brightness of the order of 10^3 A/cm^2 sterad. This corresponds to a probe current of 10 pA ($\sim$ 1 electron per pulse) with a probe diameter of 50 nm.
- An electron pulse width of 10 ps.
- A high repetition rate (80.7 MHz) for fast luminescence detection with a streak camera system.

The electron optical properties of our electron gun and the electron pulse width produced are the two main subjects of this chapter.

3.3 Electron gun description

Our high brightness picosecond electron gun is shown in Figure 3.1. The photocathode (C) is a gold film, 20 nm thick, deposited on a quartz window by conventional evaporation techniques. It is used in transmission mode operation. A circular pinhole (P) of 1 mm diameter located 2.5 mm from the cathode is used as an extraction electrode and is followed by the anode (A) at a distance of 15 mm. The electron gun is mounted in a vacuum chamber at a pressure of 10^{-6} mbar.

The laser system used for the generation of picosecond electron pulses consists of a pump laser, a mode-locked laser, and a frequency harmonic generator. The pump (VERDI- Coherent) is a solid-state, diode-pumped, frequency doubled Neodymium Vanadate (Nd:YVO4) laser that provides single-frequency green (532 nm) output. A femtosecond Ti:Sapphire mode-locked laser (MIRA-Coherent) is used to produce 200 fs light pulses with a repetition rate of 80.7 MHz. The MIRA is tunable in the wavelength range between 710 to 1000 nm. We operate it at 800 nm where its operating conditions are particularly stable.

Infrared radiation is first doubled (LBO-crystal) and then tripled (BBO-crystal) in a Frequency Harmonic Generator system (SHG/THG-Inrad). The FHG provides

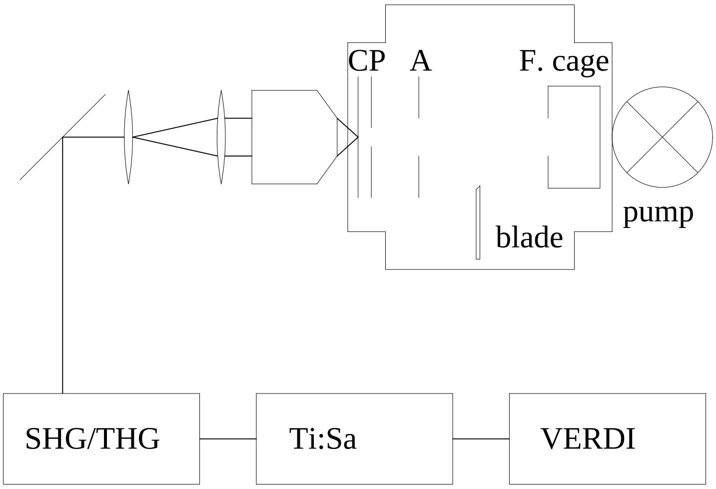

Figure 3.1: High brightness picosecond electron gun.

0.6 nJ, 200 fs pulses at 266 nm. The UV light goes through a beam expander and is focused on the cathode surface with a microscope objective. The spot size (defined as the radius at which the intensity drops by the factor $1/e^2$) is 2.5 μm. A sapphire window, ensuring a good vacuum, is placed between the objective and the photocathode.

3.3.1 Photocathode

The photocathode choice was the first technical problem to be addressed. Normally the photocathode material for an high brightness electron source is either a simple metal (Au, Ag, Cu, Y, Ba, Sm, Mg) or a semiconductor (K_2CsSb, Cs_3Sb, GaAs, CsI, Cs_2Te) [29]. The relevant properties that characterize the cathode of the picosecond CL are: spectral response, quantum efficiency, operational lifetime, temporal response, damage threshold, energy distribution of the emitted electron beam and air transferability. Pure metal photocathodes seem to be better candidates for our set-up because of high damage threshold, large free electron density, almost instantaneous time response and the ease of preparation [32]. The main problem for semiconductor photocathodes is that they are very sensitive to contamination. They require ultra high vacuum conditions while metals works well at a pressure of 10^{-6} torr. Gold has the advantage that is transferable in air without problems, and has a work function ($\Phi = 4.3$ eV) well suited for our laser system.

The thickness of the gold film is a compromise between quantum efficiency and roughness. Photocathodes of 20 nm have a good quantum yield and are rugged enough to withstand many days of operation [27]. Once the photocathode is

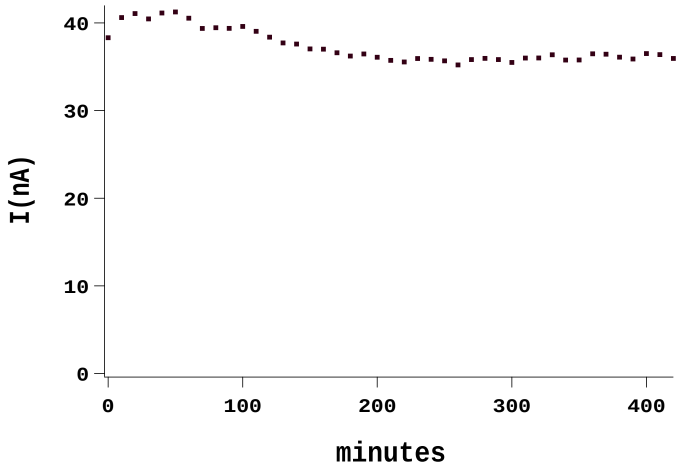

Figure 3.2: Aging test.

mounted in the vacuum chamber it can be exposed to UV radiation. Initially the current produced for a constant amount of light increases over the time. To activate the cathode the surface is irradiated with 266 nm radiation for several hours [33]. After the activation process, as long as the cathode remains under vacuum, his quantum efficiency is reproducible for days of operation. In Figure 3.2 an aging test for the gold cathode is reported. We focused 48 mW of UV radiation onto the cathode for several hours. The cathode was biased at –1 kV, the pinhole and the anode being grounded. The stability of the emitted current is rather good. A quantum efficiency η of 3.8 10^{-6} is obtained. Published quantum efficiency data for gold cathodes, tested with ultraviolet laser pulses in reflection mode operation, report values of 4.7 10^{-5}. Considering the fact that we are working in transmission mode and we have a 10 % UV transmission through our gold film, our result is in good agreement with previously performed experiments.

3.3.2 Photoelectron energy dispersion

As a consequence of the photoemission effect, electrons leave the cathode with different energies. It is very important to estimate this initial energy dispersion because it limits the brightness of the source and induces chromatic aberrations that are very difficult to correct in electron optics. The main hypothesis, that succeeds in explaining near threshold photoelectric experiments for metals, is that the number of electrons emitted per quantum of light absorbed is to a first approximation proportional to the number of electrons, per unit volume of the metal, whose kinetic energy normal to the surface augmented by hν is sufficient to overcome the potential barrier at the surface [34]. If we neglect the variation of the barrier transmission coefficient for electrons of different velocity and the possibility that they can be scattered before reaching the surface we find an energy distribution given by [35]

$$n(E)dE \propto \frac{EdE}{\exp\{(E - h\nu + \Phi)/kT\} + 1} \tag{3.1}$$

where E is the photoelectron kinetic energy. A plot of $n(E)$ for a temperature T= 300 K is given in Figure 3.3. A mean electron energy $\overline{E} = 0.25$ eV is found with a standard deviation $\sigma = 0.09 \sim 0.1$ eV.

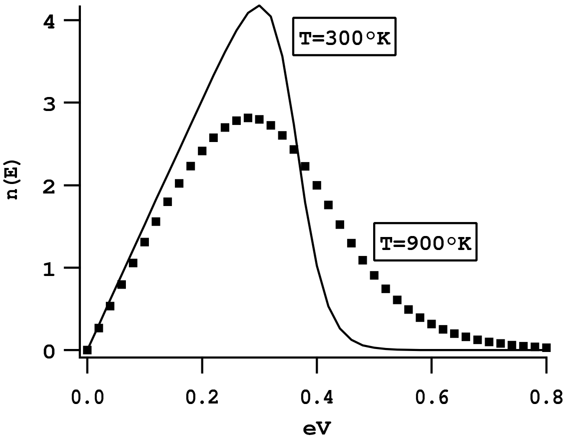

Figure 3.3: Photoelectron energy distribution for two different temperatures. The two distributions are normalized.

In general we focus up to 50 mW of UV radiation on the gold cathode. The correct temperature to be considered for the electron energy distribution is difficult to estimate. Anyway it is easy to show that σ doesn't vary too much with T in the range $300 \leqslant \mathrm{T} \leqslant 1340$ K where 1340 K is the gold melting point. In fig. 3.3 $n(E)$ is reported also for a temperature of T = 900 K. In this case we have $\overline{E} = 0.30$ eV and $\sigma = 0.1$ eV. At T = 1200 K we find $\overline{E} = 0.34$ eV and $\sigma = 0.11$ eV Considering the fact that the gold melting point is 1340 K and we do not see any damage on the cathode surface even after several hours of exposure we can confidently choose $\sigma = 0.1 \pm 0.01$ eV. We will see that this error in estimating the correct σ will be negligible for us.

3.4 Optical properties

3.4.1 Refraction index

It is well known that, in ray optics, light obeys the Fermat's principle, i.e. the time of transit t for travelling from a point D to a point D' must be an extremum. In more precise mathematical terms, the variation of the line integral

$$t = \int_{D}^{D'} \frac{\overline{n}}{c} ds \tag{3.2}$$

where the refractive index n is usually defined as $\overline{\mathrm{n}} = \mathrm{c}/\mathrm{v}$ i.e. the ratio of the velocity in vacuum c and the phase velocity v, must vanish. On the other hand, electrons obey the Maupertuis's principle of least action. For conservative forces, the action I is given by the line integral of the momentum p of the particle along its path s.

$$I = \int_{D}^{D'} p \, ds \tag{3.3}$$

A comparison of Fermat's and Maupertuis's principles suggests that the path of the electron is identical with the path of a wave if $\overline{n} \propto p$. We can introduce, in analogy with light optics, an electron optics index of refraction $n \propto p$. Choosing the potential V to be zero when $p = 0$ we have, for non relativistic electrons $n \propto \sqrt{V}$. We can restrict ourselves to the non-relativistic situation because the maximum V for our system is 30 kV (see below).

3.4.2 Crossover

We will suppose now that the photocathode is grounded while the pinhole and the anode are at positive potentials $\mathrm{V_P}$ and $\mathrm{V_A}$ respectively. In this section the C-P distance will be α and the P-A distance will be β (Fig. 3.4). The electric field in the C-P region will be $\mathrm{E_1} = -\mathrm{V_P}/\alpha$ and in the P-A region $\mathrm{E_2} = (\mathrm{V_P} - \mathrm{V_A})/\beta$. Electrons will be supposed to have all the same initial energy $\overline{E}$. For reasons that will be clear later the pinhole is used in order to create a high electric field (1 kV/mm at least) in the cathode proximity, to have $\mathrm{eV_P} \gg \overline{\mathrm{E}}$.

For optical considerations we can divide the system in three parts: the region in which electrons experience a constant electric field $\mathrm{E_1}$, the pinhole and the region at constant field $\mathrm{E_2}$. In the pinhole proximity the electric field is inhomogeneous and contains a radial component. It can be shown [36] that the pinhole is equivalent to a thin lens of focal length

$$f = \frac{4V_P}{E_1 - E_2} \tag{3.4}$$

immersed in a medium with refractive index $\mathrm{n} = \sqrt{\mathrm{V_P} + \overline{\mathrm{E}}/\mathrm{e}} \sim \sqrt{\mathrm{V_P}}$.

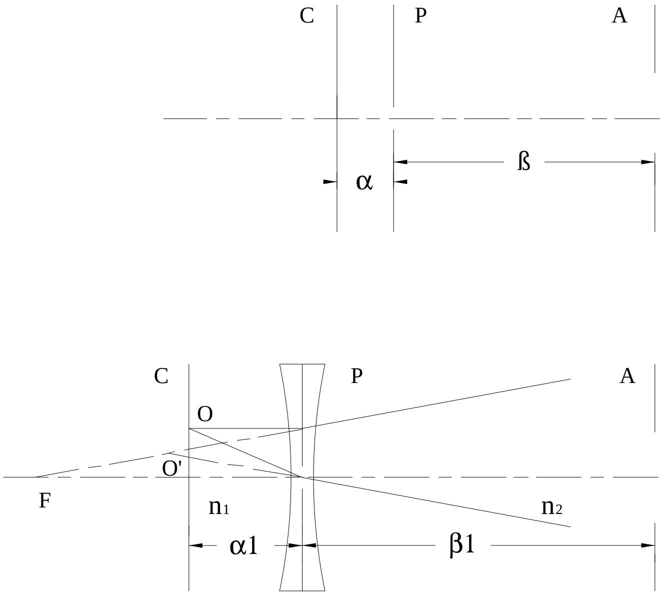

Figure 3.4: O' is the image of the point object O. The focal point F is placed at a distance $\mathrm{f}\frac{\mathrm{n_2}}{\mathrm{n_1}}$ from the pinhole. The ray from O directed towards the centre of the lens forms an angle θ with the axis. Its angle after been deviated is $\theta\frac{n_1}{n_2}$. The thin lens is divergent because in general $|E_1| > |E_2|$.

The two acceleration regions are very easy to treat as well. Consider two plane electrodes D, F parallel to each others (Figure 3.5). Their distance will be s. Electrode D is at potential $\mathrm{V_1}$ while F is at potential $\mathrm{V_2}$. (You can think for instance to the pinhole P and the anode A.) Let O be the position of an electron in the proximity of D. Its velocity is $\mathrm{v} = \sqrt{2\mathrm{eV_1}/\mathrm{m}}$. Its trajectory makes an angle θ with the normal to D. It is easy to show that, in the paraxial approximation, electrons from O arrive in F as if they were travelling in a region of constant potential, from a point O' placed on the normal-to-the-electrodes from O, at a distance $\mathrm{s_1}$ from F.

$$s_1 = \frac{2s}{1 + \sqrt{\frac{V_1}{V_2}}} = \frac{2s}{1 + \frac{n_1}{n_2}} \tag{3.5}$$

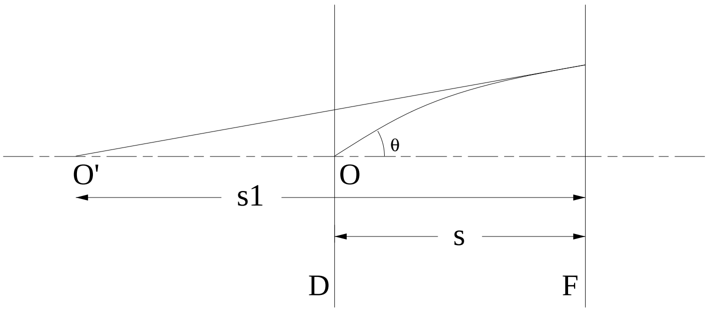

Figure 3.5: In paraxial approximation and for monochromatic electrons, a region of constant electric field is stigmatic. All electrons from O “seem” to arrive in F from a common point O’.

The acceleration region between D and F can be considered as a region of constant refractive index $n = \sqrt{V_2}$ (or null electric field) with the electrode D placed at a distance s_1 from F.

It is now possible to describe the optical properties of the picosecond electron gun (Figure 3.4). It consists of a thin lens placed between two mediums with different refractive indexes; $n_1 = \sqrt{V_P}$ and $n_2 = \sqrt{V_A}$ respectively. According to formula (3.5) the distance between the anode and the thin lens is given by

$$\beta_1 = \frac{2\beta}{1 + \frac{n_1}{n_2}} \tag{3.6}$$

and the distance between the thin lens and the cathode is

$$\alpha_1 = \frac{2\alpha}{1 + \sqrt{\frac{\overline{E}/e}{V_P}}} \simeq 2\alpha \tag{3.7}$$

The cathode virtual image position is placed at a distance d from the anode given by

$$d = 2\alpha \frac{n_2}{n_1} M + \frac{2\beta}{1 + \frac{n_1}{n_2}} \tag{3.8}$$

where the lateral magnification M is:

$$M = -\frac{f}{2\alpha - f} \tag{3.9}$$

Plots of f, d and M are reported in Figure 3.6. We choose $\alpha = 2.5$ mm, $\beta = 15$ mm and two different values for V_P; 2.5 and 7.5 kV respectively. V_A varies from 2.5

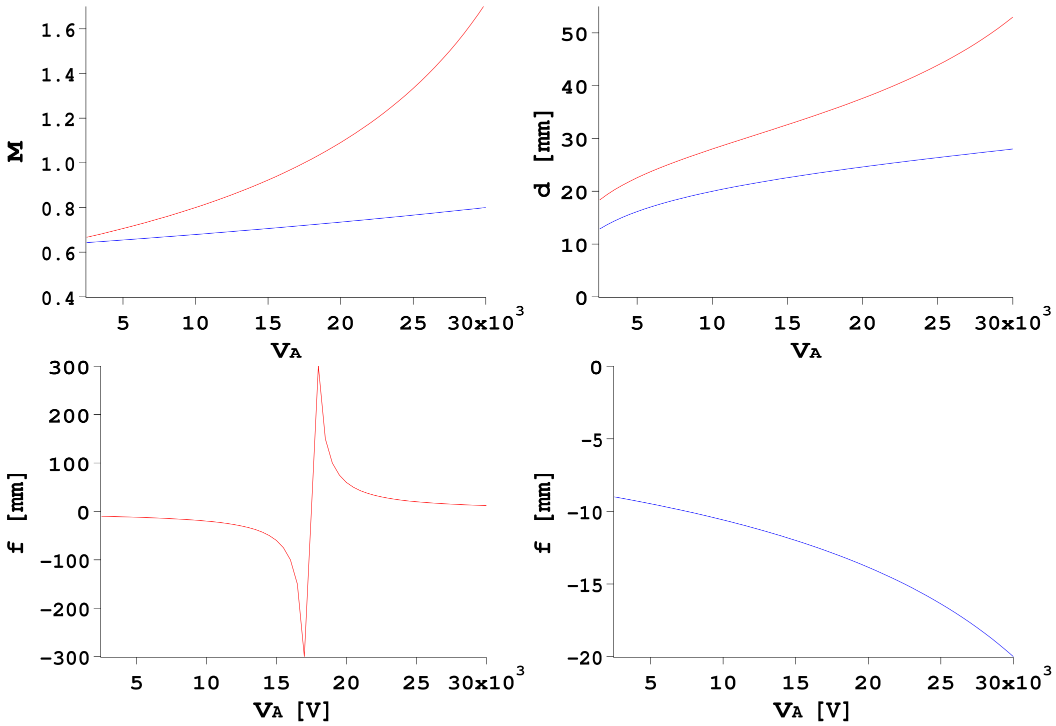

Figure 3.6: Red: $\mathrm{V_P}$ =2.5 kV, blue: $\mathrm{V_P}$ =7.5 kV. The magnification (M), the cathode virtual image position (d), and the focal length (f) of the picosecond electron gun are reported as a function of the anode potential.

kV to 30 kV (The maximum acceleration potential for our electron microscope). A potential $\mathrm{V_P}$ =2.5 kV correspond to an electric field of 1 kV/mm in the C-P region. For $\mathrm{V_A} \geqslant 17.5\mathrm{kV}, |\mathrm{E_2}| \geqslant |\mathrm{E_1}|$, and the focal length f pass from negative to positive. A potential $\mathrm{V_P}$ =7.5 kV correspond to an electric field of 3 kV/mm in the C-P region. In this case $|\mathrm{E_1}| > |\mathrm{E_2}|$ for $2.5 \leqslant \mathrm{V_A} \leqslant 30\mathrm{kV}$.

3.4.3 Brightness

With the aim of measuring the gun brightness, we examined the electron beam profile after the anode. Electrons, freely expanding in the vacuum chamber, were collected in a Faraday cage (Fig. 3.1). By cutting the beam with a blade and plotting the measured current derivative as a function of the blade displacement, we obtained the beam profile (Fig. 3.7) The blade was placed in the middle of the vacuum chamber, at a distance $d = 106$ mm from the cathode. For 27 nA extraction current, the cathode at −1 kV, pinhole and anode at ground, and a laser spot size of 2.5 μm we found a gaussian beam with a radius $R_b = 6.5$ mm.

An important parameter for electron microscopy is axial brightness. Only electrons leaving the centre of the source with a little angle of emission are relevant. If we assume that the current density j at the cathode surface has the same Gaussian profile than the laser beam,

$$j = I_0 \frac{1}{2\pi\sigma^2} \exp - \frac{2\rho^2}{R_l^2} \tag{3.10}$$

where I_0 is the total current and R_l the laser radius, the fraction of electrons emitted from a disk of radius $r \ll R_l$ in the centre of the active region is $2\frac{r^2}{R_l^2}$. We consider now a little disk of radius $r' \ll R_b$ placed on the axis of the vacuum chamber at the blade level. The fraction of electrons, propagating in the solid angle $\Delta\Omega = \pi\frac{r'^2}{d^2}$ defined by r', are $2\frac{r'^2}{R_b^2}$. Axial brightness is given by the number of electrons emitted from the disk of radius r per unit surface per unit solid angle:

$$\beta = I_0 \cdot 2\frac{r^2}{R_l^2} \cdot 2\frac{r'^2}{R_b^2} \cdot \frac{1}{\pi r^2} \cdot \frac{d^2}{\pi r'^2} = \frac{4 I_0 d^2}{\pi^2 R_b^2 R_l^2} \tag{3.11}$$

This formula is not totally correct. The optical source rather than the physical source of the electron gun must be considered. Using formula 3.8, with $\mathrm{V_C} = 0$ V, $\mathrm{V_P} = \mathrm{V_A} = 1$ kV, we find $\mathrm{d} = \beta + \frac{4}{3}\alpha$. For our system the optical source is placed behind the cathode at a distance $\frac{1}{3}\alpha$, where α is the cathode-pinhole distance. The linear magnification M is $\frac{2}{3}$. The effective radius of our electron source is then $\frac{2}{3}R_l$ and so brightness must be multiplied by $(3/2)^2$. For 1kV acceleration voltage the brightness of our laser driven electron gun is 93 A/cm^{2}sterad.

The maximal possible brightness β_{th} for an electron gun was given by Langmuir

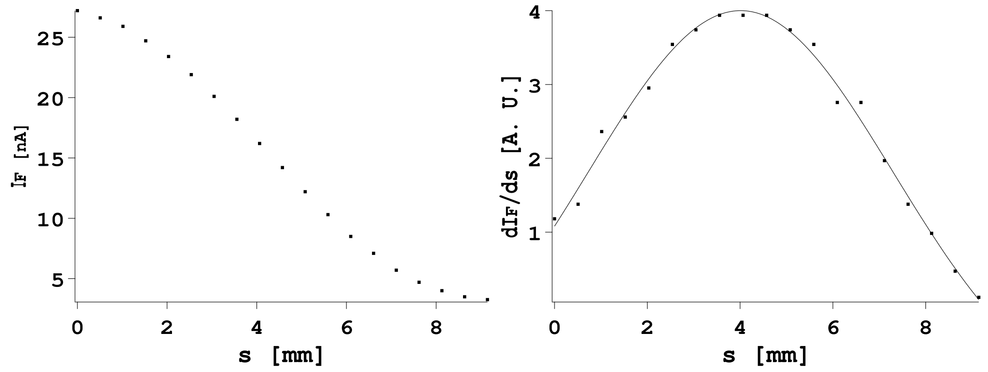

Figure 3.7: Right: electron current ($\mathrm{I_F}$) collected by the Faraday cage as a function of the blade displacement (s). Left: the beam profile. Dots are experimental values, the line is a gaussian fit.

[37] as

$$\beta_{th} = \frac{jV}{\pi \Delta V} \tag{3.12}$$

where j is the source current density, V the acceleration voltage and ΔV is the initial photoelectron energy spread divided by the electron charge. As we saw in section 3.3.2 the correct value for $e\Delta V$ is 0.1 eV. A discrepancy between the theorical brigthness $\beta_{th} = 2.9 \cdot 10^2$A/cm^{2}sterad and the measured one suggests that we are facing space charge effects.

The formula (3.12) is very general and does not depend on the optical system employed. In particular the linear relation between brightness and acceleration voltage is good as long as relativistic corrections can be neglected. By varying the cathode potential we tried to verify experimentally this linear relation. In Fig. 3.8 brightness is reported as a function of the acceleration voltage. The measurements were performed for two different laser spot sizes; $\rho = 2.5$ and 18 μm. The acceleration voltage is limited to –2.5 kV because, when we performed such a measurement, we were not equipped with a high voltage generator.

Electron guns brightness are usually reported for an acceleration voltage of 20 kV. From Eq. (3.12) the axial brightness of our laser driven electron gun at 20 kV is $\beta = 1.8 \cdot 10^3$ A/cm^{2}sterad. This value is 100 times less than the brightness of a thermionic electron gun ($(0.2 - 1) \cdot 10^5$ A/cm^{2}sterad) [20]. Modern SEMs with a thermionic electron gun can achieve a spatial resolution of 3 nm. It means that the electron beam can be focused on the sample over a spot diameter $d_p \leqslant 3$ nm still having enough current to obtain a clear image. With our gun we can have in principle the same current in a spot 10 times bigger, which means a spatial resolution of 30 nm. We have a confirmation of this by evaluating the probe current with the formula that relates it to brightness

$$I_p = \beta \cdot \pi^2 \cdot \frac{d_p^2}{4} \cdot \theta^2 \tag{3.13}$$

where θ is the probe aperture angle. Typical values for θ are between 5 and 20 mrad. Choosing $\beta = 1.8 * 10^3$ A/cm^{2}sterad, θ=10 mrad, $d_p = 30$ nm, it gives an I_p of 4 pA still sufficient to have a secondary electron image. Such a current correspond to 0.3 electrons per pulse.

Until now we have considered the continuous brightness β. Indeed we intend to use the standard Everhart-Thornley secondary electron detector mounted on a commercial SEM in order to obtain secondary electron images. Such a detector operates in continuous mode so β is the relevant parameter. Anyway, since we are working with pulses, it seems interesting to us to give the brightness per pulse $\beta_{pulse} = \beta/\nu\tau$ also. With $\nu = 80$ MHz the repetition rate of our laser system

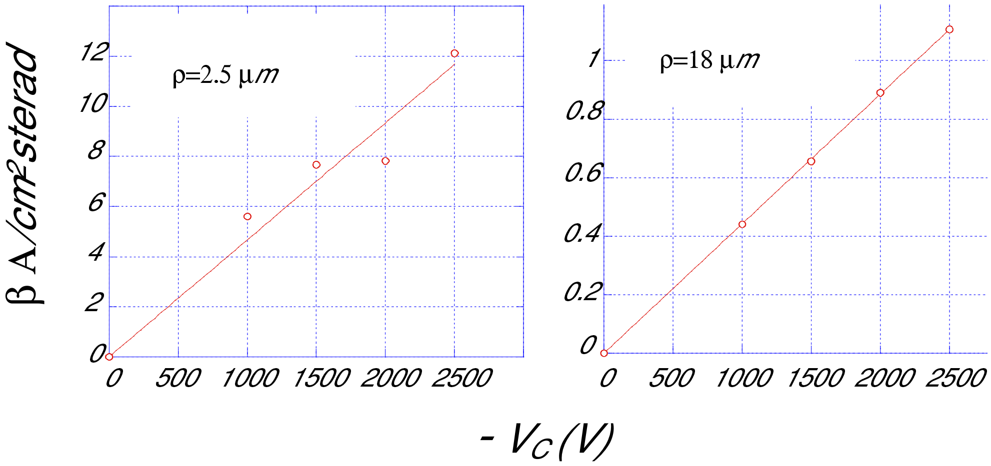

Figure 3.8: Brightness vs. acceleration potential.

and $\tau = 12$ ps the estimated electron pulse temporal width (see below) we obtain $\beta_{pulse} = 1.8 \cdot 10^6$ A/cm^{2}sterad.

3.4.4 Space charge effects

In the previous section we compared the measured brightness with the maximal theoretical brightness. A discrepancy between the two values is clear evidence that Coulomb repulsion between electrons is not negligible. Electron interactions are most relevant in the cathode proximity, where the linear dimensions of our electron pulses are small and particles are slow. Space charge effects are annoying because they are a main cause of electron pulse broadening.

We tried to investigate how much Coulomb repulsion affects brightness. We measured the electron beam radius ($\mathrm{R_b}$) at the centre of the vacuum chamber, for different laser spot sizes ($\mathrm{R_l}$) on the cathode. Results are reported on Fig. 3.9 (left). If we neglect space charge effects we expect that $\mathrm{R_b}$ increases with $\mathrm{R_l}$. Instead we observe that, for $\mathrm{R_l} < 50$ μm, $\mathrm{R_b}$ increases when $\mathrm{R_l}$ decreases. We attribute this broadening to space charge effects.

In Fig. 3.9 (right) brightness is reported as a function of the laser spot size. It is evident that although electron Coulomb interactions are not negligible, brightness still increases as $\mathrm{R_l}$ decreases. In the measures reported here we passed from a $\mathrm{R_l} = 4$ μm and a photocurrent $I_C = 22$ nA to a $\mathrm{R_l} = 190$ μm and a $I_C = 34$ nA. In Fig. 3.9 (bottom) brightness has been renormalized for a constant current $I_C = 22$ nA. Dots are the renormalized data. According to formula 3.11 brightness is expected to scale as $\frac{1}{R_l^2}$. Markers (black) are the result of a fit scaling as $\frac{1}{R_l^2}$. It is

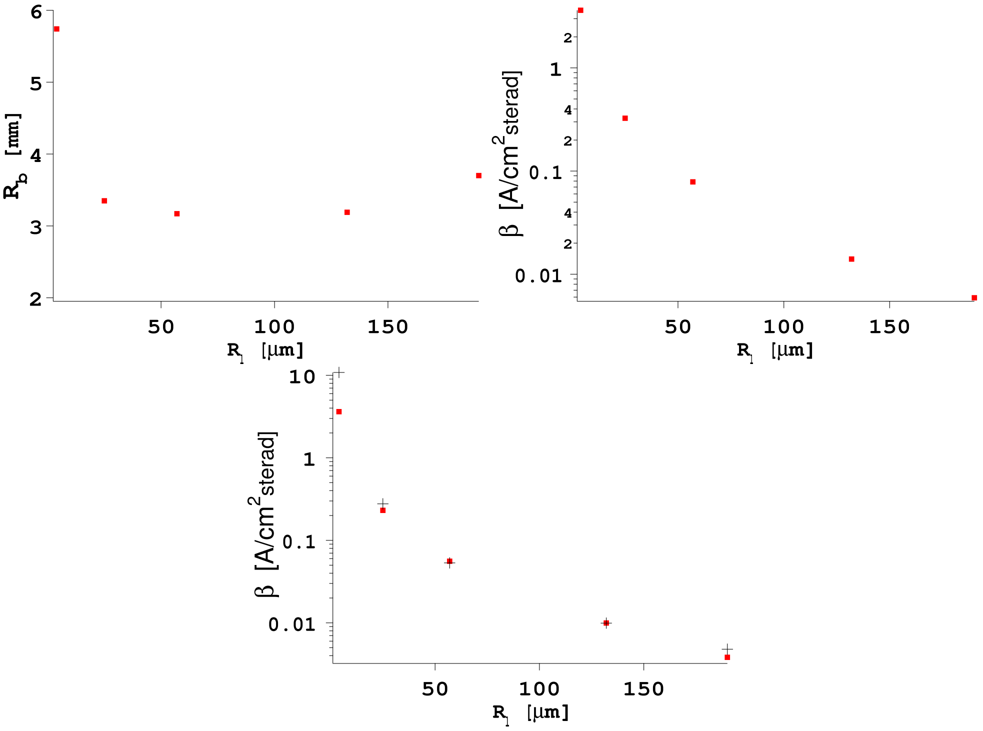

Figure 3.9: Theoretical (black markers) and experimental (red dots) gun brightness as a function of the laser spot size on the cathode.

evident from the figure that for little R_l brightness increases less than the $\frac{1}{R_l^2}$ law expected if the Coulomb repulsion is totally negligible.

3.5 Pulse width

The temporal width of the electron pulses was measured by an indirect method. The electron beam was focused over a semiconductor material and the cathodoluminescence signal was collected with a streak camera. We compared the time resolved cathodoluminescence (TRCL) emission, produced by electron pulses of unknown temporal width, with the time resolved photoluminescence (TRPL) signal obtained with 200 fs laser pulses. To perform this experiment we modified the set-up employed for the aging and brightness tests (Fig. 3.10). A sample support was mounted in the middle of our vacuum chamber at 45 degrees with respect to the incident electron beam. The electron pulses were focused by an electrostatic lens placed after the anode. A lens (L_1 f = 20 cm) collimated the luminescence signal that was focused on the streak camera with a 31 cm focal-length lens (L_2).

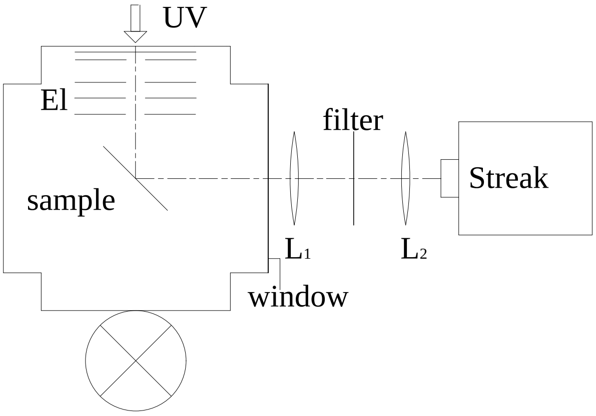

Figure 3.10: Pulse width set-up. The electrostatic lens is indicated by El.

A filter was inserted in the light beam path in order to stop the residual laser light.

3.5.1 Electrostatic lens

The lens we used to focus the electron beam was a saddle-field lens. It consisted of three circular electrodes, 2 mm thick, with a circular central aperture of diameter $\phi = 2$ mm. The distance between the first electrode and the pinhole was 1 mm and the distance between two consecutive electrodes was 1 mm also. The cathode was placed at a negative potential, pinhole, electrode 1 and 3 were at ground. In this configuration electrode 3 took also the place of the anode. The electron velocity, outside the lens, is given by the potential V_C of the cathode. Inside the lens, electrons are initially accelerated or decelerated according to the choice of the potential V_2 of the inner electrode, but in both cases a converging lens is obtained [36].

The first step towards the realization of this electrostatic lens was a modelling with an ion optics program (SIMION). Such a program allows for computing the potential field produced by the electrodes and then the electrons path. The potential distribution in space is completely defined by the geometry and the potentials of the electrodes. It can be calculated from Laplace differential equation $\nabla^2 V = 0$. Though the analytical calculation of the potential distribution for a given electrode configuration is impracticable in many cases, SIMION performs a complete numerical computation by a relaxation method. (A description of it can be found in electron optics manuals [36] [38].) It is important to remind here that given a certain number of conductors at different potentials, all enclosed in a conducting shell, the Uniqueness theorem guarantees that the electric field is determined throughout the system. Moreover a general state of this system can be analyzed

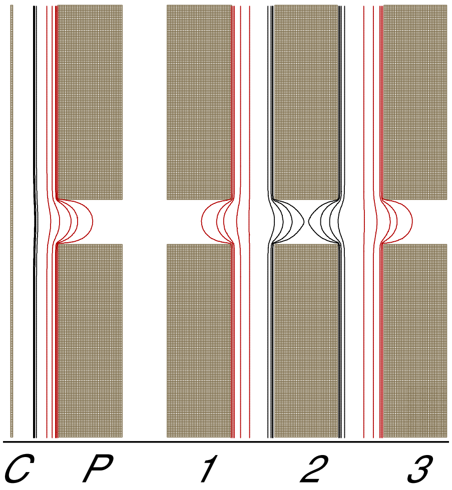

Figure 3.11: Equipotentials for the electrostatic lens computed by SIMION. C is at –2500 V, electrode 2 is at –1385 V, electrodes 1, 3 and P are at earth. Red: -600, -300, -100, -50, -10 V equipotentials. Black: -1200, -1300, -1350, -1370 V equipotentials.

as the superposition of states in each of which all conductors but one are at zero potential [39]. After having obtained an exact potential plot of the investigated electron lens, we know the refractive index variation in the space. It is then simple to compute the electron trajectories with a numerical ray tracing method. The system was simulated with SIMION for an acceleration potential of –1 kV and -2.5 kV. We found that electrons were focused at the centre of the vacuum chamber for V_2 equal to -558 V and to -1428 V. The simulated spot sizes were respectively 180 μm and 100 μm.

Finally we fabricated and mounted the lens. An experimental test of the lens was carried out as well. Using the blade and the Faraday cage we found optimal focusing for V_2 = -554 V and -1385 V respectively and spot sizes of 279 μm and 178 μm. While the simulated value of V_2 are in good agreement with the experimental values, the spot sizes are not. The mainly reason is that in our simulation we considered monochromatic electrons and we did not take account of chromatic aberrations.

3.5.2 Pulse width measurement

The semiconductor specimen was GaAs:Si with an impurity concentration of $10^{19}/\mathrm{cm}^3$. It was mounted in the middle of the vacuum chamber at 45° with respect to the electron beam direction. The cathodoluminescence signal was collected at 90° and directed towards the streak camera by the lens collecting system. The acceleration potential for the electrons was chosen to be 2.5 kV. In the same experimental configuration we directly focused the femtosecond laser pulses over the sample and we obtained the time resolved photoluminescence signal also. Experiments were carried out at room temperature. We observed that the TRCL and the TRPL signals had different rise times and the same decay time of 16 ps (defined as the time for the intensity to drop of a factor $1/e$).

We can regard the TRPL signal as the response of the system to a δ of Dirac excitation (200 fs). It is then possible to obtain the pulse width of the electron beam as the deconvolution of the TRCL signal with the TRPL one. A very good fit of the photoluminescence spectrum is given by the convolution

$$h(t) = A \cdot g_1(t) * f(t) \tag{3.14}$$

of a Gaussian $g_1(t)$ with a full width half maximum (FWHM) of 6 ps and an exponential $f(t) = Exp(-t/16)$. The TRCL is fitted with

$$y(t) = B \cdot g_2(t) * f(t) \tag{3.15}$$

where $g_2(t)$ is a Gaussian of FWHM = 16 ps and, $f(t)$ the same exponential used previously (A and B are normalization factors). In the frequency domain the deconvolution is simply given by

$$x(\nu) = \frac{y(\nu)}{h(\nu)} = \frac{A \cdot g_1(\nu) \cdot f(\nu)}{B \cdot g_2(\nu) \cdot f(\nu)} = \frac{A}{B} \cdot g_3(\nu) \tag{3.16}$$

where $g_3(\nu)$ is a Gaussian function. The Fourier transform of $x(\nu)$ is still a Gaussian of FWHM = 14.8 ps. We identify it with the pulse width of our electron excitation.

Several causes contribute to the temporal broadening (Δt) of the electron beam. It is well known that the photocathode time response ($\Delta t_1 = 100$ fs) is not relevant at the time scale we are concerned. The Δt_2 due to initial energy spread is only relevant in the acceleration region and is given by

$$\Delta t_2 = \frac{1}{E}\sqrt{\frac{m}{2e}}\sqrt{\Delta V} = 0.92\ ps \tag{3.17}$$

where E is the electric field between the cathode and the pinhole, m and e the electron mass and charge. It is important to remind that electrons obey the Maupertuis principle and not the Fermat principle. Electrons that travel different paths from one point in the object plane to the image plane take different times Δt_3:

$$\Delta t_3 = \frac{1}{2}(\alpha_1^2 \cdot d_1 + \alpha_2^2 \cdot d_2)/v = 0.81\ ps \tag{3.18}$$

In this formula d_1 and d_2 are the electrode 2 distances from the pinhole and the sample, α_1 is the aperture angle of the beam diverging towards electrode 2, α_2

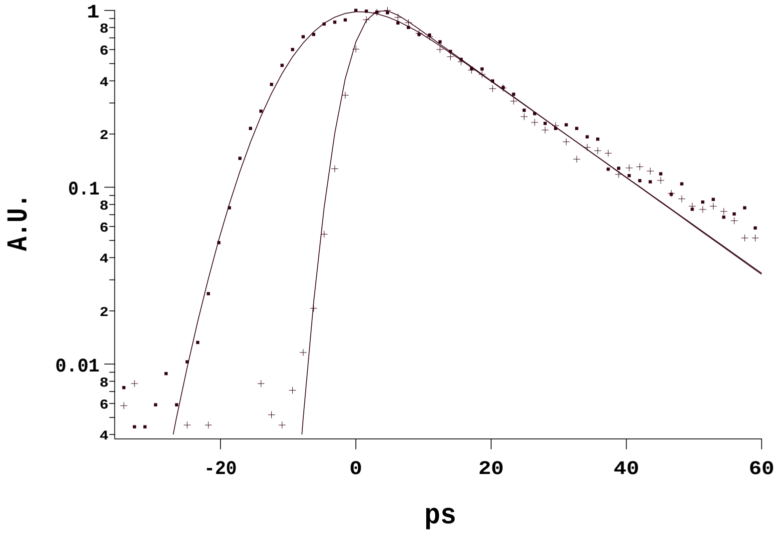

Figure 3.12: Dots are the experimental TRCL data. Markers are the TRPL data. Lines are the two fitting curves.

the aperture angle of the beam focused on the sample and v the electron velocity. In (3.18) we do not consider the acceleration region because this contribution is already computed in formula (3.17). One main cause of temporal broadening is the 45 degrees sample position with respect to the electron beam incident direction and, consequently, to the image plane of our optics system. The electron beam FWHM (210 μm) at the sample level introduces indeed an equal optical path difference. At 2.5 KeV kinetic energy this correspond to a time delay of 7 ps. If we deconvolve this contribution from the measured pulse width we obtain a FWHM pulse of 12 ps. This is the electron pulse broadening of our electron gun. Since the electrostatic lens does not introduce intermediate crossover in the beam path and the laser spot size on the cathode ($R_l = 2.5$ μm) is much smaller than the spot size on the sample, we suppose it to be mainly due to space charge effects in the photocathode proximity.

3.6 Design and implementation

The gun prototype could not be used to replace the thermionic electron gun of the SEM we bought for our TRCL set-up. First of all, for mechanical reasons, it was not possible to adapt it to the SEM column. Finally the gun prototype we mounted in our laboratory was supposed to work in the range 0-5 kV. In a scanning electron microscope the anode is at earth and the cathode potential vary from -1 to -30 kV. Implementing an electron gun that can operate in this voltage range demands a technical know-how. The French firm OPEA collaborated with us in achieving

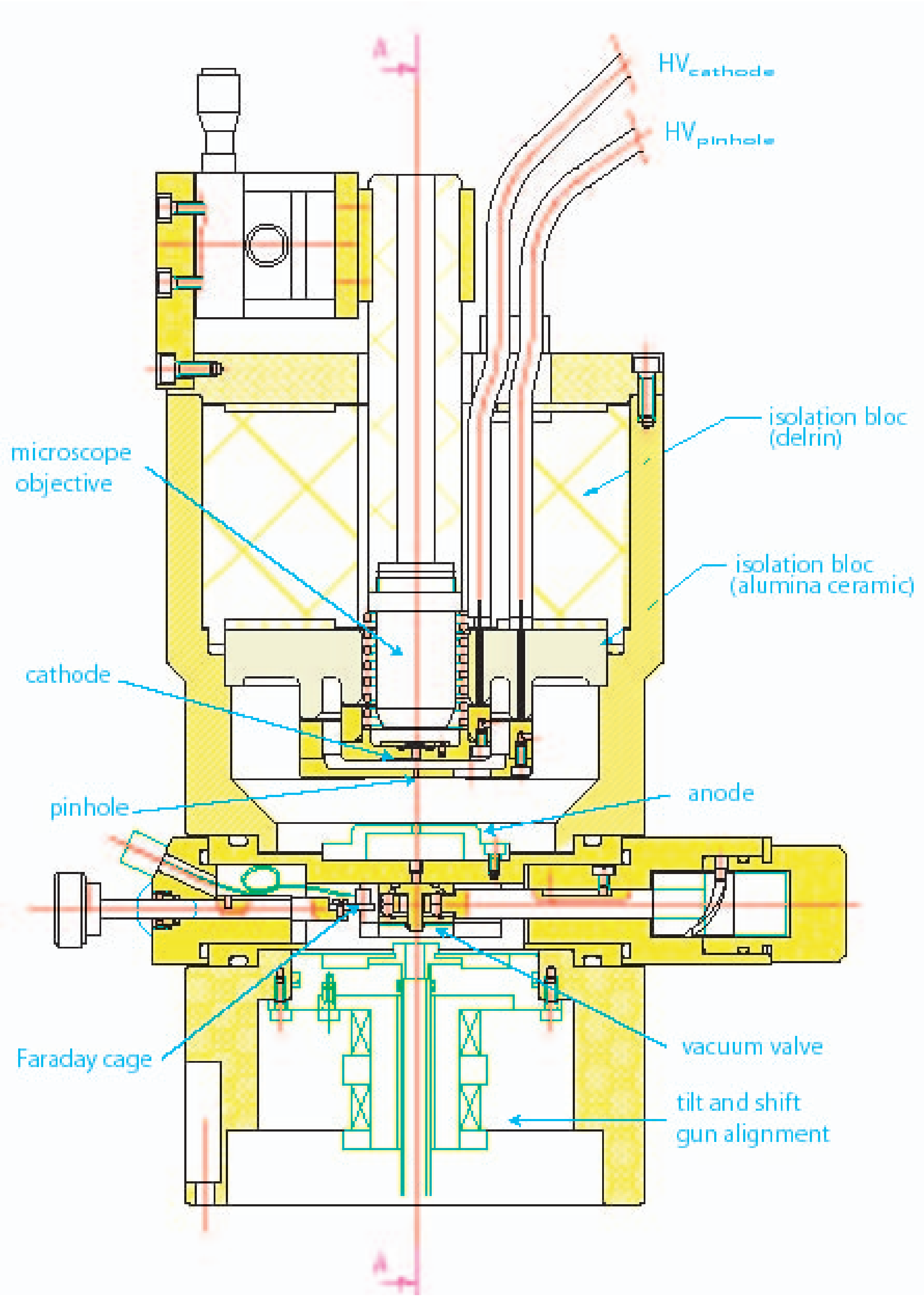

Figure 3.13: High brightness picosecond electron gun.

this task.

In Figure 3.13 the mechanical design of the picosecond electron gun is reported. The electron gun dimensions are: height 23 cm, diameter 12 cm (see also Figure 3.14). We will start to describe it from the piece that has to be inserted on the microscope column (bottom of Fig. 3.13). The JEOL tilt and shift gun alignment is placed inside it. When we removed the thermionic gun, we were forced to remove the coils that align the beam before entering the first microscope lens. They were mounted again, at the same place with respect to the electron optical column, in this adaptation piece.

On top of it a vacuum valve is inserted. It is supposed to preserve the vacuum in the gun while the microscope chamber is open. The bellow connector for the pump is clearly visible on Fig 3.14. At the same level we placed a Faraday cage. When the valve is open, the Faraday cage can be pushed in the optical column axis to measure the current emitted from the cathode. The bloc that contains the vacuum valve and the Faraday cage is removable. In that case the anode, that is placed just on top of it, has to be mounted in its original position: just on top of the alignment coils. Even if very useful, we did not take the risk to design a fixed valve. The main reason is that when we insert it, the optical source for the microscope is 5 cm higher. We were not sure that the column lens system could work properly in these conditions.

Figure 3.14: High brightness picosecond electron gun.

In our design, the cathode support and the pinhole are screwed to two stainless steel circular electrodes. These electrodes are in contact with two high-voltage connectors and are welded to an alumina ceramic bloc that ensures electrical isolation. In an electric discharge electrons usually move on the surface of an isolator. For this reason great care has been taken in the ceramic piece design. The path from cathode support to pinhole is much longer on the ceramic surface than in vacuum. The same for the path from the pinhole to earth. The gold film evaporated on a quartz coverslip is fixed on the cathode support with a silver paint drop. Three holes in the pinhole piece allow for pumping the cathode-pinhole region. A sapphire window placed behind the cathode ensures a good vacuum.

The microscope objective working distance from the cathode is 8.5 mm. In order to avoid electrical discharges it is supposed to be at 30 kV also. A delrin support connects it to a x-y-z linear stage. A mirror (not represented in figure) fixed on top of the gun deviates the collimated laser beam inside the delrin support towards the objective. A delrin isolation bloc isolates the top of the electron gun from the high tension. The UV light is focused on the cathode by checking that the back-reflected light is a collimated beam. The focal spot is placed on the microscope column axis when the Faraday cage current is maximized.

3.7 Conclusion

As a first step towards picosecond cathodoluminescence we have developed a high brightness picosecond electron gun to replace the electron gun of a SEM. The design and the implementation of this system are reported.

A microscope objective focuses UV light pulses (266 nm, 200 fs, 80 MHz repetition rate) on a gold photocathode used in transmission mode operation. An extraction electrode with a circular pinhole, and an anode accelerate the photoelectrons.

The optical properties of the picosecond electron gun have been investigated. This system is equivalent to a thin lens immersed in two regions of different refraction index. The gun brightness is $1.8 \cdot 10^3$ A/cm^{2}sterad, a value high enough to allow for a spatial resolution of 30 nm in the secondary electron imaging mode of a SEM.

The temporal width of the electron pulses at the gun level has been measured by an indirect method. We have compared the time resolved cathodoluminescence emission with the time resolved photoluminescence signal obtained with 200 fs laser pulses. An electron pulse width of 12 ps is found.

4 Picosecond Cathodoluminescence

4.1 Introduction

A complete description of the picoCL set up is given in this chapter. The technical steps that were solved in order to install the laboratory are reviewed. Three of them were the most important. The first one is the electron microscope choice. The second is the fact that the laser system that drives the high brightness picosecond electron gun and the SEM require an anti-vibration system for proper working conditions. Since the laser and the SEM are coupled they must have a common anti-vibration system. For this reason we mounted the SEM on the optical table where the laser was installed. Thirdly the vacuum system modifications required by our gun adaptation to the microscope column are described. The validation and the characterization of set up are reported as well. A spatial resolution of 50 nm in the secondary imaging mode is shown. The test to estimate the temporal resolution (12 ps) concludes this chapter.

4.2 Set up description

Picosecond cathodoluminescence (Fig. 4.1) is an original TRCL set up. A high brightness picosecond electron gun replaces the thermionic gun of a commercial JEOL 6360 SEM. Electron pulses, produced by photoelectric effect, travel down the electron optical column of the SEM and are focused on the sample. The deflection coil in front of the last microscope lens scans the electron probe in a raster across the specimen. The secondary electrons (SE), produced as a consequence of the primary beam-specimen interaction, are collected by an Everhart-Thornley detector. This last one is connected to a computer that, in synchronism with the scanning electron beam, reproduces a topographic image of the sample.

An essential requirement of CL systems designs is a high efficiency of light collection, transmission and detection. In our set up the specimen is placed at the focal point of a parabolic mirror (focal length 3 mm). The collimated luminescence signal is focused either on the entrance slit of a monochromator (Jobin-Yvon SPEX 270M) or directly on a photomultiplier (PM). The photomultiplier signal is first amplified and then sent to the computer that displays a polychromatic CL image of the sample. A monochromatic image is obtained when the PM is placed after the

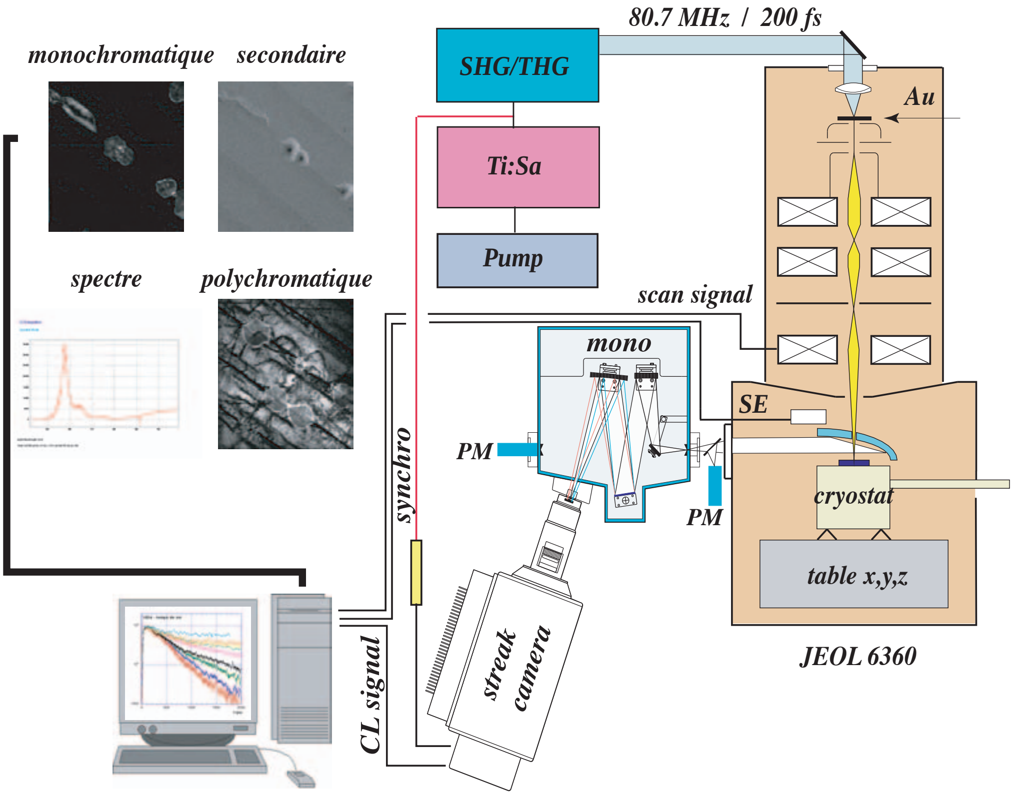

Figure 4.1: Picosecond cathodoluminescence set up. A high brightness picosecond electron gun replaces the thermionic electron gun of the microscope. Examples of SE and CL imaging modes are reported. A streak camera is used to record a spectrum and to perform temporal analysis.

monochromator exit slit. The monochromator has a focal length of 270 mm and an aperture of F/4. Its spectral range operation is fixed by the grating with range 0.185 to 40 μm. We can work with two different gratings both blazed at 750 nm. They have a groove density of 1200 gr/mm and 600 grooves/mm. The resolution for 1200 grooves/mm grating and an entrance slit of 0.1 mm is 0.1 nm at 546.07 nm.

Once we have obtained a SE and a CL image of the system under investigation (a nanostructure for instance) we can decide to study the luminescence emitted from different points of it. It is sufficient to work in the spot mode of the electron microscope. The electron beam is not scanned anymore on the sample surface but it is directed on the point we decided to study. This is one of the advantages of our system with respect to a traditional one. As we saw in section 2.2 a beam blanking unit does not allow to work in the spot mode but the electron beam is always scanned on a surface of few μm^2.

A streak camera (HAMAMATSU C 5680) is used to record spectra and to perform temporal analysis. The light from the monochromator is focused on the entrance slit of the streak. An optics forms a slit image on the photocathode of the streak tube. The input optics spectral transmission is 200 nm to 1600 nm, its effective F value is 5 and the image multiplication ratio is 1:1. Photons are then converted in electrons that are accelerated and sent towards a pair of deflecting plates. When the electrons pass through the deflection plates, a high speed sweep voltage is applied to them so that the electron beam is swept in the direction from top to bottom. This sweep is synchronized with a portion of the light pulse from the Ti:Sapphire laser that is deviated by a beam splitter and received by a high-speed detector, to serve as trigger signal for the streak. Next, the swept electron beam is projected to a micro channel plate, where it is magnified electronically. Electrons are then converted back into light at a phosphor screen. Light is then passed through an output optics system and is directed towards the readout camera (HAMAMATSU C 4742). As a result, the streak image is an image in which the time axis flows from top to bottom. The information in the horizontal direction of the streak image is left just as it is. In our set up this information is the luminescence wavelength.

Finally a LN_2 cryostat allows the sample to be cooled down to 90 K. It consists of a cold copper finger in contact with the sample holder. Despite its simplicity this system guarantees a great stability. The LN_2 cryostat will be replaced by an He cryostat the next year.

4.3 Electron microscope choice

In a SEM electrons from a thermionic or field emission cathode are accelerated toward the anode. The smallest beam cross-section at the gun -the crossover- is demagnified by a two or three electron lens systems so that an electron probe, of diameter $d_p = 1$ nm to 1 μm, carrying an electron probe current $10^{-12} - 10^{-8}$ A, is formed at the specimen surface. We can define the electron microscope magnification M as $M = d_p/d$ where d is the crossover diameter. A SEM electron optical column is designed to have a magnification factor M that varies according to the crossover size and hence for the different types of electron guns.

4.3.1 Thermionic electron gun

The conduction electrons in metals or compounds have to overcome the work function Φ if they are to be emitted from the cathode into vacuum. Increasing the cathode temperature leads to a broadening of the Fermi energy distribution, and for high temperatures, electrons in the tail of the Fermi distribution acquire enough kinetic energy to overcome the work function. The current density j of the cathode emission can be estimated by Richardson's law

$$j = AT_C^2 \exp\left(-\Phi/kT_C\right) \tag{4.1}$$

where k is the Boltzmann's constant, T_C is the cathode temperature and A is a constant that depends on the cathode material.

Most metals melt before they reach a sufficiently high temperature for thermionic emission. An exception is tungsten, which is widely used at a temperature T_C of 2500 – 3000 K (melting point T = 3650 K). Tungsten thermionic cathodes are prepared usually as a wire bent into a hairpin. The tungsten thermionic electron gun has a crossover diameter of 20 – 50 μm, a $j = 1 - 3$ A/cm^2, the gun brightness β at 20 KV is $\beta = 0.2 - 1 \cdot 10^5$ A/cm^{2}sterad [40]. The lifetime of tungsten cathodes $\simeq$ 200 hours is limited by evaporation of the cathode material, which results in a break when part of the wire becomes thin. A vacuum of 1–5 $\cdot\, 10^{-5}$ torr is sufficient to prevent oxidation of the heated cathode.

Lanthanum hexaborides LaB$_6$ cathodes with T_C = 1400 – 2000 K are also employed because their work function is lower. LaB$_6$ rods with a polished tip may be heated indirectly, by supporting them between wires of carbon fibres, or directly, by soldering them on refractory metal strips. The LaB$_6$ electron gun has a crossover diameter of 10 – 20 μm, a j = 20 – 50 A/cm^2, the gun brightness β at 20 KV is $\beta = 0.2 - 1 \cdot 10^6$ A/cm^{2}sterad [41, 42]. LaB$_6$ cathodes attain lifetime of 1000 hours and require a vacuum of 10^{-6} torr. Even if the LaB$_6$ cathode performances are slightly better than that of a tungsten one, some electron microscope companies (Zeiss and Philips) do not produce any more LaB$_6$ electron microscopes. JEOL still produces LaB$_6$ microscopes but has stopped their development.

The electron emission of a thermionic cathode is concentrated within a small area of the cathode tip by means of a negatively biased Wehnelt cup (fig. 4.2). This negative bias is generated by auto-biasing, a voltage drop $\mathrm{U_w} = \mathrm{I_c} \cdot \mathrm{R_w}$ being created across a 1-10 MΩ resistance Rw in connection line of the high-tension supply to the cathode.

The crossover diameter of a thermionic gun, being between 10 and 50 μm, *requires an electron optical column with a magnification factor* $M \leqslant 1/5000$ in order to have a final spot size d_p of 10 nm. The lens system focuses the electrons to form one or two intermediate crossovers before the electrons reach the specimen.

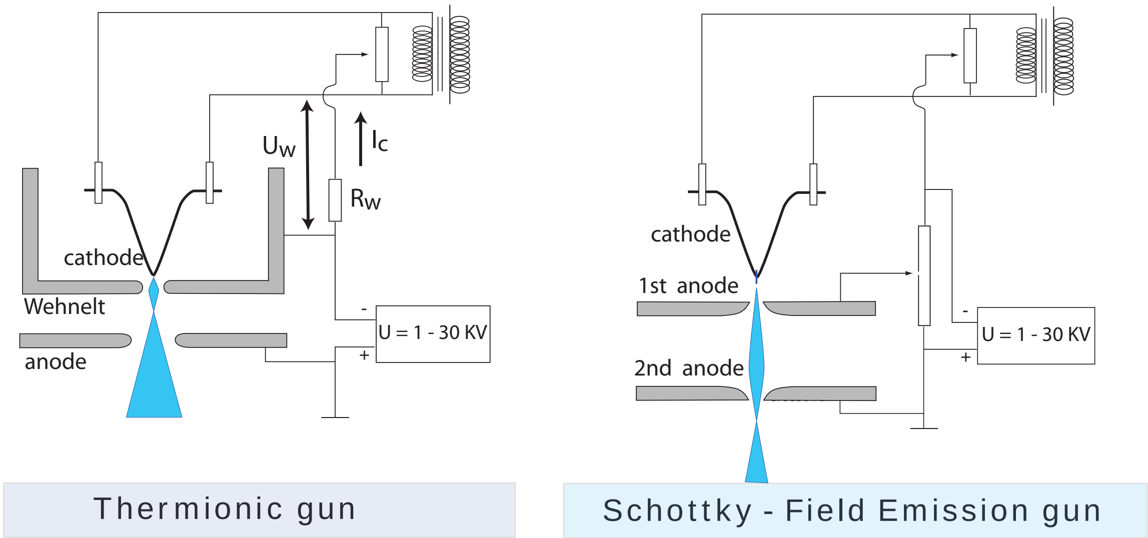

Figure 4.2: A thermionic electron gun consists of cathode, Wehnelt cup and anode. The Wehnelt bias $\mathrm{U_w}$ is provided by the voltage drop of the emission current $\mathrm{I_c}$ across $\mathrm{R_w}$. A field emission gun consists of cathode and two anodes. The first anode acts like an extraction electrode.

4.3.2 Schottky gun

The potential energy V(z) of an electron in front of a conducting surface at a distance z larger than the atomic diameter can be calculated by considering the effect of a mirror charge with opposite sign behind the surface. If an electric field $\mathcal{E}$ is applied, the potential energy $V = -e|\mathcal{E}|z$ is superposed on that of the mirror charge giving

$$V(z) = \Phi - \frac{e^2}{16\pi\epsilon_0 z} - e|\mathcal{E}|z \tag{4.2}$$

When the field strength $\mathcal{E}$ at the cathode is increased, the overlap of potential energies in 4.2 results in a decrease $\Delta\Phi$ of the work function (Schottky effect). Electrons still have to overcome the now lowered work function Φ_{eff}

$$\Phi_{eff} = \Phi - \Delta\Phi = \Phi - e\sqrt{\frac{e|\mathcal{E}|}{4\pi\epsilon_0}} \tag{4.3}$$

by their kinetic energy, which is furnished by heating the cathode.

The LEO 1500 (Zeiss) has a Schottky ZrO/W tip emitter. Its working temperature is typically 1800°K, its performances are d = 15 nm, j = 500 A/cm^2,

β (20kV) $= 4 \cdot 10^7$ A/cm^{2}sterad [43]. This cathode is less robust than a thermionic one and has to operate in a vacuum of 10^{-8} torr.

4.3.3 Field emission gun

Field emission (FE) from a tungsten tip of radius $r \simeq 0.1\mu$m starts when the electric field $\mathcal{E}$ increases to values larger than 10^7 V/cm. By tunnel effect electrons from the Fermi level can escape into vacuum. Field effect cathodes need an ultra high vacuum better than 10^{-9} torr because otherwise the tip radius is destroyed by ion bombardment from the residual gas. They can function at room temperature. The main advantages of FE guns are the high brightness (β (20kV) $= 5 \cdot 10^8$ A/cm^{2}sterad) and the small diameter of the crossover ($<$ 10 nm) so that only one demagnifying lens is needed to get electron probe diameters below 1 nm [44]. *The electron optical column for a Schottky or FE gun has a magnification factor* $M \leqslant 1/15$.

Schottky and field emission guns need two anodes. The first regulates the field strength at the tip and hence the emission current. (It operates like an extraction electrode.) The second anode accelerates the electrons to the final kinetic energy.

4.3.4 Electron optical column for the picosecond electron gun

A table that summarizes the principal parameters of thermionic, Schottky and field emission guns for an accelerating voltage of 20 kV is reported in this section. They are compared to the high brightness picosecond electron gun described in the previous chapter. The crossover diameter of our electron gun is 5 μm (section 3.4.2). The gun brightness is high enough to allow for a probe spot diameter of 50 nm still having enough current to obtain a secondary electron image (section 3.4.3). *The magnifying factor we require from an electron optical column is at least* $M \leqslant 1/100$. This request forces us to choose the column of a thermionic electron microscope for our set-up.

The gold photocathode does not need an ultra high vacuum environment like the Schottky or the FE guns require. Indeed our picosecond gun works properly at the same vacuum conditions of a LaB$_6$. We preferred anyway to choose for our set-up a tungsten electron microscope because, as we said before, electron microscope companies stopped the LaB$_6$ development.

Table 4.1 Electron gun comparison

	Tungsten	**LaB_6**	**Schottky**	**FE**	**Gold**
T_C (K)	2500-3000	1400-2000	1800	300	300
Φ (eV)	4.5	2.7	2.7	4.5	4.3
j (A/cm^2)	1-3	20-50	500	10^5	$1.2 \cdot 10^{-1}$
β $(A/cm^2 sterad)$	$0.2 - 1 \cdot 10^5$	$0.2 - 1 \cdot 10^6$	$4 \cdot 10^7$	$5 \cdot 10^8$	$1.8 \cdot 10^3$
ΔE (eV)	1.5-3	1-2	0.3-0.7	0.2-0.7	0.1
d (μm)	20-50	10-20	0.015	0.002	5
p $(torr)$	10^{-5}	10^{-6}	10^{-8}	10^{-10}	10^{-6}

Characteristic parameters

Cathode temperature T_C
Work function Φ
Current density j
Gun brightness (20 kV) β

Energy spread ΔE
Crossover diameter d
Operating vacuum p

Chromatic aberrations depend on the initial electron energy dispersion ΔE. In table 4.1 ΔE is reported for all the electron guns. The picosecond gun (section 3.3.2) has the most favourable conditions with respect to the others.

If we look at figure 4.2 we see that Schottky or field emission gun have an extraction electrode and an anode to accelerate electrons. This is the same configuration needed by our pulsed electron gun. The best choice for the picoCL set up is the microscope column of a thermionic electron gun and the power supply of a field emission system.

4.3.5 JEOL 6360

The scanning electron microscope for the picoCL set up is the JEOL 6360. The tungsten hairpin filament accelerating voltage can be varied between -1 kV to -30 kV . The anode is at ground. An electromagnetic 2-stage deflection unit is employed to align the electron beam before entering the microscope optical column.

The first microscope lens is an electromagnetic 2-stages zoom condenser lens system that performs a beam demagnification. A conical objective lens focuses the electrons over the sample. The optimal objective working distance is 8 mm. Three objective lens aperture pinholes (100-30-20 μm diameter) can be inserted in the electron beam paths. The smallest one is used for high resolution observation. The scan coils deflectors allow for images magnification between 5X and 300.000X. An astigmatism correction system is provided also.

The guaranteed microscope resolution is 3 nm at an accelerating potential of 30 kV and a working distance of 8 mm. The probe current can varies between 1 pA to 1 μA. The microscope is equipped with an Everhart-Thornley detector for SE imaging mode operation.

4.4 PicoCL installation

As we said in this chapter introduction the JEOL 6360 was mounted on the optical table where the laser was installed. After this operation we verified that the microscope resolution was not affected by our modification. As a further step towards the final time resolved system, a continuous CL set up was tested. The laboratory installation was concluded when the picosecond electron gun replaced the thermionic one.

4.4.1 SEM on the optical table

Figure 4.3 shows the result of the JEOL 6360 installation. The electron optical column and the specimen chamber are fixed to a non-magnetic steel optical table. This last one has a hole designed for the vacuum pumping system to be connected to the microscope column. A turbomolecular vacuum pump is suspended to the

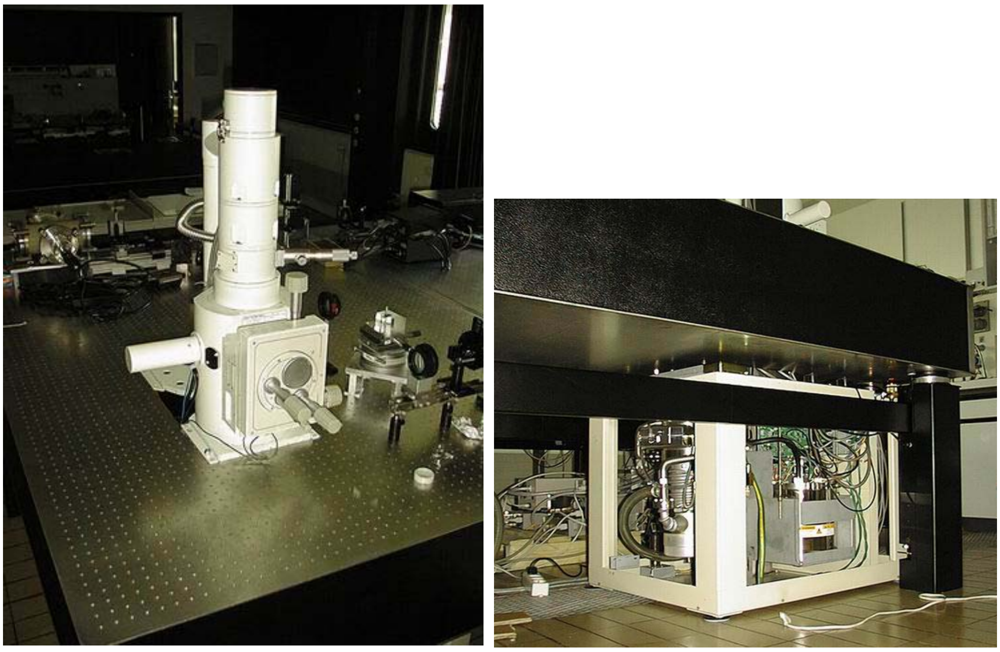

Figure 4.3: Left: electron optical column and specimen chamber above the table. Right: electronics and vacuum pumps below the table.

microscope column while a rotary pump is connected to this one by a flexible pipe. The microscope electronics controls are placed below the table. In this configuration the SEM shares the same anti-vibration system of the laser system. Due to the great magnification factor we need for high-resolution operation, we are indeed very sensible to crossover displacements. In this way the laser spot size on the cathode has the same dispacements of the microscope column.

When the installation was over, we tested the electron microscope operation. Images of gold particles deposited on carbon are shown in figure 4.4. These images were obtained on a sample provided by JEOL. The left one was performed with the SEM original configuration, the right one after the microscope installation on the optical table. The slight differences are due to the fact that images were obtained at different acceleration voltages and different brightness and contrast regulations. It is evident that the microscope resolution was not affected by the changes imposed by our set up.

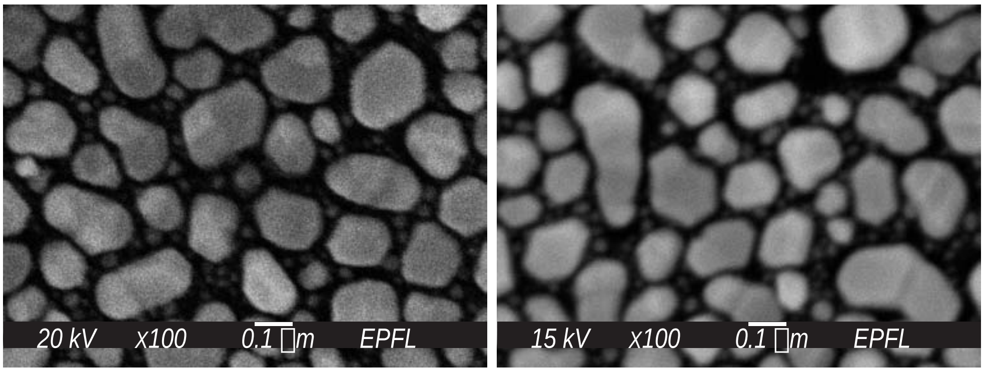

Figure 4.4: Secondary electron images of gold particles on carbon. The magnification is 100.000X. Left: image obtained with the SEM in its original configuration. Right: image obtained with the SEM installed on the optical table.

4.4.2 Continuous CL

Before replacing the thermionic gun with the picosecond electron gun we mounted and tested also the continuous CL set up. The measurements performed with this system are part of a diploma thesis work that was carried out in our laboratory [45]. The GaN epitaxial lateral overgrowth (ELO) structures shown here were grown by Denis Martin (IPEQ-EPFL) and are used as an example of the CL potentialities. Spatially resolved characterization by cathodoluminescence spectroscopy of similar sample is reported in literature [46]. A 2 μm thick GaN layer is grown by Metal-Organic Chemical Vapor Deposition (MOCVD) on (0001) sapphire and pattern with stripes of a 120 nm SiO_2 mask. The parallel SiO_2 stripes are ordered in specific direction, the width of the windows and the mask are 5 and 10 μm respectively. The lateral overgrowth is achieved using 50 μm thick hybride vapor fase epitaxy (HVPE) GaN deposited on the underlying MOCVD GaN layer through the windows in the SiO_2 mask. The CL images and spectra in this section were taken at 5 kV accelerating voltage and at a temperature of 110 K.

The parabolic mirror used to collect the luminescence signal 4.1 has a little hole, above its focal point, that allows electrons for going through and exciting the semiconductor sample. When the specimen is at the mirror focal point, its distance from the mirror edge is 1 mm only. It can perturb the electric field that drives electrons towards the SE detector. Anyway we never had any problem to obtain good SE images even with the mirror inserted in the electron beam. An example of SE image obtained with the collecting mirror placed above the sample for CL measurement is reported in figure 4.5.

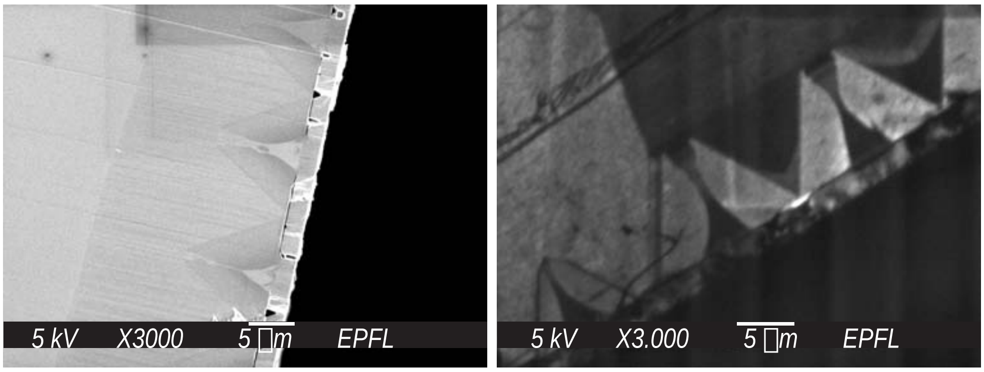

Figure 4.5: Left: Secondary electron image of ELO GaN structures. The SiO2 masks and the triangular shape of the overgrowth GaN are clearly visible. Right: Polychromatic CL image. The region above the mask windows is dark.

Correct alignment of the parabolic mirror is not easy. We want the luminescence to be collimated when it leaves the electron microscope directed towards the light detector. This imposes less restrictions on the distance we can install the photomultiplier or the monochromator. In this case the exciting electron beam and the specimen must be at the mirror focal point. The procedure we use for proper alignment is the following. We insert a light source in a metallic box with a pinhole aperture. The pinhole is place approximately to the mirror focal point. We make a SE image of the pinhole with the electron microscope and we centre it on the computer screen. The mirror position is corrected in order to collimate the light beam from the source. If necessary, the pinhole distance from the mirror and hence the electron beam focalization are corrected also. A lens focuses the light beam on the monochromator entrance slit. When the parabolic mirror alignment is not correct, the focal spot on the slit has a typical coma aberration.

The light detector for CL imaging mode operation is a photomultiplier. It produces a current proportional to the incident luminescence signal. A home made current-voltage converter adapts the signal for the SEM imaging card. A polychromatic CL image of epitaxial lateral overgrowth of GaN structures is shown in figure 4.5. Monochromatic images obtained with the PM placed at the monochromator exit are reported in figure 4.6. The slit is partially closed to select only a certain wavelength range.

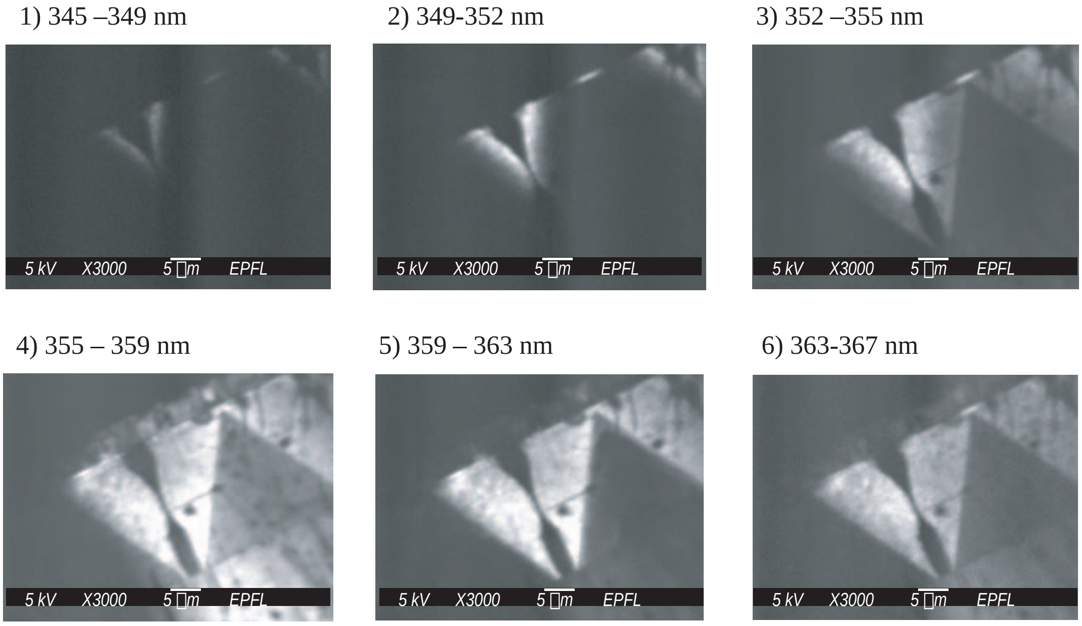
1) 345 –349 nm
2) 349-352 nm
3) 352 –355 nm
4) 355 – 359 nm
5) 359 – 363 nm
6) 363-367 nm

Figure 4.6: Monochromatic CL images of GaN ELO structures.

Images in fig 4.6 show that the luminescence wavelength varies when we excite different regions on the specimen. Spectra for seven selected emission points are reported in figure 4.7. These spectra were obtained by centring on the computer display the point to be analysed and increasing the microscope magnification to its maximum possible value. (300.000X). We were forced to use this procedure because JEOL 6360 electron microscope is not provided with the beam stop function. An external scan control (4Pi Digital Imaging System) that allows for driving and positioning the electron beam, has been recently installed in order to overcome this problem. These measurements evidence a region of large local free carrier concentration above the SiO_2 stripes (brighter region in figure 4.7). This lead to the broad and strongly blue-shifted CL emission observed in spectra d) and e).

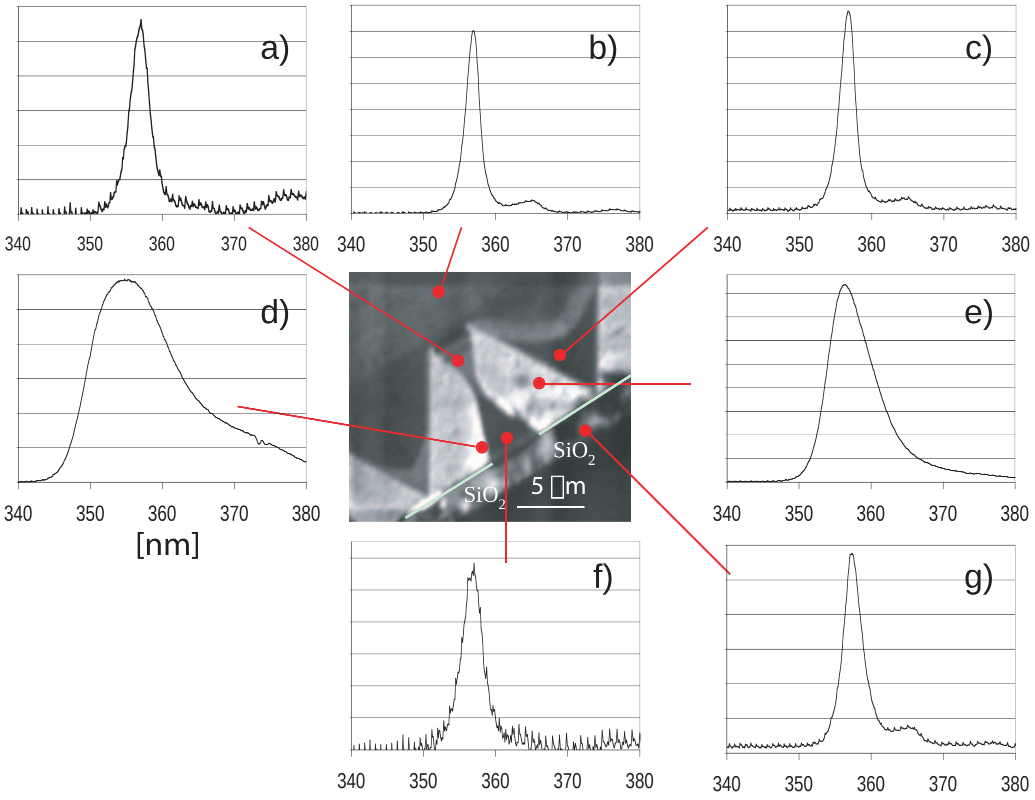

Figure 4.7: Spectra from selected points of GaN ELO structures. As in reference [46] we observe large local free carrier concentration leading to the broad and strongly blue-shifted CL emission in regions d) and e).

4.4.3 High brightness picosecond electron gun installation

The JEOL 6360 electron microscope column is divided in five blocs. The first one is the electron gun that is followed by the gun alignment system and the condenser lens. The two last blocs are the scan system and the objective lens. Every part is screwed to the other and is separated by an o-ring ensuring a good vacuum. Mechanical reasons forced us to remove the first two blocs for installing the picosecond electron gun. The gun alignment system was inserted again in the photoemission electron gun design (fig. 3.13). It was placed at the same position it occupied before with respect to the rest of the microscope column.

A vacuum valve divides the picosecond gun and the gun alignment system. When the valve is open a pinhole aperture (diameter 1 mm), which allows for differential pumping of the gun region, connects the two parts. As we saw in section 4.3.4 the picosecond electron gun requires a vacuum of 10^{-6} torr while the tungsten tip requires 10^{-5} torr. Good vacuum conditions at the gun level were obtained by modifying the electron microscope pumping system. The JEOL 6360 is provided with an oil diffusion pump. We replaced it with a turbomolecular pump (LEYBOLD TURBOVAC 361) and an ionic pump (VARIAN Vacion plus 25). The turbo is pumped by the original JEOL oil rotary pump and is connected to the specimen chamber and to the ionic pump by two vacuum pipes (fig. 4.8). The ionic pump is connected to the picosecond gun. The connection is done above the valve that divides it from the gun alignment system. When the vacuum in the electron microscope is of the order of 10^{-5} torr we switch on the ionic pump for differential pumping at the gun level and close the vacuum valve that connects the turbo to the ionic pump. In such a way the vacuum in the specimen chamber is 10^{-5} torr but we can have a vacuum of 10^{-6} torr in the gun region.

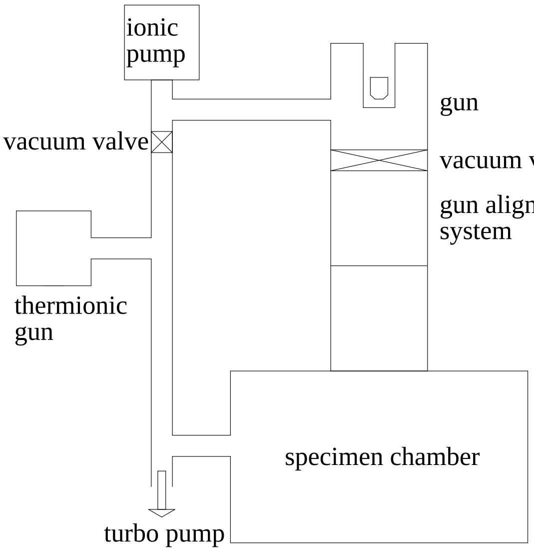

Figure 4.8: Block diagram of the electron microscope pumping system. These modifications were made in collaboration with the firm OPEA.

The thermionic electron gun is removed from the microscope column but it is still pumped with the turbo. The computer program that drives the JEOL 6360 electron microscope must detect a current flowing in the tungsten hairpin for allowing the user working with it. For this reason the electrical connection to the thermionic gun were not removed and we let this gun operating “as usual”.

A homemade power supply is used to accelerate the electrons at the gun level. It is similar to the power supply of a field emission electron gun. Two high voltage power supply modules (Spellmann MP 30N) which provide 0.33 mA maximum current and 0 to -30 kV voltage range were connected to the cathode and the pinhole. The most important requirement for an electron gun power supply is the voltage stability. The two Spellman modules guarantee a ripple of 300 mV peak to peak at full load that is largely sufficient for our working condition. It causes an initial energy dispersion of the same order of magnitude of the photoelectrons initial energy dispersion (0.1 eV) and ten times less than that of a thermionic gun.

A periscope raises the UV radiation to the gun level. It directs the light pulses towards a mirror fixed on top of the electron gun. This last one deviates the laser beam towards the microscope objective that focuses on the gold film.

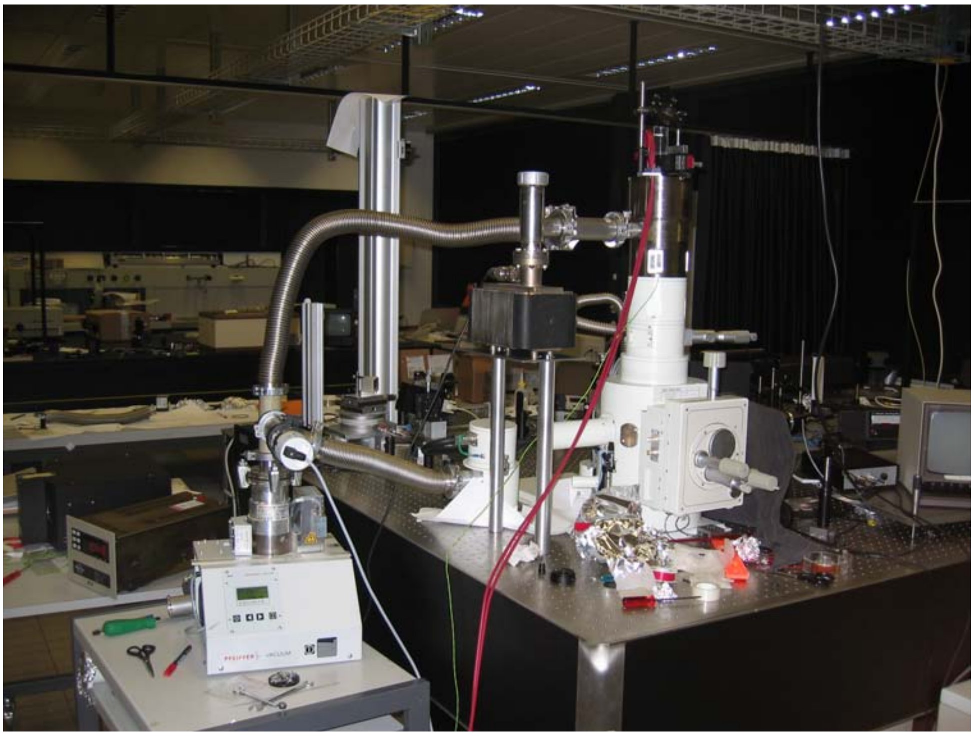

Figure 4.9: Picosecond electron gun installed on the JEOL 6360. The two red high tension cables, the ionic pump, the thermionic gun, and the periscope are clearly visible.

4.5 Picosecond cathodoluminescence

4.5.1 Alignment

Once the picosecond electron gun is mounted on the microscope column we activate (section 3.3.1) the gold cathode. The gold film is irradiated with 266 nm UV light for several hours. The emitted photocurrent is detected with the Faraday cage placed in front of the gun vacuum valve (fig. 3.13 and fig. 4.8). When the current produced for a fixed amount of incident light is constant we can begin the microscope alignment procedure.

The laser beam is focused on the gold film by the microscope objective. The optimal working distance is found by checking that the back-reflected beam is collimated. The laser spot size position on the gold film must coincide with the microscope column axis. This is done by maximizing the photocurrent in the Faraday cage. An alternative possibility is to look at the signal on the microscope computer screen and to correct the laser position on the gold film until this last one is maximal.

An electron microscope column is in general aligned from top to bottom. It is possible to correct slight beam spot size misalignments $\simeq 100$ μm with the gun tilt and shift alignment system.

The beam spot size on the specimen is fixed at the condenser lens level. A great spot size means more exciting current at the sample level and hence more imaging contrast, a little one allows for greater resolution. In general a compromise between contrast and resolution must be found.

The objective lens aperture determines the probe beam aperture at the sample level. A little aperture reduces the probe current on the sample but reduces also the objective lens aberrations when a little probe diameter is needed.

Astigmatism is not noticeable at low magnification (X 1000), however if you raise the magnification to a high value, the image appears to flow in a certain direction before and after the focal point, making it difficult to perform accurate focusing. The microscope stigmator system is placed at the objective lens level. In general astigmatism is corrected when an objective lens aperture is already inserted in the electron beam path.

The column alignment procedure described here is the same used for the thermionic gun. A great amount of regulations are totally controlled by the computer. For instance the user has no access to the currents circulating in the microscope column lenses. The voltage applied to the thermionic gun fixes their values. The accelerating voltage of the picosecond electron gun is furnished by our home made power supply. We are free to vary the voltage applied to the thermionic gun to change currents, and then the focal lengths of the microscope column lenses. This possibility turns out to be very useful. The crossover axial position for the thermionic gun varies in a different way with respect to the picosecond gun. Changing the focal length of the lenses helps to correct for this difference.

4.5.2 Spatial resolution

The picoCL characterization began with the secondary electrons imaging mode test. We looked at gold particles deposited on a carbon substrate. Such a sample is typically used to characterize commercial SEMs. A secondary electrons image obtained with the thermionic electron gun (fig. 4.10) shows that the gold particles have different diameter between 50 to 200 nm.

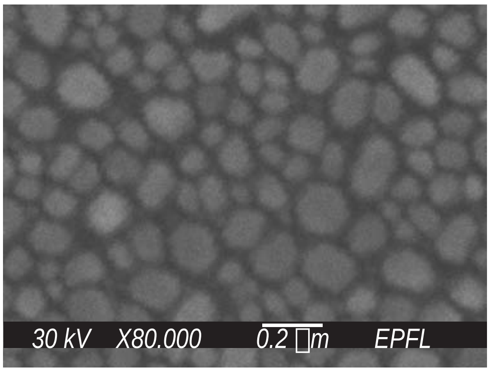

Figure 4.10: A SE image of the sample used for testing the resolution of the picoCL set up. This image was obtained with the thermionic electron gun.

Low magnification images of the same sample, obtained with the picosecond electron gun, are shown also (fig 4.11). An acceleration voltage of -5 kV was applied to the gold film. The pinhole was polarized at –4.5 kV. The thermionic gun accelerating voltage was set at -3 kV. This value was chosen to have images with the maximum signal to noise ratio.

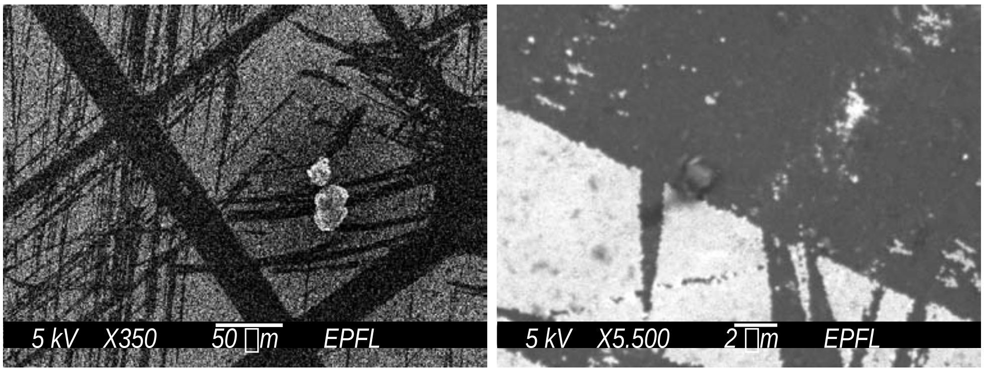

Figure 4.11: PicoCL SE images. The accelerating voltage reported from now on is that applied to the gold cathode.

A problem we had to face with our set up was to calibrate the distances on our images. The micron marker indicating the distance scale on reported images is the original one displayed on the computer microscope and it need to be slightly corrected. The reason for that is the difference between the acceleration voltages applied to the thermionic cathode and to the gold cathode. Images were calibrated using samples where distances were known. In figure 4.12 a periodic array of Al-

GaAs/InGaAs tetrahedral pyramidal grown by OMCVD (organometallic chemical vapour deposition) is reported. The distance between the centres of two pyramids is 5 μm. The two bars represent a distance of 2.3 μm and 1.18 μm respectively and not 2 μm and 1 μm as reported.

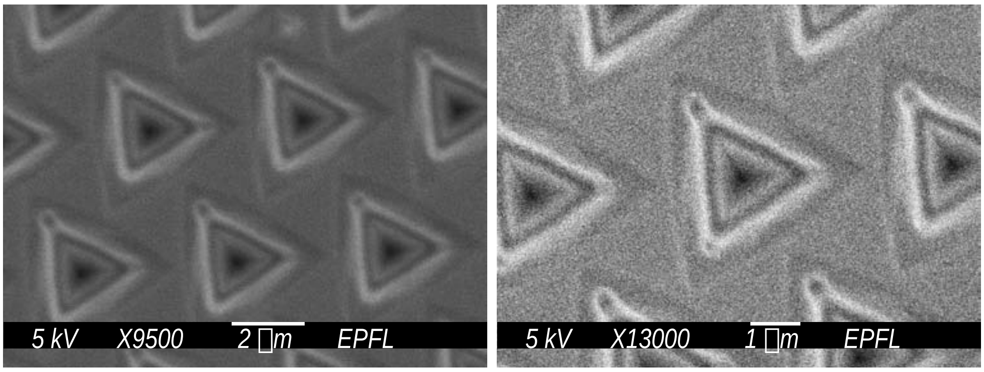

Figure 4.12: PicoCL calibration. The distance between the centre of the two pyramids is 5 μm. This sample can be used to correct the distances displayed by the modified electron microscope.

Finally we tried to do an image of gold particles with the picoCL set up (fig. 4.13). A line profile is reported also and it is used to show the system spatial resolution. Probe size and resolution are interrelated in SEM. The resolution can be worse but not better than the probe size. When using the SE mode, the high resolution results from the excitation of secondary electrons by the incident electron probe from an exit depth t_{SE} of the order of a few nanometres. In our case we are limited by the electron probe size that is greater than t_{SE}. (You need the brightness of a field emission gun to have a probe size smaller than t_{SE}.) When the electron probe scans across to a sharp edge, the transmitted intensity becomes a smoothed step function. The resolution can be defined as the distance between points corresponding to 10 % and 90 % of the total step height [20].

We made the approximation of considering a gold particle having a sharp border and applied this method two the gold particles image obtained. The picture dimensions are 1.55 x 1.09 μm. The line considered to trace a profile (5 μm width) is marked in red. On the left hand side of the picture it crosses two gold particles clearly separated. We look at the edge of the left one. The two segments on the graph indicate the mean minimum and maximum value. The two stars correspond to the 10 % and the 90 % of the edge height. They are separated by 50 nm. This is our system resolution.

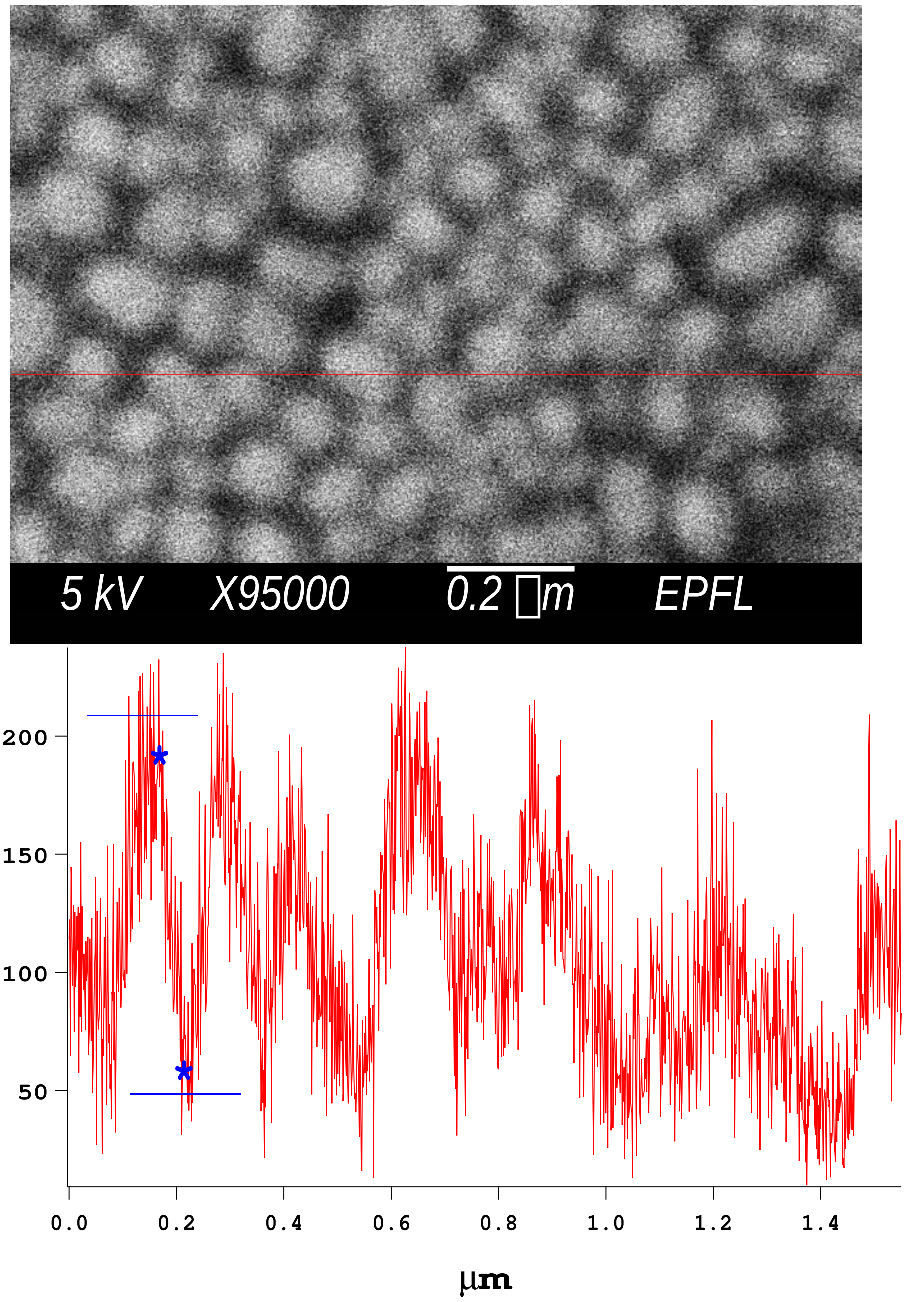

Figure 4.13: Spatial resolution test. The resolution is defined as the distance between points corresponding to 10 and 90 % of the total step height when a sharp edge is crossed.

4.5.3 CL imaging mode

Another important test for the picoCL set up was to obtain good quality CL images (fig. 4.14). The alignment procedure for a time resolved CL experiment is equal to that employed for the continuous one. In order to evaluate the performances of the new system we used the same sample that was tested to validate the CL continuous system.

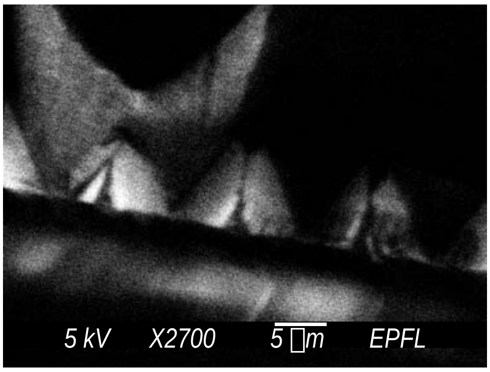

Figure 4.14: Polychromatic CL images of ELO GaN structures.

The spatial resolution of a CL image is limited by the diffusion cloud (fig. 4.15), caused by the gradual loss of the incident electron energy, and by the carrier mobility. The primary electron range interaction (radius of the diffusion cloud) depends on the exciting beam energy and on the specimen density. The carrier mobility depends on temperature and properties of the sample under investigation. In the case of ELO GaN structures excited with 5 kV electron beam at T = 300 K, a spatial resolution of 250 nanometres was found (fig. 4.16).

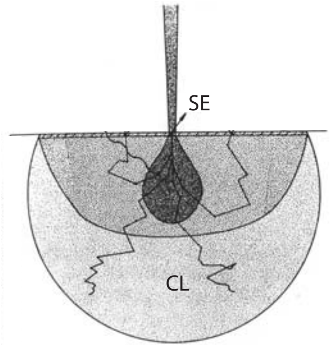

Figure 4.15: Incident electron diffusion cloud. Carriers that contribute to luminescence are generated in the whole diffusion cloud.

This sample was used also for testing the system temporal resolution. We were interested to measure the electron pulse width at the sample level. Like the measure of the pulse width at the gun level (see section 3.5) the collimated luminescence signal was focused directly on the streak camera. The electron beam was focused in different point of the GaN structures. The result report below is the temporal response of the dark region above the window of the SiO2 mask (fig. 4.16). The carrier lifetime in this point is indeed the shortest one for all the sample.

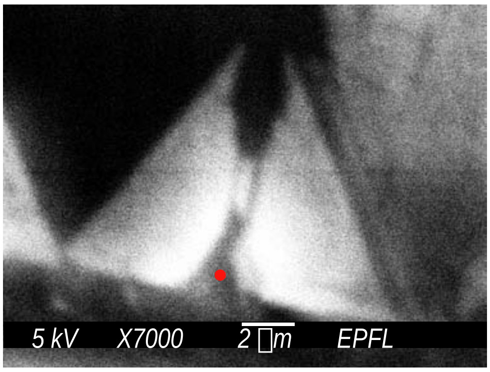

Figure 4.16: High magnification CL image of an ELO GaN structures at room temperature. The CL spatial resolution is few hundreds of nanometres. To obtain the picoCL temporal resolution test reported below, we fixed the electron beam in the point indicated by the red disk.

4.5.4 Temporal resolution

In the case of the pulse width measurement for the high brightness picosecond electron gun, we deconvolved the TRCL signal with the TRPL from a GaAs:Si sample (see section 3.5.2). The photoluminescence response was obtained with the same experimental configuration used for the cathodoluminescence one. Measuring the time resolved PL from a specific point of the ELO GaN structures (fig. 4.16) would have required a microPL set up. We chose to not perform the TRPL experiment and to deduce directly the electron pulse width from the TRCL signal with a different analysis of the data.

The equation for the carrier population evolution as a consequence of an electron pulse excitation is given by

$$\frac{dN}{dt} = f(t) - \frac{N}{\tau_r} - \frac{N}{\tau_{nr}} \tag{4.4}$$

where N is the number of carrier at time t, $f(t)$ is the exciting pulse profile and τ_r, τ_{nr} are the radiative and non-radiative carrier lifetimes. We are neglecting the rise time of the luminescence emission because, according to the electron pulse width measurement at the gun level, our experimental results show that it is little with respect to this last one. The TRCL signal is the number of photons $n(t)$ emitted between t e t+ dt and it is given by

$$n(t)dt = \frac{N(t)}{\tau_r}dt \tag{4.5}$$

$N(t)$ and $n(t)$ are proportional so we can limit ourselves to compute $N(t)$. By integrating equation 4.4 we find

$$N(t) = \exp\left(-\frac{t}{\tau}\right)\int_0^t f(x)\cdot\exp\left(\frac{x}{\tau}\right)\cdot dx; \qquad \frac{1}{\tau} = \frac{1}{\tau_r} + \frac{1}{\tau_{nr}} \tag{4.6}$$

where the integration constant has been chosen to have $N(0) = 0$. As in sections 3.5.2 and 3.4.3 we make the assumption that the electron pulse profile is gaussian. In this case N(t) is

$$N(t) = N_0\cdot\exp\left(-\frac{t}{\tau}\right)\int_0^t \frac{1}{\sqrt{2\pi}\sigma}\exp\left[-\frac{(x-x_0)^2}{2\sigma^2}\right]\cdot\exp\left(\frac{x}{\tau}\right)\cdot dx \tag{4.7}$$

We used this last expression to fit our experimental data (fig. 4.17). The best fit was obtained choosing a τ of 80 ps and a gaussian FWHM of 11 ps.

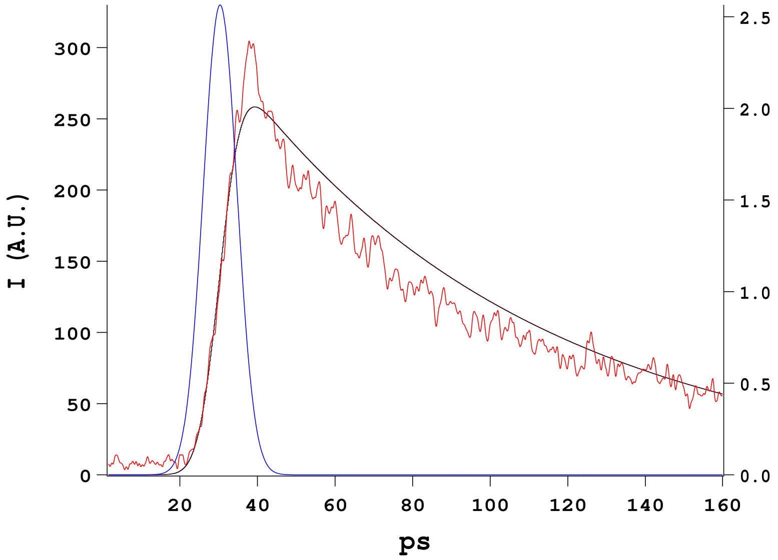

Figure 4.17: Temporal resolution test. Red: data. Black: fit with one carrier population. Blue: Electron pulse profile to obtain the best fit. The right axis is referred to the gaussian function. The gaussian is centred at 29 ps, the FWHM is 11 ps.

In order to obtain a better fit we made the hypothesis that carriers have two channels to relax. We can divide carriers in two populations $N_1(t)$ and $N_2(t)$, with two different decay times τ_1 and τ_2. The two populations obey equation 4.4 and they give a total population $N(t) = N_1(t) + N_2(t)$ equal to

$$\begin{aligned} N(t) = \quad & N_1 \quad \cdot \exp\left(-\frac{t}{\tau_1}\right) \int_0^t \frac{1}{\sqrt{2\pi}\sigma} \exp\left[-\frac{(x-x_0)^2}{2\sigma^2}\right] \cdot \exp\left(\frac{x}{\tau_1}\right) \cdot dx \, + \\ & N_2 \quad \cdot \exp\left(-\frac{t}{\tau_2}\right) \int_0^t \frac{1}{\sqrt{2\pi}\sigma} \exp\left[-\frac{(x-x_0)^2}{2\sigma^2}\right] \cdot \exp\left(\frac{x}{\tau_2}\right) \cdot dx \end{aligned} \tag{4.8}$$

Finally the fit was pretty good (fig. 4.18) with $\tau_1 = 6.3$ ps, $\tau_2 = 87$ ps and a Gaussian FWHM = 12 ps.

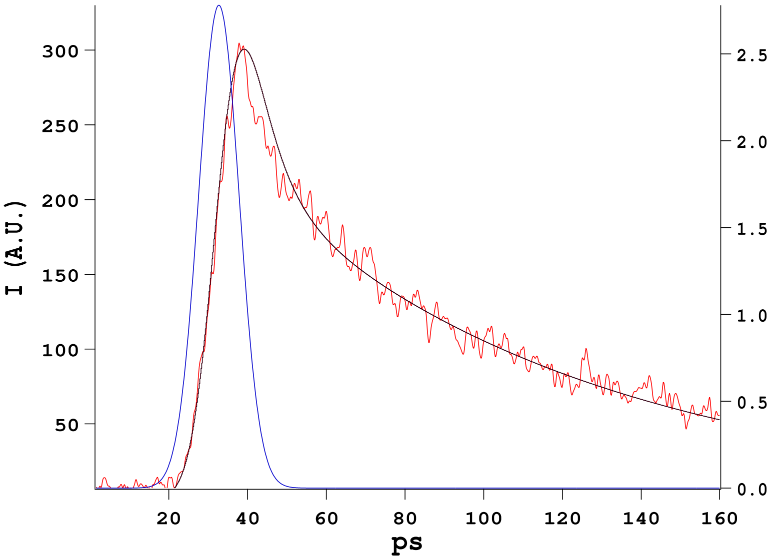

Figure 4.18: Temporal resolution test. Fit with two carrier populations. The Gaussian is centred at 31 ps, the FWHM is 12 ps.

The hypothesis of the two carrier populations does not change the FWHM of the exciting pulse too much. This parameter is indeed very important to fit the rise time of our experimental data. We can safely conclude that the electron pulse temporal width is 12 ps ± 1 ps. This is the temporal resolution of the picoCL set up.

If we compare this result with the pulse width measured at the gun level we observe that we do not have an appreciable pulse spreading down the microscope column. Causes that contribute to the temporal pulse broadening down the column are the same treated in section 3.5.2. In particular the aperture angle of the electron beam is small enough to neglect path difference effects. Our experimental results also suggest that space charge effects, during flight, are not relevant too.

4.6 Conclusion

Picosecond cathodoluminescence is an original time resolved cathodoluminescence set up to study semiconductor nanostructures. A high brightness picosecond electron gun replaces the electron gun of a commercial SEM. The secondary electron imaging mode of the system allows for reproducing topographic images of the sample under investigation. By collecting the luminescence emitted as a consequence of the primary electron beam excitation, a cathodoluminescence image of the sample can be obtained as well. A monochromator and a streak camera are used to perform spectral and temporal analysis of the luminescence emission.

The purpose of the electron optics of a SEM is to produce a small electron probe at the specimen by demagnifying the electron optical source at the gun level. The magnification factor we require for the picoCL set up is $\leqslant 1/100$. This request forces us to choose the electron optical column of a thermionic electron microscope (JEOL 6360) rather than that designed for a field emission gun. The SEM installation, it shares the optical table with the femtosecond laser, and the vacuum system modifications were the most relevant technical problems to solve.

An image of gold particles deposited on a carbon substrate, a sample typically used to characterize commercial SEMs, shows that the spatial resolution of the SE imaging mode is 50 nm. The temporal profile analysis of the luminescence emission from an ELO GaN sample allows for estimating the electron pulse width (12 ± 1 ps) at the sample level. This is the temporal resolution of the picoCL set up.

5 Carrier transport in InGaAs/AlGaAs tetrahedral pyramidal quantum structures

5.1 Introduction

As a first study with the picoCL set up, we investigated the time resolved luminescence of quantum structures located in InGaAs/AlGaAs tetrahedral pyramids. The experimental results obtained provided interesting information about carrier transport in these nanostructures. This chapter begins with the sample description. Continuous and time resolved CL measurements follows. Finally a model is developed to interpret the experimental data.

5.2 Sample growth and structure

The investigated pyramidal nanostructures are fabricated with the following procedure [47, 48]. Prior to growth, a GaAs substrate is patterned with a 5 μm pitch hexagonal matrix of tetrahedral recesses, using standard photolithography and wet chemical etching (fig. 5.1). The characteristic tetrahedral pyramid pattern, exposing (111)A facets, is obtained in this case due to the anisotropic nature of the wet chemical etching.

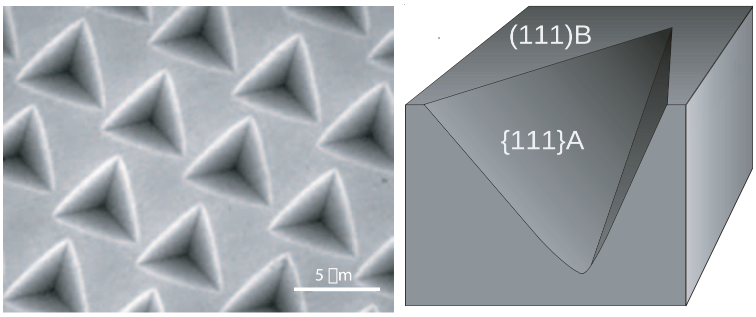

Figure 5.1: SEM top-view images of 5 μm pyramidal arrays. The characteristic tetrahedral pyramid pattern, exposing GaAs (111)A facets is obtained because this surface is resistant to the acid etch.

Low pressure OMCVD growth of InGaAs/AlGaAs heterostructures is then performed on the patterned substrate. The higher AlGaAs OMCVD growth rate on the (111)A facets leads to the formation of a very sharp corner and wedges ($<$ 10 nm radius of curvature) with self limiting profiles at the centre and the wedges of the pyramid. The first epitaxial layer ($Al_{0.75}Ga_{0.25}As$ nominal thickness 45 nm) is followed by 130 nm of $Al_{0.55}Ga_{0.45}As$. Subsequently 140 nm $Al_{0.30}Ga_{0.70}As$ with a 0.5 nm $In_{0.10}Ga_{0.90}As$ layer inserted at its centre and other 130 nm of $Al_{0.55}Ga_{0.45}As$ are grown. All thicknesses refer to growth on planar (100) substrates. The actual growth rate at the tip of the pyramid can be significantly higher (3 to 5 factor), and is actually governed by a complex interplay among surface diffusion on the (111)B planar surfaces, growth rate anisotropies on the different crystal planes, capillarity diffusion and entropy of mixing effects [49–52].

The growth process results in the formation of an InGaAs quantum dot (QD) connected to several types of low-dimensional barriers: InGaAs quantum wires (QWRs) on the edges of the pyramid, InGaAs quantum wells (QWs) on the (111)A facets and segregated $\sim$ $Al_{0.04}Ga_{0.96}As$ vertical quantum wire (VQWR) and $\sim$ $Al_{0.20}Ga_{0.80}As$ vertical quantum wells (VQWs) formed at the centre and at the pyramid edges (fig. 5.2).

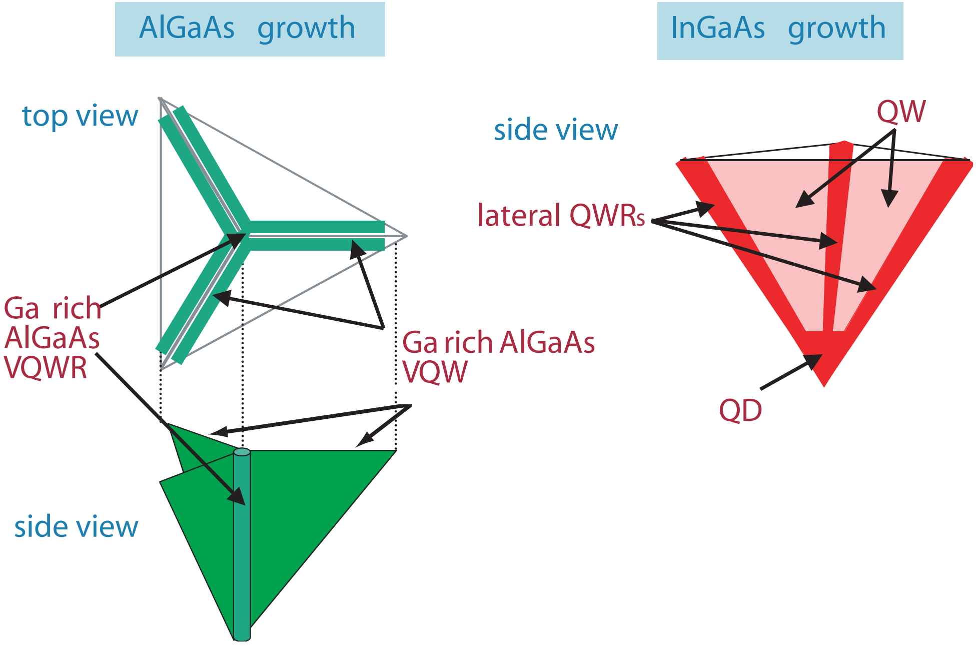

Figure 5.2: Schematic representation of the five heterostructures present in an InGaAs/AlGaAs pyramid. The InGaAs nanostructures are sandwiched between two $Al_{0.30}Ga_{0.70}As$ barrier layers. Ga rich VQWR and VQW self-order respectively at the centre and at the pyramid edges.

For time resolved cathodoluminescence experiments upright arrays of pyramids, containing the different nanostructures, are more useful for enhancing the collection efficiency of the luminescence due to the lens-shaped surface [53]. To achieve such upright pyramids, a back etching process has been developed, in which the GaAs substrate supporting the pyramid arrays has been removed. Figure 5.3 shows an array of such pyramids after the substrate removal step.

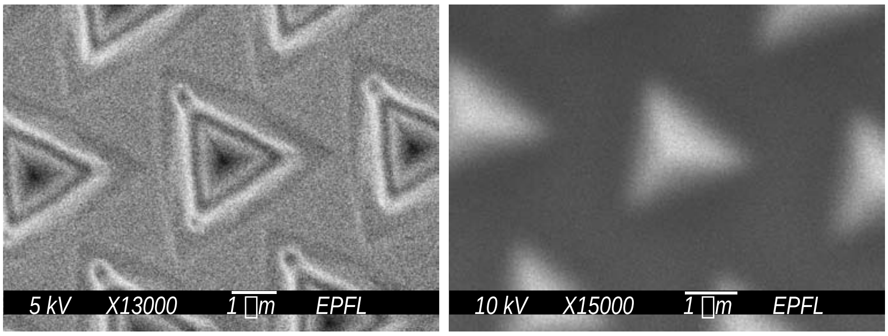

Figure 5.3: Left: low pressure OMCVD InGaAs/AlGaAs inverted tetrahedral pyramidal. Right: upright arrays of pyramids after back-etching process.

As a consequence of the back etching process the sample is not uniform. In regions where the acid action is stronger pyramids are "bigger" because the GaAs substrate is totally removed. Etching can damage pyramids in this part of the sample. Indeed we could not observe any luminescence emission from pyramids in this region. We carried out our experiments in other parts of the sample where pyramids emerge only partially from their substrate and they were not damaged by the acid (fig. 5.4). This same observation was confirmed by microPL experiments on the same sample performed in another laboratory [47].

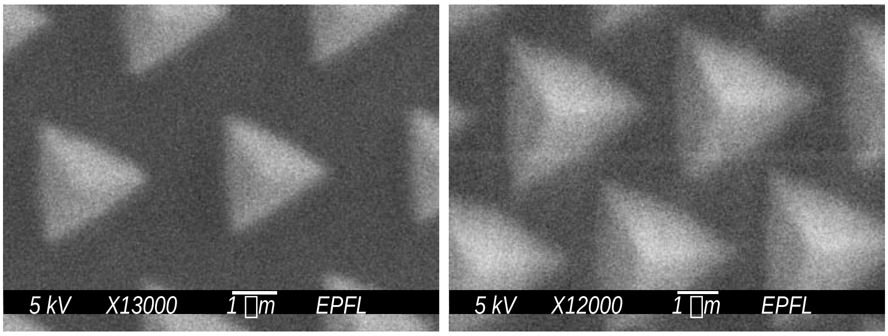

Figure 5.4: The back etching process is not uniform. Regions where the GaAs substrate was totally removed pyramids look bigger.

5.3 Continuous CL

We report in this section the continuous CL results on InGaAs/AlGaAs pyramids: the luminescence spectrum of the low dimensional heterostructures and CL images at the different emission wavelengths. We will see to which extent spectrally resolved cathodoluminescence imaging can help to identify some of the nanostructures spectral features. The procedure that was used to correlate peaks present in spectra to the different nanostructures will be briefly reviewed.

5.3.1 Luminescence spectrum

PicoCL experiments on InGaAs/AlGaAs pyramidal quantum structures were performed at a temperature of 90 K. The accelerating voltage was 10 kV and the exciting current was 10 pA i.e. $\sim$ 1 electron per pulse. Vacuum in the microscope specimen chamber was $1 \cdot 10^{-5}$ mbar.

The luminescence signal was focused on the monochromator input slit with a near infrared achromat (focal length of 100 mm). Spectra were recorded with a slit aperture of 200 μm and the 600 grooves/mm grating. This correspond to a resolution $\sim$ 2 nm (4 meV) at 800 nm. This value is largely sufficient for our purposes, at a temperature of 90 K we expect indeed a broadening of 7.5 meV.

The continuous CL spectrum was recorded with a thermoelectric cooled CCD (HAMAMATSU C 7041) that we used at the place of the streak camera (fig. 4.1). The advantage of using this CCD is the large active area (24.5 x 6 mm) that allows for registering at once a greater part of the diffracted luminescence with respect to the streak camera (active area 5.4 x 0.15 mm). The spectral features of the nanostructures under investigation extend from 1.93 to 1.48 eV (fig. 5.5). Even with the C 7041 we had to register it in two steps that were joined together at 1.74 eV (at the minimum between the lateral QWR and the VQW).

Spectrum reported on fig. 5.5 was integrated for 500 ms. It has been obtained while the electron beam was scanning over a field covered by one pyramid. The scan speed was the standard one that is equivalent to 142 ms per image. A background subtraction procedure was employed in order to have a high signal to noise ratio.

We clearly see five peaks. The one at the minimum energy (1.52 eV) will be associated to the QD. Its FWHM is 6.7 meV. The energy spread observed for it is consistent with the temperature at which we are working. Holes states in the dot are indeed separated by few meV and at temperatures between 80 to 100 K emission lines from it broaden. Peaks at 1.57, 1.66, 1.77, 1.90 eV correspond respectively to the VQWR, QWR, VQW, and the QW. We will discuss in the next sections how the spectral features of each nanostructure can be identified.

We determined also the carrier temperature by fitting with a Boltzmann function the high energy tail of the QWR emission. (we chose this last one because it has the longest tail and a fit can be performed over more than one decade of intensity variation). A carrier temperature of 120 K ± 8 K is found. This error was determined by varying the fitting points on the tail.

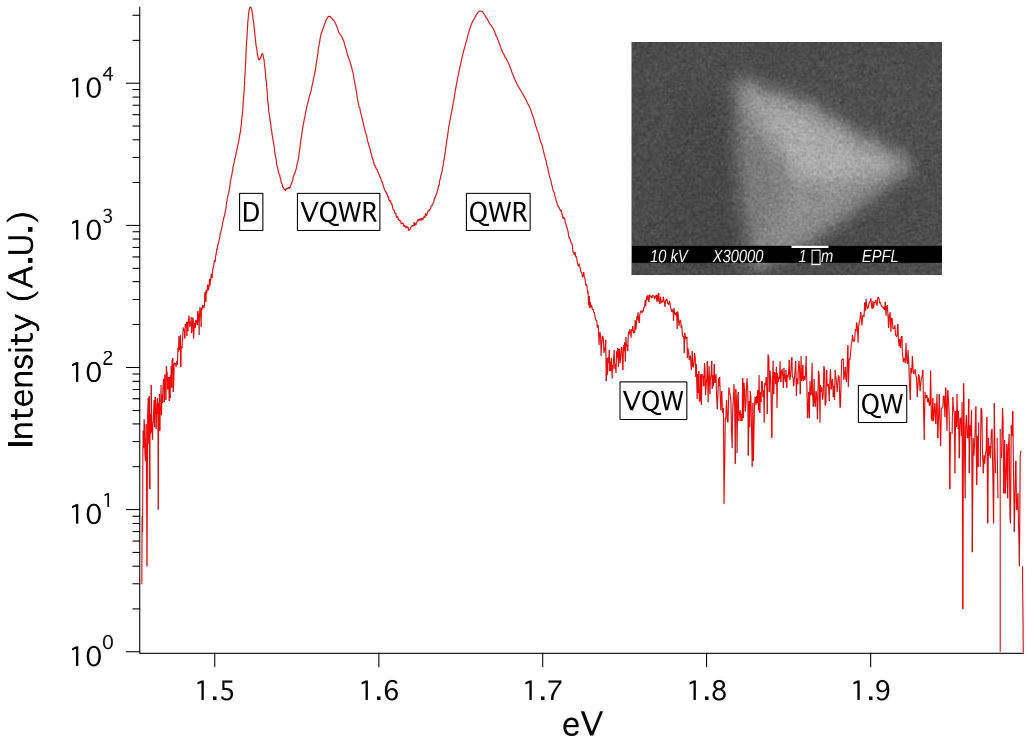

Figure 5.5: Luminescence spectrum from InGaAs/AlGaAs pyramidal quantum structures. Five peaks are clearly visible. They correspond to the five nanostructures formed in the pyramid. Inset: Image of the surface scanned by the electron beam while the spectrum was taken.

5.3.2 Spectrally resolved CL images

Spectrally resolved CL images of the pyramids are shown in figure 5.6. The input and the exit slit of the monochromator were closed to 400 μm in order to select $\sim$ 8 meV of the spectrum to be detected by the PM (fig. 4.1 and section 4.4.2). Then we registered an image for each of the five maxima present in the spectrum. Contrast and brightness were optimized for each picture to better evidence the emission pattern at the different wavelengths. All the images reported are from the same region of the sample with linear dimensions $\sim$ 25 μm x 30 μm.

CL imaging mode is useful to directly identify the 1.90 eV emission line with the InGaAs QWs grown on the (111)A facets. Emission from one facet looks uniform while pyramid edges and centre are dark.

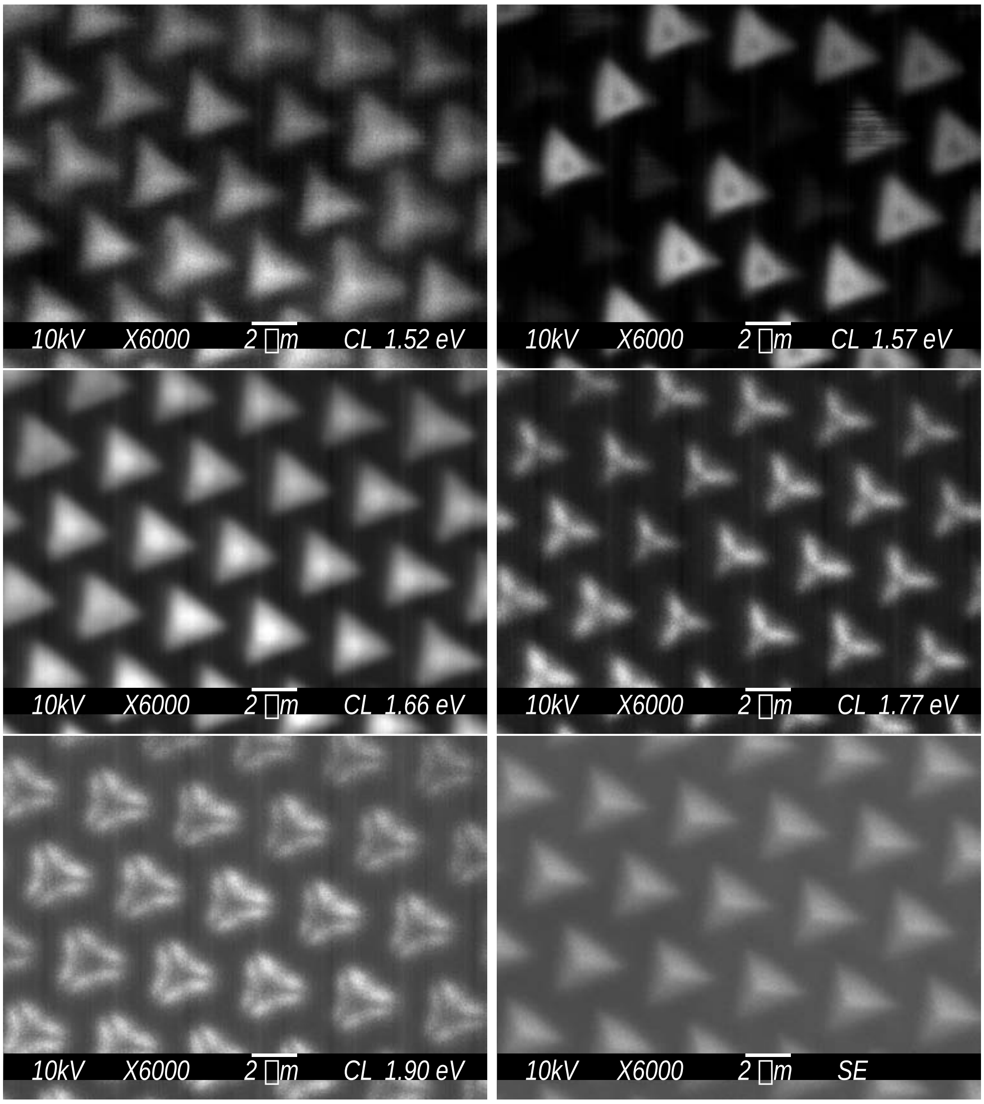

Figure 5.6: SE and monochromatic CL images from the same region of the sample. From top to bottom CL images centred at the QD, VQWR, QWR, VQW, QW emission wavelengths and the SE image used as reference.

Wavelength dispersive CL images do not allow for other attributions. Features at 1.57 and 1.77 eV can be attributed to the VQWR and the VQW because they also appear at the same energy in the control sample in which no InGaAs QW layer was grown [52]. Aluminium segregation in the VQWR is expected to be lower than in the VQW so the line at 1.57 eV is attributed to the VQWR. The CL image centred at 1.77 eV confirms that the VQW emits at this energy.

InGaAs heterostructures can be identified by their energy position and the expected InGaAs thickness, as determined using a simple square well model, neglecting lateral quantization [53]. Several other experiments, like excitation power dependent measurements, showing a strong saturation at high powers for the QD contribution, cleaved edge measurements and microPL line scans, were used to further corroborate these peak assignments [52]. It was also observed that the QD emission evolves as expected with dot thickness, with the ground state transition energy increasing with decreasing the dot thickness [48].

Our CL images relative to QD, QWR and VQWR can not be related in a direct way with the nanostructure location at the origin of the luminescence signal. This is typical for a CL experiment because the emission pattern does not depend only on the primary electron diffusion range but also on the carrier transport processes involved in these complex nanostructures (see section 4.5.3). The carriers diffusion length so limits the spatial resolution of the wavelength dispersive image. If we consider for instance the CL image at the QD emission line (1.52 eV), we observe that the emission pattern is the entire pyramid. This means that carriers find a path to diffuse towards the dot from all points of the pyramid.

Carrier mobility increases as a function of the temperature of the sample. Low temperature (10 K) spectrally resolved CL images of a slightly different sample, GaAs/AlGaAs heterostructures growth in the same regular matrix (5 μm pitch) of tetrahedral recesses, are reported in literature (fig. 5.7) [54]. In these images the QD, QWR, VQW and QW emissions are reported. The diameter of the QD image of 250 nm indicates a lateral diffusion length of less than 125 nm for carriers that are excited in the QD barriers and eventually recombine in the dot. These images provide another confirmation for the assignment of the luminescence transitions.

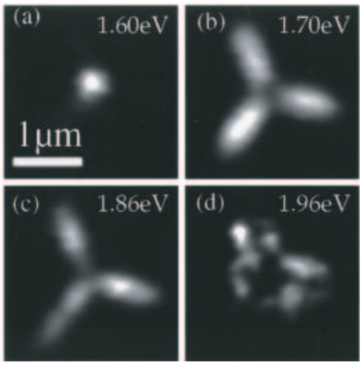

Figure 5.7: Monochromatic low temperature (10 K) CL images of a single pyramid with a nominal GaAs layer thickness of 1.5 nm [54].

5.4 Time resolved measurements

Time resolved experiments were carried out according to the following procedure. We excited with the electron pulses six different points on one pyramid and for each emission wavelength we studied the temporal response. The chosen points were: the top of the pyramid, the middle and the bottom of the pyramid edge, and three points on the pyramid facet. A colour code will be used to distinguish the luminescence emission from the different points (fig. 5.8).

As we already said in section 4.4.2, JEOL 6360 electron microscope is not provided with the spot mode function so we centred on the computer display the point to be analysed and we increased the microscope magnification to its maximum possible value (300.000X). In this way the excitation region was a square of 300 nm x 300 nm. Data reported in this section were all obtained with the same streak camera gain and are the result of 50 accumulations, each one integrated for 1557 ms. The luminescence beam that illuminated the 600 grooves/mm grating had a diameter of 1 inch, limiting the temporal resolution to 50 ps.

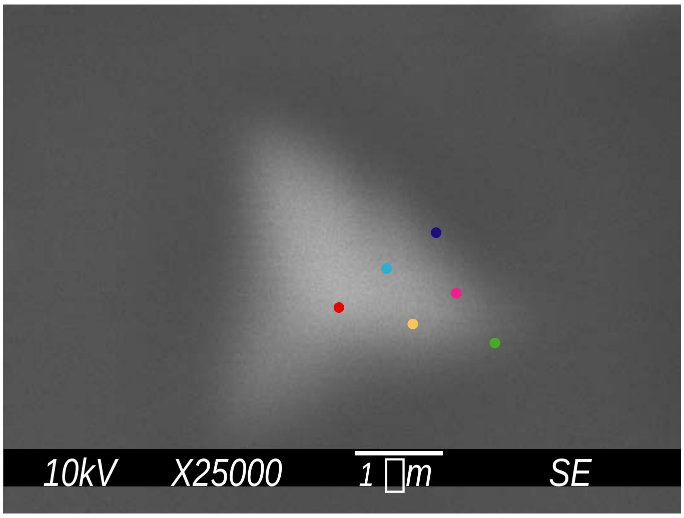

Figure 5.8: The six excitation points on a pyramid. The SE image is used as reference.

Two main results are found. Rise and decay times for the different emission wavelengths provide a strong confirmation of the peak attribution that was done with other techniques. More than that, experimental results suggest that carriers diffuse from the lateral structures (QW, VQW, QWR) towards the central structures (VQWR, QD) via the QWRs. As an example of the potentialities of the picoCL, a streak image, obtained when exciting the cyan point on the (111)A facet of the pyramid, is presented in fig. 5.9.

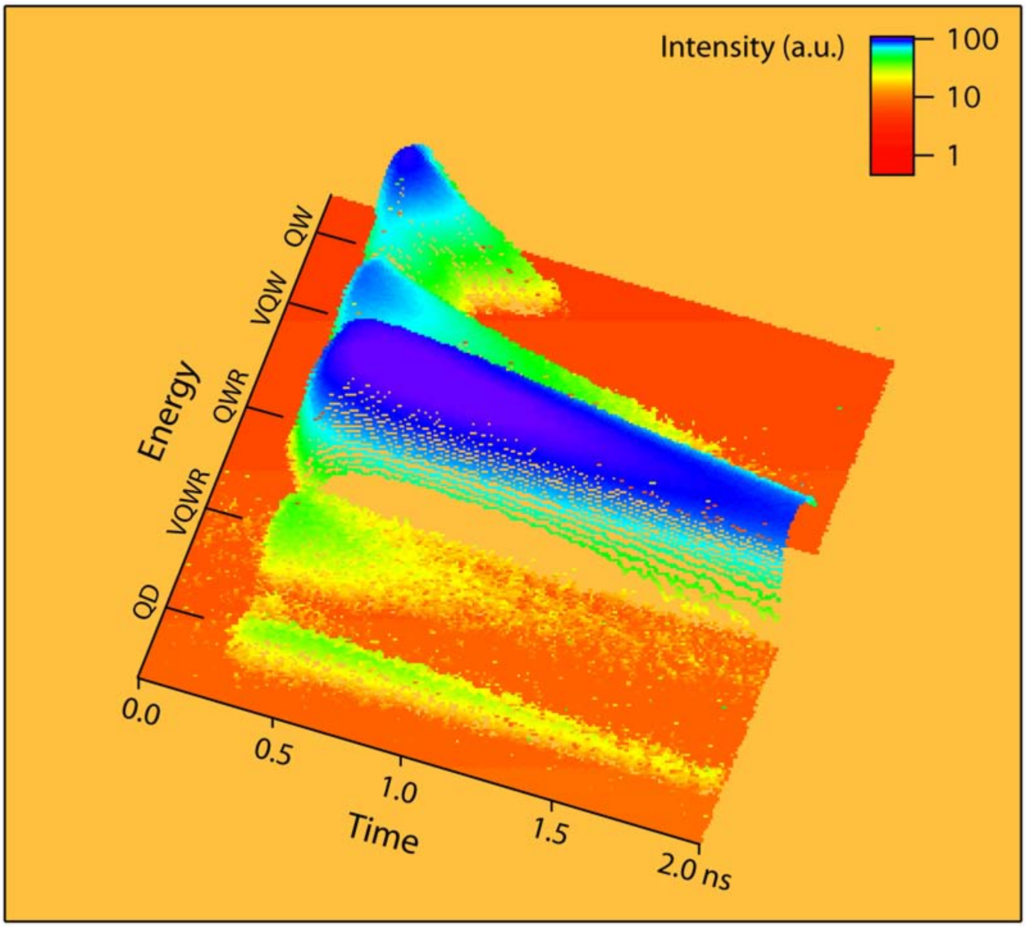

Figure 5.9: Streak image for one of the pyramids when excited at the center of the pyramid (111)A facet. The five different nanostructures display very different time behaviors that are signatures of the complex transport mechanisms within the pyramid.

5.4.1 QW

The temporal dependence of the QWs luminescence is reported on fig. 5.10. The continuous CL image, shown on fig. 5.6 and reported also in the fig 5.10 inset, suggests that the luminescence decay times for the QWs depend on the excitation point. The top and the edges of the pyramid look dark because of carrier capture in the other heterostructures. In these regions carriers from the QWs are trapped in the QWRs, VQWs, VQWR or the QD. As a consequence of this, we expect the QW decay time to be shorter at these points. Indeed if we compare the different excitation points (see table 5.1) we find that the decay time is 130 ps when we excite the top of the pyramid and it is 300 - 400 ps when the bottom of the facet is excited. Rise times are also interesting. They are defined as the time for the signal to rise from 10% to 90% of the maximum value. In this case the rise time represent the carrier capture from the AlGaAs barrier into the InGaAs QWs. Since the QWs are grown on all the (111)A facet we expect them to be all equal. Our experimental results validate this scenario.

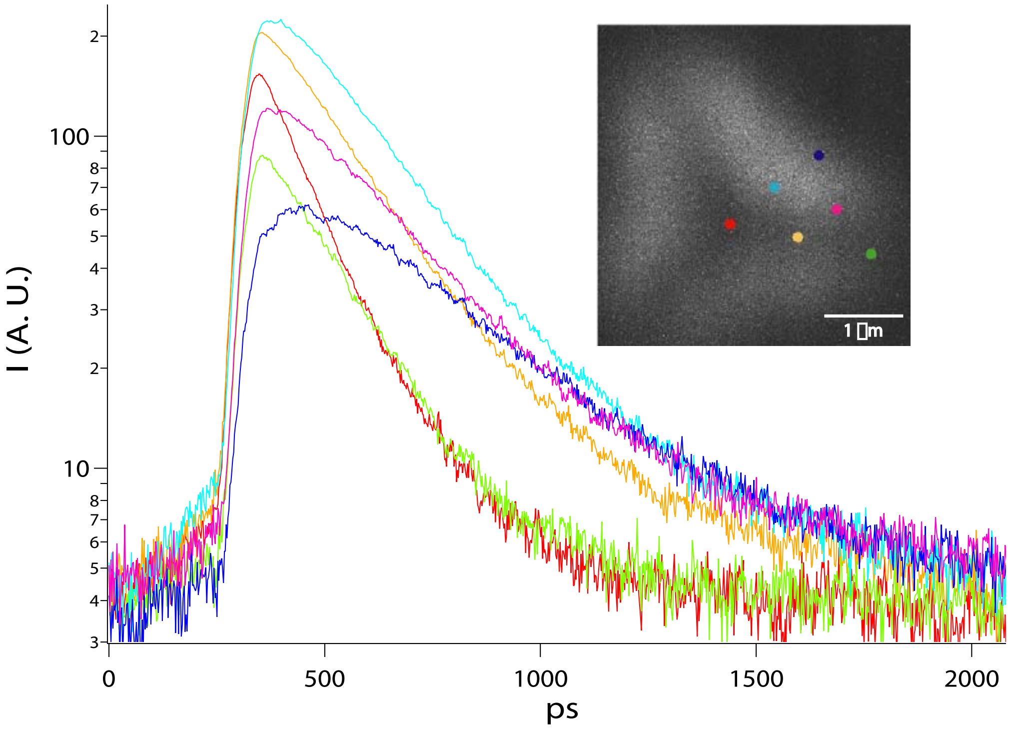

Figure 5.10: Temporal response of the luminescence signal emitted by the QW (emission centred at 1.90 eV). Colours correspond to the different excitation points.

Table 5.1 QW Data

	Red	**Orange**	**Green**	**Cyan**	**Magenta**	**Blue**
Rise time$_{10-90\%}$ (ps)	56	55	58	57	57	100
Decay time (ps)	130	210	210	240	290	400

5.4.2 VQW

PicoCL experiments (fig. 5.11) confirm that the luminescence signal at 1.77 eV is emitted by the VQWs. AlGaAs VQWs are formed (see fig. 5.2) at the pyramid edges. We expect that carriers diffuse more rapidly towards the VQWs when we excite a point on the pyramid corner than when we direct the electron beam on a facet.

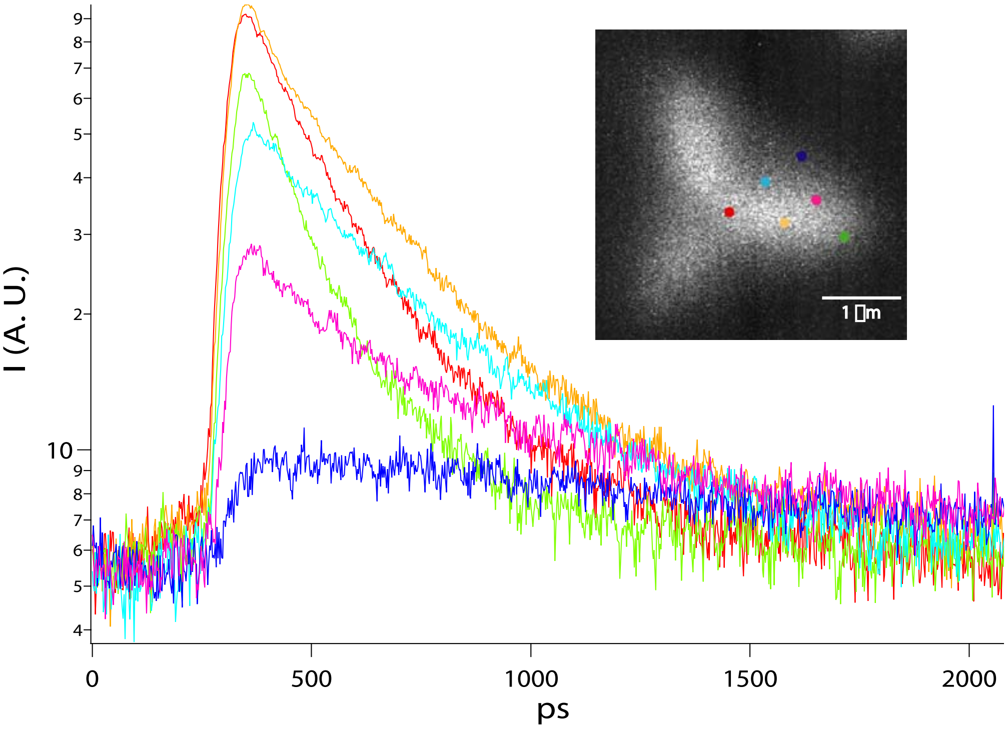

Figure 5.11: Temporal response of the luminescence signal emitted by the VQW (emission centred at 1.77 eV).

If we look at the rise and decay times at this wavelength, we observe that the rise times do not vary too much. Instead the decay times of the luminescence profiles increase with the distance of the exciting point from the pyramid edge, while the maxima of the intensity emission decrease. We interpret the rise time as the time the carriers take to leave the VQW because of carrier trapping in the QWR. The decay times represent here the carrier capture in the VQW and are mainly due to carrier diffusion.

Table 5.2 VQW Data

	Red	**Orange**	**Green**	**Cyan**	**Magenta**	**Blue**
Rise time$_{10-90\%}$ (ps)	51	55	53	68	65	~ 100
Decay time (ps)	190	260	130	330	340	

With a 10 kV primary excitation beam, electron-holes pairs are created within a volume of 300 nm [45] around the point of impact of the electrons i.e. mostly in the AlGaAs barriers of the structure. If we consider also the fact that in our case the primary electron beam scans a surface of 300 x 300 nm we can safely assume an electron-hole creation volume with a radius of 400 nm. Taking the decay times observed for the excitation points on the edge of the pyramid this imply a diffusion coefficient of the order of 10 cm^2/s corresponding to a mobility of of the order of 1000 cm^2/Vs at 90 K. This value seems indeed quite reasonable (see below).

5.4.3 QWR

InGaAs QWRs are located along the pyramid edges. We observe a difference in the rise time luminescence signal when the electron pulses are focused on the pyramid corner or on the pyramid facet (fig. 5.12).

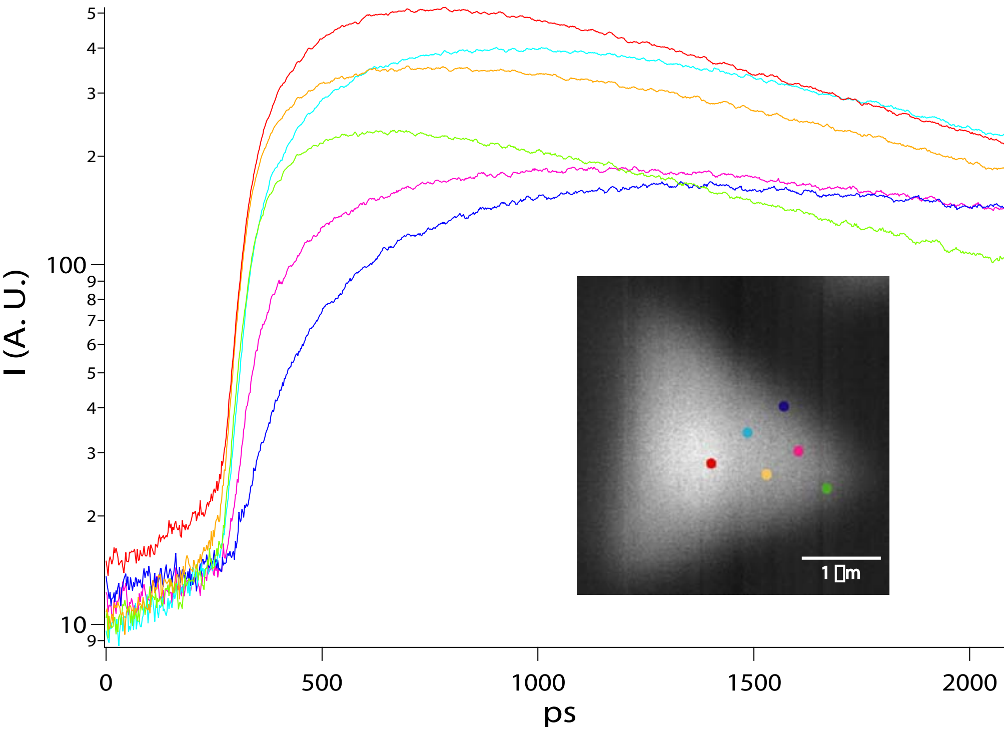

Figure 5.12: Temporal response of the luminescence signal emitted by the QWR (emission centred at 1.66 eV).

Rise times for the QWR are now clearly not relaxation limited. If we consider the three points along the pyramid edge, we explain this result with the carrier capture from the 400 nm excitation volume. For the three excitation points on the pyramid facet we have to consider the path that carriers travel to get trapped into the QWR.

The luminescence decay time is also longer with respect to the wells. We could estimate it only for the edge excitation points because in the other cases the signal is too long. The decay time that we observe is due to two important contributions: the carrier lifetime in the QWR and the carrier diffusion towards the central structures (see below).

Table 5.3 QWR Data

	Red	**Orange**	**Green**	**Cyan**	**Magenta**	**Blue**
Rise time$_{10-90\%}$ (ps)	250	230	180	350	470	640
Decay time (ps)	1420	1160	1430			

5.4.4 VQWR

Data for the VQWR are shown in fig. 5.13. The measured rise times confirm that the VQWR is a central structure. Indeed rise times increase with the excitation point distance from the pyramid centre because carriers have to travel a longer path to get there. Notice that this is the first case where we observe a difference in the rise times luminescence from excitation points located on the pyramid edges (Table 5.4).

Decay times for the VQWR are also very long. We clearly observe that luminescence from the VQWR is not zero during the return sweep of the streak camera that overlaps the signal of the main sweep (0-2 ns window) with the residual light emitted in the 6-8 ns window. This spurious signal is superposed to the main one with an inverted temporal scale. For this reason the luminescence present in our spectra before the pulse excitation, is the sum of the luminescence decay 8 ns after the pulse excitation plus the residual signal after 12 ns (i.e. the temporal distance between two exciting electron pulses).

It is important to observe that for all excitation points, except the one on top of the pyramid, the luminescence signal still increases after 2 ns. When we look at the lateral structures, the only luminescence signal that is not zero in the time interval between 1.5 and 2 ns is the QWR emission. The temporal response of the wells falls rapidly to zero with respect to the response of the other structures. This observation suggests the scenario that carriers diffuse towards the central structures via the QWRs. Later in this chapter we will develop a model that confirm this hypothesis.

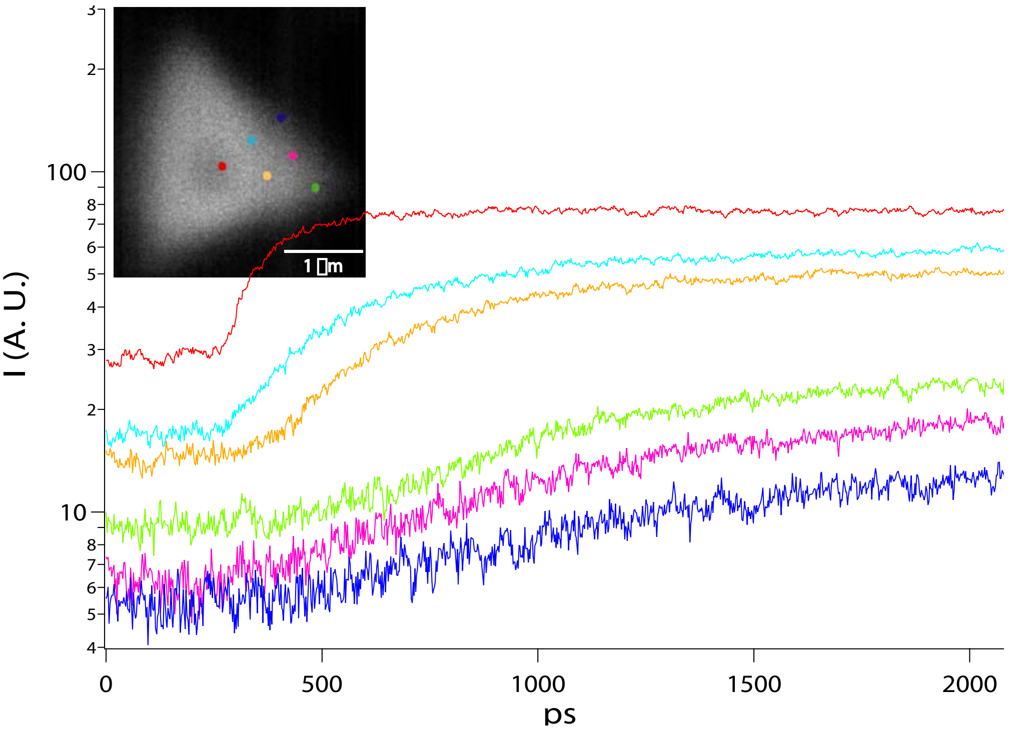

Figure 5.13: Temporal response of the luminescence signal emitted by the VQWR (emission centred at 1.57 eV).

Table 5.4 VQWR Data

	Red	Orange	Green	Cyan	Magenta	Blue
Rise time$_{10-90\%}$ (ps)	210	$\geqslant$ 870	$\geqslant$ 1100	$\geqslant$ 820	$\geqslant$ 1000	$\geqslant$ 1300

5.4.5 QD

The QD emission is saturated. Its luminescence is constant in time (fig. 5.14). As we saw in the previous section the VQWR has a very long lifetime. Carriers are not completely relaxed even after 8 ns. As long as carriers are present in the VQWR they can diffuse towards the QD and saturate it.

A way to avoid this problem is to reduce the temperature of the sample. Results published in literature show that the decay times for these quantum wires decrease considerably with temperature [55]. Other measurements will be performed when a He cryostat will be mounted on the set-up.

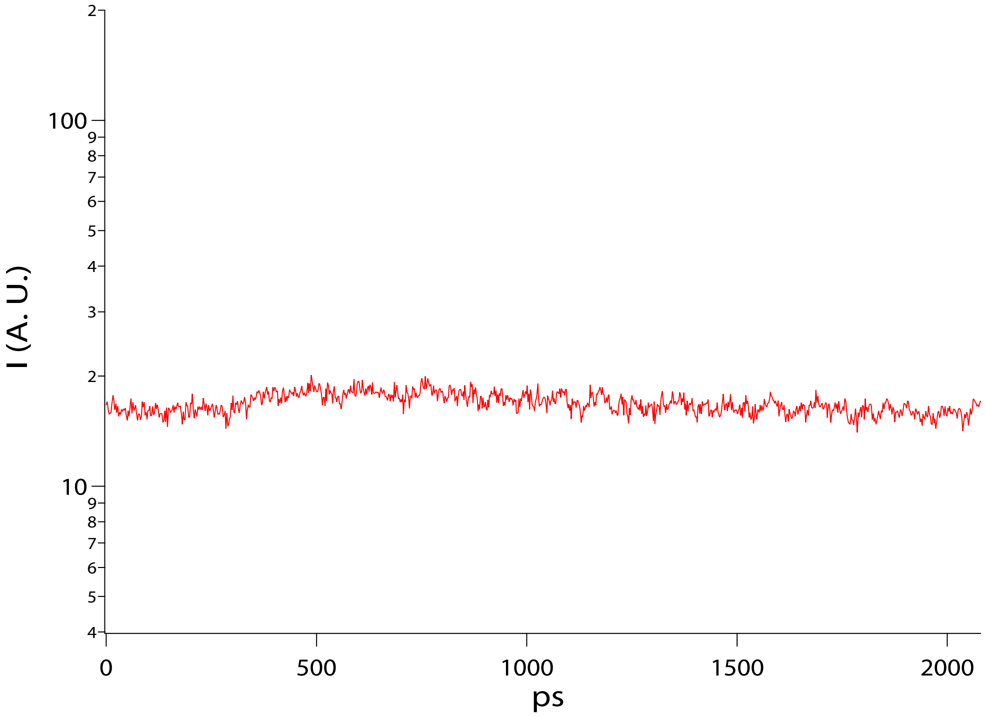

Figure 5.14: Temporal response of the luminescence signal emitted by the QD (emission centred at 1.52 eV). For each excitation point the dot was saturated.

We could anyway perform a measurement that confirms the attribution of the 1.52 eV emission to the QD. We analysed the luminescence emitted from a great number of pyramids. We finally found a few number of them where the QD was not saturated. They are placed in a region where the acid etch was quite strong. These pyramids are identified by their luminescence pattern. The intensity ratio of the luminescence peaks is different from that observed in the rest of the sample [53]. The QD and the VQWR emission are much weaker with respect to normal conditions (a factor 10 at least).

Figure 5.15 reports the temporal profiles for the QD luminescence in this particular set of pyramids. The only result that we want to retain from these graphs is the evidence that the rise time increases with the excitation point distance from the pyramid centre. Even if damaged by the acid etch these pyramids confirm that the 1.52 eV luminescence is emitted from the QD. We can safely conclude that picoCL allows for a detailed luminescence peak attribution of the nanostructures grown in InGaAs/AlGaAs pyramids.

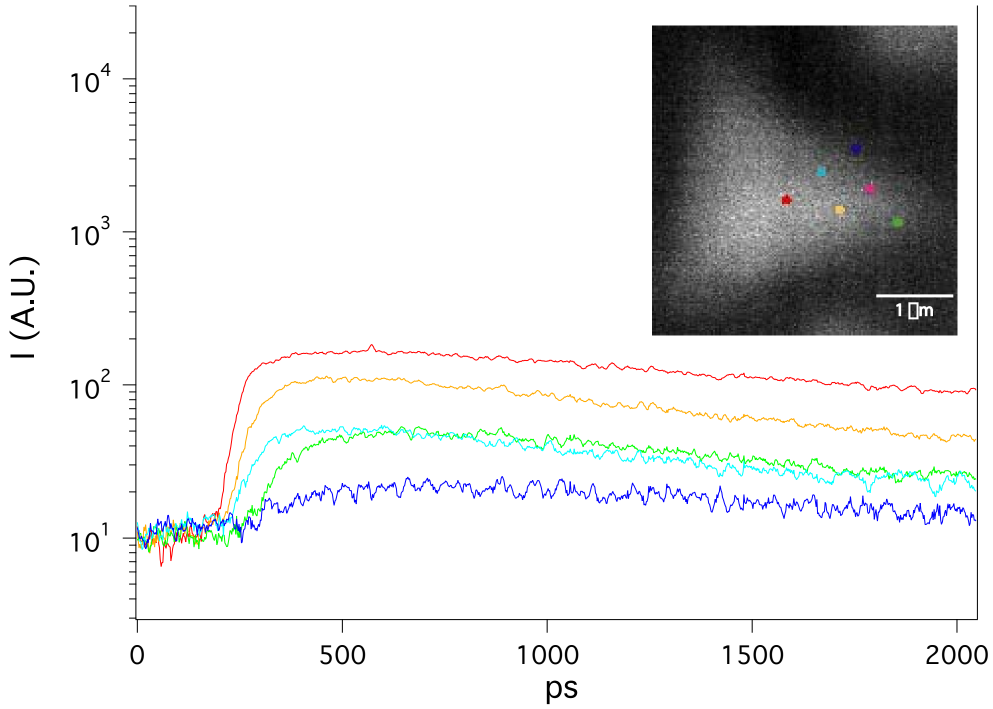

Figure 5.15: Temporal response of the luminescence signal emitted by the QD (emission centred at 1.52 eV). We performed these measurements on pyramids located in a region where the acid etch was quite strong.

5.5 Carrier transport

In the previous section we noticed that for all excitation points, except the one on top of the pyramid, the luminescence emission from the VQWR is still increasing even after 2 ns from the electron pulse excitation. At the same time if we look at the lateral structures, the only luminescence signal that is not zero in the time interval between 1.5 and 2 ns is the QWR emission. This allows us to suppose that carriers diffuse towards the central structures via the QWRs.

We develop here a simple model to describe the carrier transport in InGaAs/AlGaAs pyramidal quantum structures. We show how carrier diffusion in the QWRs can be used to simulate our data. In particular the model is successful in computing the carriers mobility in the QWR and in describing at the same time the population dynamics of the QWR and the VQWR.

5.5.1 Diffusion model

To gain insight into the transport properties of the QWR we focus our attention on the two excitation points located on the pyramid edge plus the excitation point on top of the pyramid. The wire length derived from our reference images (fig. 5.8) is 1.8 μm. This value must be corrected by considering the angle ($\sim 54°$) that the pyramid edge forms with the substrate, giving a QWR length of 3 μm.

The primary electron beam incident on a pyramid edge creates electron-hole pairs in all its interaction range, mainly in the AlGaAs barriers. The diffusion coefficients for electrons and holes are generally different. Electrons have a great mobility with respect to the holes. The charge separation induced by the difference in the diffusion coefficient accelerates holes and decelerates electrons. For this reason we will consider the ambipolar diffusion coefficient to model our data. To simulate all this, according to our discussion earlier, we make the assumption that in our model carriers are created in a reservoir and they take a time τ to be trapped into the QWR. Carriers in the QWR diffuse in a one dimensional system towards the central structures.

Equation 5.1 governs the number of carriers per unity length $u(x,t)$ located at time t and at point x in the reservoir

$$\frac{\partial u(x,t)}{\partial t} = -\frac{u}{\tau}. \tag{5.1}$$

As discussed earlier τ is much smaller that the carrier lifetimes of the QWR and the VQWR (see section 5.4.4 and 5.4.3). For this reason in equation 5.1 we neglect the carrier diffusion coefficient in the reservoir.

The initial spatial distribution $u(x,0)$ centred on the excitation point C is given by

$$u(x,0) = N_0 \frac{1}{\sqrt{2\pi}\sigma} \exp\left(-\frac{(x-C)^2}{2\sigma^2}\right) \tag{5.2}$$

where $\sigma = 400$ nm and N_0 fixed the total number of carriers that will be injected in the wire.

The number of carriers per unit length $n(x,t)$ in the QWR obeys the equation

$$\begin{aligned} \frac{\partial n(x,t)}{\partial t} &= D\frac{\partial^2 n(x,t)}{\partial^2 x} - \frac{n}{\tau_1} + \frac{u}{\tau} \\ n(x,0) &= 0 \end{aligned} \tag{5.3}$$

where τ_1 is carrier lifetime in the QWR. The diffusion coefficient D is related to the carriers mobility μ by the Einstein relation

$$D = \mu \cdot \frac{kT}{e} \tag{5.4}$$

where k is the Boltzmann constant, T is the sample temperature and e the electron charge.

A properly posed physical problem never consist of a partial differential equation alone; there must be additional boundary conditions to specify a unique solution to the problem. We chose a reflecting barrier [56] at the end of the QWR (point B see fig. 5.16)

$$\left.\frac{\partial n(x,t)}{\partial x}\right|_{x=B} = 0 \tag{5.5}$$

and an absorbing barrier at the top of the QWR (point A)

$$n(A,t) = 0 \tag{5.6}$$

The flux of particles absorbed by A is [57]

$$J = -D \cdot \left.\frac{\partial n(x,t)}{\partial x}\right|_{x=A} \tag{5.7}$$

A fraction of these is captured by the VQWR and the rest is reflected back in the QWR. (A condition easy to treat for a numerical solution, see appendix A.)

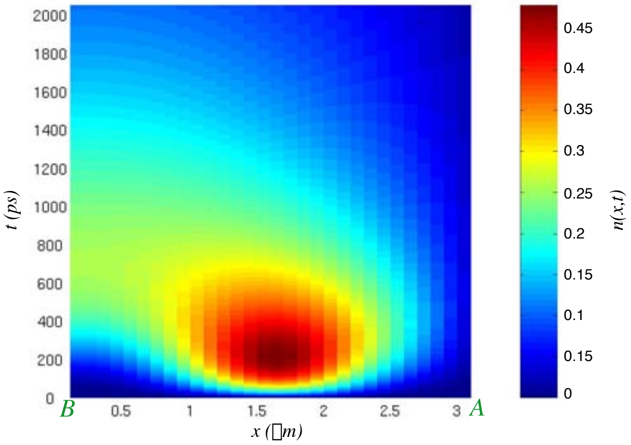

Figure 5.16: Diffusion pattern in the QWR. B is the reflecting barrier and A is the absorbing one. For the numerical solution the wire was discretized in 30 steps of 100 nm length.

If we look at the temporal profile of the luminescence emission for the VQWR when we excite the top of the pyramid, we observe that it is rather constant in time (fig. 5.13). This fact suggests the hypothesis that it is saturated. (As we will see in a next section our simulations confirm this hypothesis.) In this case we are forced to consider the number of free states in the VQWR when we compute the number J_1 of carriers trapped by this wire in the time interval $t, t+dt$

$$J_1 \cdot dt = -D \cdot \left.\frac{\partial n(x,t)}{\partial x}\right|_{x=A} \cdot \left(1 - \frac{N(t)}{N_{sat}}\right) \cdot dt \tag{5.8}$$

In this last equation $N(t)$ is the population in the VQWR, N_{sat} is the maximum number of carriers that can be captured in the VQWR and J_1 is proportional to the fraction of VQWR free states.

The rate equation for the VQWR population is

$$\begin{aligned} \frac{dN(t)}{dt} &= J_1 - \frac{N(t)}{\tau_2} \\ N(0) &= \mathbb{N}_0 \end{aligned} \tag{5.9}$$

where τ_2 is the carrier lifetime in the VQWR and $\mathbb{N}_0$ is the number of electron-hole pairs eventually present in the wire when the next excitation pulse arrives onto the pyramid (see section 5.4.4).

In order to compare the results of our simulations with the experimental data, we have to compute the number of photons emitted by the QWR (I_{QWR}) and the VQWR (I_{VQWR}) in the time interval $t, t+dt$

$$I_{QWR}(t) = \frac{\int_{QWR} n(x,t) \cdot dx}{\tau_1^r} \tag{5.10}$$

$$I_{VQWR}(t) = \frac{N(t)}{\tau_2^r} \tag{5.11}$$

where τ_1^r and τ_2^r are the radiative lifetimes. We will start by neglecting the non-radiative lifetimes and setting $\tau_1^r = \tau_1$, $\tau_2^r = \tau_2$. As we will see later if we relax these conditions, we do not modify the temporal profile of the luminescence emission but only the QWR and VQWR intensities.

5.5.2 Numerical solution

One of the principal strategies used in numerically solving problems such as equation 5.3 is the finite-difference method. It involves a discretization of space and time in steps of fixed size as follows (fig. 5.16):

$$\begin{aligned} t_j &= j \cdot k \qquad 1 \leqslant j \leqslant m \\ x_i &= i \cdot h \qquad 1 \leqslant j \leqslant p \end{aligned} \tag{5.12}$$

The next step in the process is to replace the differential problem by a discretized version of it [58]. For instance equation 5.3 is approximated with

$$\frac{n_{i,j+1} - n_{i,j}}{k} = D \cdot \frac{n_{i-1,j} - 2n_{i,j} + n_{i+1,j}}{h^2} - \frac{n_{1,j}}{\tau_1} + \frac{u_{i,j}}{\tau} \tag{5.13}$$

where $n_{i,j}$ stays for $n(x_i, t_j)$.

In our simulations we chose k = 2 ps, h = 100 nm. The choice of the length of the spatial and temporal step is not totally free. The finite-difference algorithm to be stable demands the condition

$$\frac{Dk}{h^2} \leqslant \frac{1}{2} \tag{5.14}$$

to be verified. Finally it is recommended to check the invariance of the solution on the length of the steps by varying them. The explicit algorithm we used to solve the set of equations for the diffusion model is reported in appendix A.

5.5.3 Carrier lifetime τ_2

Our experimental results suggest that the carriers lifetime τ_2 for the VQWR is not shorter than some nanoseconds. In figure 5.13 we clearly observe that luminescence from the VQWR is still present during the return sweep of the streak camera that overlaps the signal of the main sweep (0-2 ns window) with the residual light emitted in the 6-8 ns window. This spurious signal can cause problems for the data interpretation. In this section we describe the procedure used to analyze our results.

Let us first admit that we have just one population dynamics in the VQWR. In this case it is quite easy to subtract the overlapped signal to the 0-2 ns window. During the 6-8 ns temporal window all carrier populations in the lateral structures are zero. In this case we can safely assume that, in this time interval, the decay signal $I(t)$ from the VQWR is

$$I(t) = A \exp\left(-\frac{t}{\tau_2}\right) \qquad 6 - 8 \textit{ ns window} \tag{5.15}$$

where the constant A is fixed by the luminescence signal present in the spectrum before the excitation pulse arrival. The light intensity I_0 at that time is the sum of the luminescence decay 8 ns after the pulse excitation plus the residual signal after

12 ns

$$I_0 = A \cdot \left(\exp\left(-\frac{8}{\tau_2\ (ns)} \right) + \exp\left(-\frac{12}{\tau_2\ (ns)} \right) \right) \tag{5.16}$$

to give

$$I(t) = \frac{I_0}{\left(\exp\left(-\frac{8}{\tau_2}\right) + \exp\left(-\frac{12}{\tau_2}\right) \right)} \cdot \exp\left(-\frac{t}{\tau_2} \right) \qquad 6-8\ ns\ window \tag{5.17}$$

A graph of $I(t)$, for different choices of τ_2, is reported in figure 5.17. The same graph reports the result of the subtraction of $I(t)$ from the experimental data obtained when we excite the top of the pyramid. (We subtract the spurious signal due to the return sweep of the streak camera.)

The graph shows how a lifetime $\tau_2 \leqslant 4$ ns is not acceptable. The luminescence signal would have a non-physical behaviour. The hypothesis of a single population dynamics is compatible with $\tau_2 \sim 5$ ns. Values of $\tau_2 \geqslant 6$ ns are not acceptable because in this case the luminescence intensity after 8 ns would be greater than measured

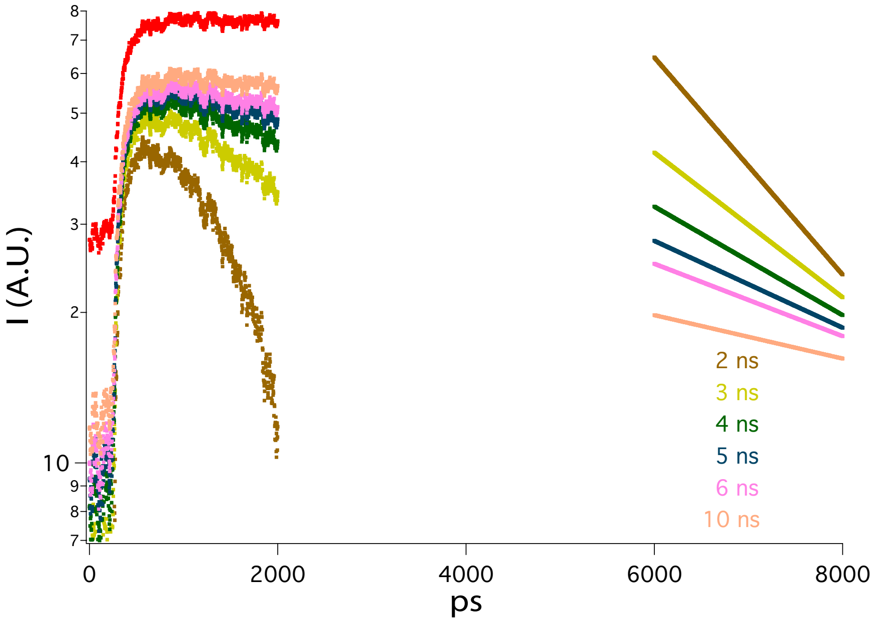

Figure 5.17: The red curve is the VQWR temporal response when we excite the top of the pyramid. We subtract to this curve the signal due to the return sweep of the streak camera. This same signal (reported on the graph) is what we expect to observe in the 6-8 ns temporal window (formula 5.17).

Of course we cannot exclude the possibility of having more than one population with different dynamics. In this case the tail we observe could be due to a very long decay time $\tau_2 \geqslant 6$ ns.

In the following we will use the model developed in the previous section to simulate our experimental data. First of all we will consider the case of a mono-exponential decay and we subtract the 5 ns exponential decay relative to the return sweep of the streak to the VQWR signal. After this we will assume to have two populations. In this case we will make the extreme hypothesis of a very long carrier lifetime for one of the two (we will subtract a constant signal). The carrier mobility in the QWR will be a value in between those found for these two cases.

5.5.4 Simulation results

The main parameters that characterize our diffusion model are the rise time τ for the QWR, the lifetimes τ_1, τ_2 and the carrier mobility in the QWR. According to the previous section we begin by choosing $\tau_2 = 5$ ns. The best fit to our results is obtained by setting $\tau = 150$ ps, $\tau_1 = 2$ ns and $\mu = 1400\ \mathrm{cm}^2/\mathrm{V}\cdot\mathrm{s}$.

Figure 5.18 shows the fit for the temporal profile of the luminescence emitted by the QWR. The intensities of the experimental curves differ when we move from an excitation point to another one. We explain this observation with a different number of carriers injected in the QWR in the three cases that we are considering. To take account of this fact we vary the parameter N_0 in the model to have 1700 carriers injected in the wire when we excite the top of the pyramid and 1100 and 600 for points on the middle and on the bottom of the pyramid edge. In our model the absolute value of N_0 is totally arbitrary, only ratios between different values of N_0 are important.

The algorithm we developed also computes the temporal dependence of the VQWR emission (fig. 5.18). The fit is very good. In particular it is important to note that we are successful in reproducing the intensity ratios for the VQWR curves once we have set those for the QWR. As we said in section 5.5.1 a good fit for the VQWR imposes the hypothesis of wire saturation. Appendix B shows the results we obtain without this hypothesis.

Figure 5.19 reports the results of the fit when we subtract to the experimental curves a continuous signal rather than an exponential one. In this case we are assuming that we have two population dynamics in the VQWR. This procedure proves to be very useful in estimating the error we do when we compute the carrier mobility in the QWR. In this case we set $\tau = 150$ ps, $\tau_1 = \tau_2 = 2$ ns to find the best fit for a carrier mobility of $1200\ \mathrm{cm}^2/\mathrm{V}\cdot\mathrm{s}$.

In conclusion we have demonstrated that in InGaAs/AlGaAs pyramids carriers diffuse from the lateral structures towards the central structures via the QWR. A mobility $\mu = 1300 \pm 100\ \mathrm{cm}^2/\mathrm{V}\cdot\mathrm{s}$ is found.

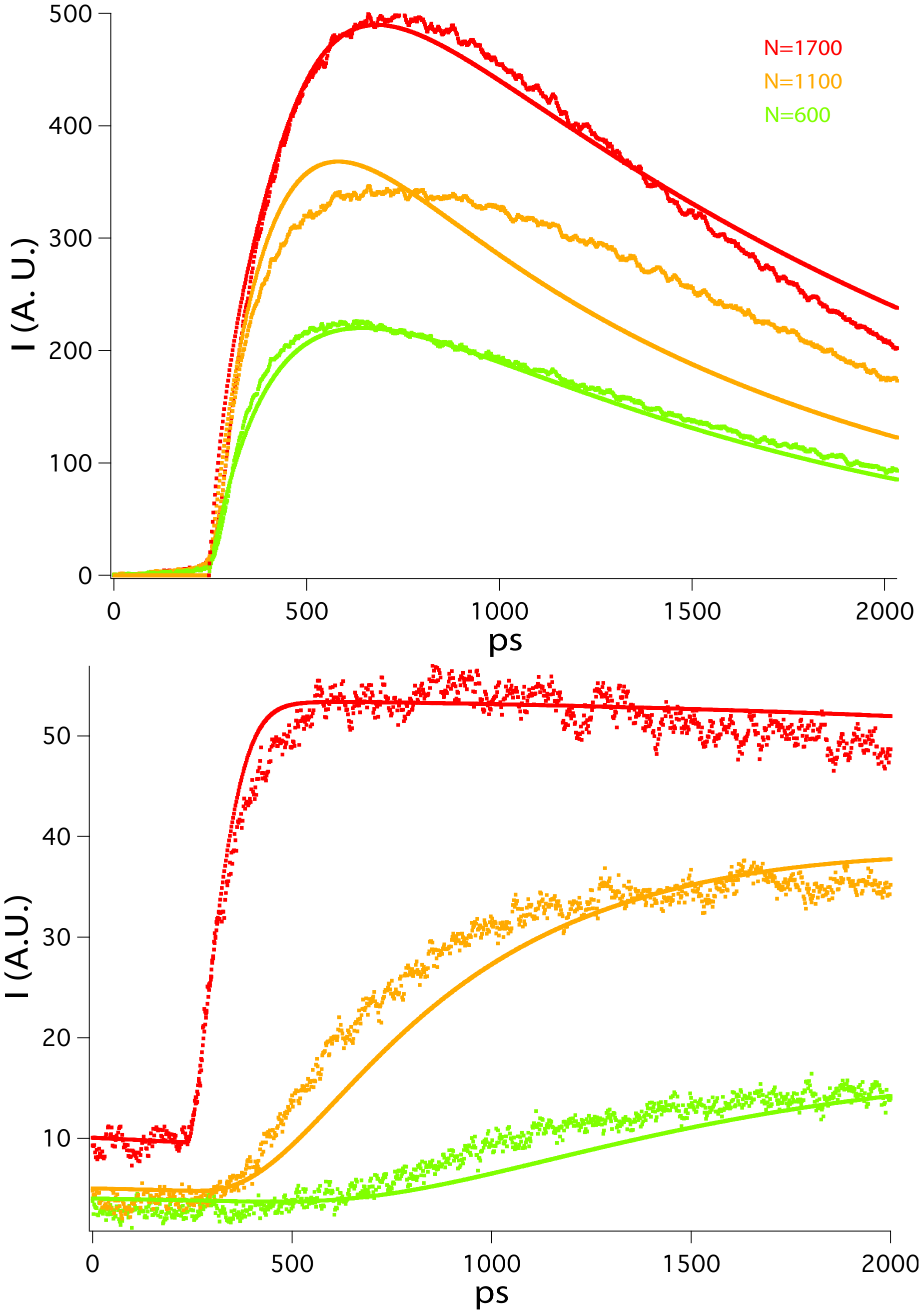

Figure 5.18: Fit of the experimental data in the hypothesis of one population dynamics. Top: QWR. Bottom: VQWR.

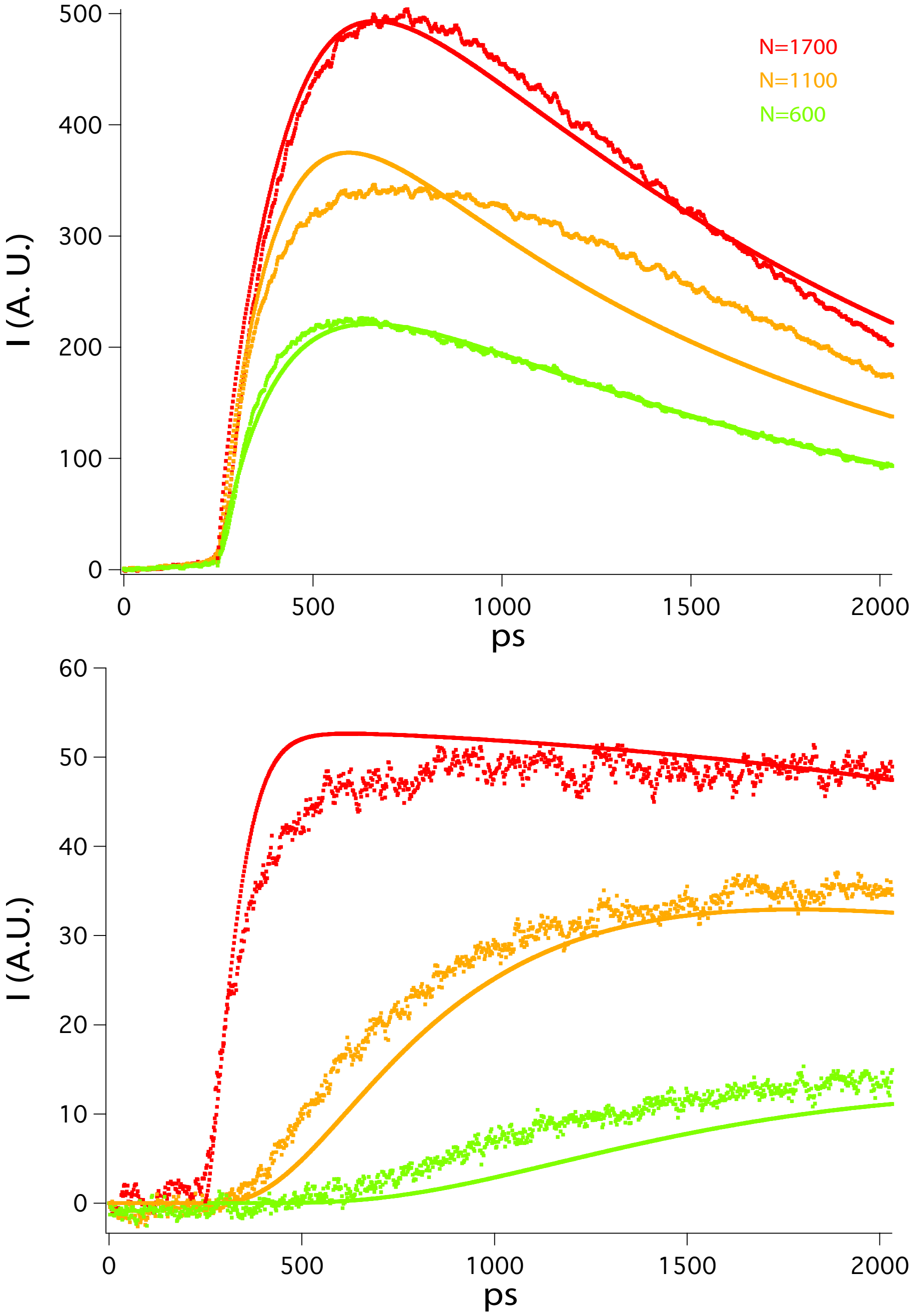

Figure 5.19: Fit of the experimental data in the hypothesis of two population dynamics. Top: QWR. Bottom: VQWR.

5.5.5 VQWR radiative lifetime

We now want to compare the intensity ratio

$$\frac{I_{VQWR}(t)}{I_{QWR}(t)} \tag{5.18}$$

of the VQWR luminescence with that of the QWR. Our model gives a value 1.5 greater than that observed experimentally (fig. 5.20). This indicates that the condition $\tau_2^r = \tau_2$ (see section 5.5.1) is not valid. In order to have the correct intensity ratio, without varying the population dynamics in the wires, from equation

$$\frac{1}{\tau_2} = \frac{1}{\tau_2^r} + \frac{1}{\tau_2^{nr}} \tag{5.19}$$

where τ^r stays for radiative lifetime and τ^{nr} stays for non-radiative lifetime, we obtain

$$\tau_2^r = 1.5 \cdot \tau = 7.5\ ns \qquad \tau_2^{nr} = 15\ ns \tag{5.20}$$

These results are valid if the other condition $\tau_1^r = \tau_1$ is true. Our experimental data do not allow for extracting any information about the radiative lifetime for the QWR. The carrier diffusion towards the central structures alters indeed the QWR decay time. As a consequence of this we can only set:

$$\tau_1^r \geqslant \tau_1 \qquad \tau_2^r \geqslant 7.5\ ns \qquad \tau_2^{nr} \leqslant 15\ ns \tag{5.21}$$

To conclude this chapter, we were able to fit our experimental data with the following parameters:

Table 5.5 Fitting parameters

Carrier mobility	μ	1300 cm^2/V · s
QWR rise time	τ	150 ps
QWR lifetime	τ_1	2 ns
VQWR lifetime	τ_2	5 ns
QWR radiative lifetime	τ_1^r	2 ns
VQWR radiative lifetime	τ_2^r	7.5 ns
VQWR non-radiative lifetime	τ_2^{nr}	15 ns

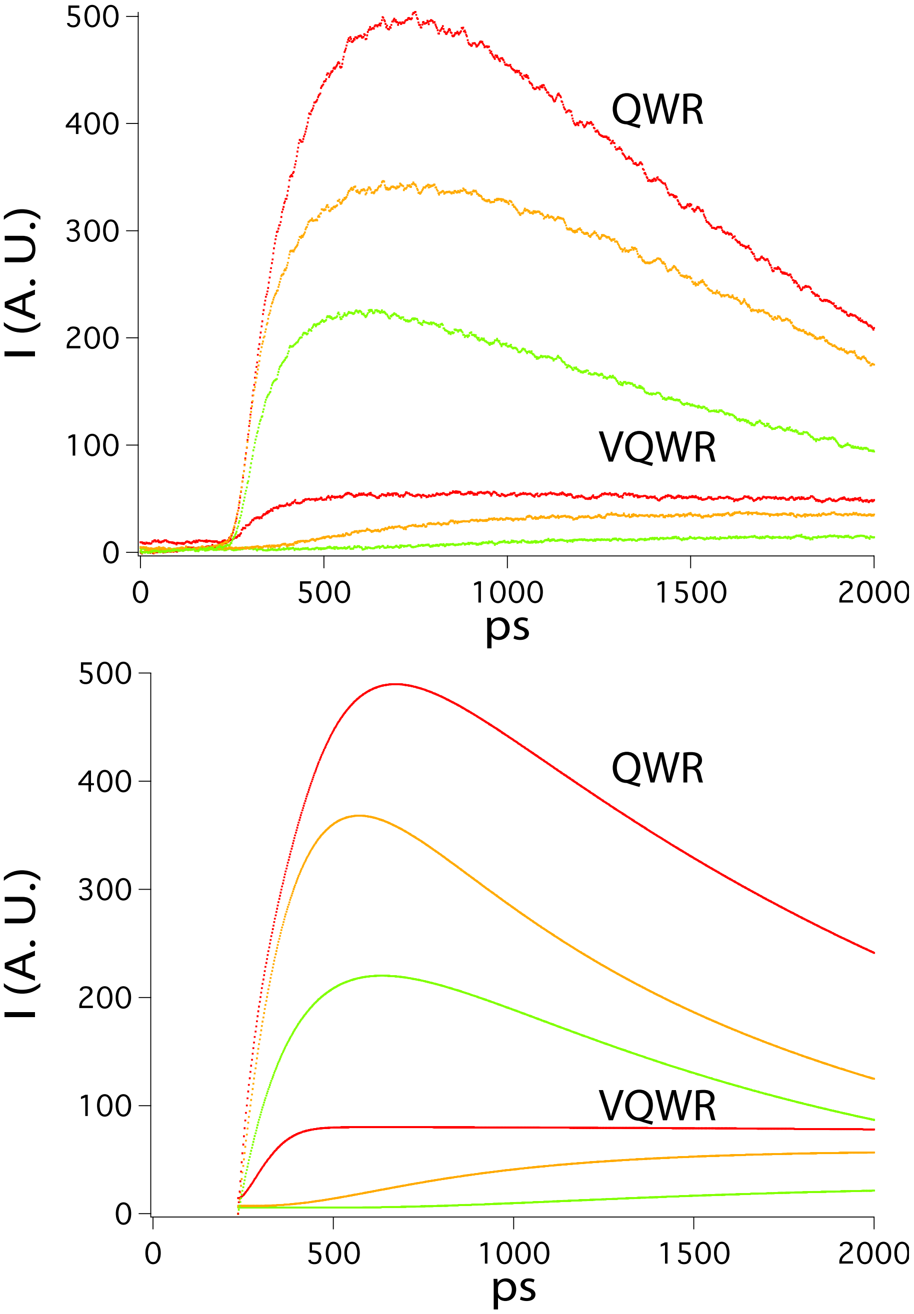

Figure 5.20: Experimental and theoretical data on the same graph. The difference in the intensities ratios is due to the fact that we did not consider the non-radiative lifetimes.

5.6 Conclusion

PicoCL has been used to investigate the optical properties and the carrier transport in quantum structures located in InGaAs/AlGaAs tetrahedral pyramids. An InGaAs quantum dot formed just below the top of the pyramid is connected to several types of low-dimensional barriers: InGaAs quantum wires on the edges of the pyramid, InGaAs quantum wells on the (111)A facets and segregated AlGaAs vertical quantum wire and AlGaAs vertical quantum wells formed at the centre and at the pyramid edges.

PicoCL experiments were performed at a temperature of 92 K, an accelerating voltage of 10 kV and a beam probe current of 10 pA. The continuous CL spectrum shows five luminescence peaks. PicoCL allows for an unambiguous luminescence peak attribution to the different nanostructures grown in a pyramid. Spectrally resolved CL images clearly identify the peak corresponding to the InGaAs QWs. The CL images relative to QD, VQWR, QWR, and VQW cannot be directly related with the nanostructure location at the origin of the luminescence signals. This is typical for CL experiments because the emission pattern does not depend only on the primary electron diffusion range, but also on the carrier transport processes in these complex nanostructures.

Time resolved measurements provide valuable information for a safe peak attribution. We have used electron pulses to excite six different points on the pyramid: three located on the pyramid edge and three located on the pyramid facet. Rise and decay times for the different emission energies are strongly dependent on the excitation point location and can be correlated to the carrier capture and relaxation processes in the different nanostructures and to the carrier diffusion mechanism in the pyramid.

In particular, except for the excitation point on top of the pyramid, we observe that the VQWR luminescence signal still increases after 2 ns (the maximum streak camera temporal window). When we look at the lateral structures, the only luminescence signal that is not zero in the time interval between 1.5 and 2 ns is the QWR. The temporal response of the wells (QW and VQW) falls rapidly to zero with respect to the response of the other structures. This observation, together with the VQWR rise time behaviour, suggests a scenario where carriers move towards the central structures via the QWR.

According to this hypothesis we have modelled the carrier diffusion along the QWR. We are successful in fitting the luminescence response of the QWR and of the VQWR. The best fit is obtained by assuming the lifetime of the VQWR and QWR to be 5 and 2 ns respectively, and the carrier mobility in the QWR to be 1300 $\mathrm{cm}^2/\mathrm{V} \cdot \mathrm{s}$. This value is of the same order of the carrier mobility in the AlGaAs barriers, as estimated from the decay time of the VQWs. Our result is similar to experimental diffusion coefficients in QWRs published in literature [59].

6 Conclusion and perspectives

We have developed a new spectroscopic tool (PicoCL) to perform time resolved experiments on a single semiconductor nanostructure. A home-made high brightness picosecond electron gun replaces the thermionic electron gun of a commercial SEM. Electron pulses of 12 ps temporal width, 80 MHz repetition rate, are focalized on a probe diameter of 50 nm to study transport and carrier dynamics at the nanoscale level. A monochromator and a streak camera perform spectral and temporal analysis of the luminescence emitted as a consequence of the electron beam excitation. These strengths combined with the imaging capabilities of a SEM allows for correlating the temporal profile of the luminescence emission from a nanostructure with its intrinsic properties and its nano-environment.

Studying the optical properties and the carrier transport in InGaAs/AlGaAs tetrahedral pyramidal quantum structures highlights the performances of this new technique. PicoCL is successful in identifying the spectral features of the different nanostructures and to explain the carrier diffusion mechanism is such a complex system.

With the rapid development of technologies for the fabrication of low-dimensional structures, the number of possible investigations with this original characterization tool is impressive. Due to its high versatility PicoCL can be used to study every semiconductor material, even those with a very wide band gap such as diamond, gallium nitride, zinc oxide, or more exotic materials like carbon nanotubes and polymeric chains.

As an example of possible study it is well known that today blue LEDs based on InGaN film, sandwiched between p-type aluminium gallium nitride and n-type gallium nitride, all grown on a sapphire substrate, are commercial available. The large mismatch between GaN and sapphire induces up to 10^{10} dislocations per cm^2 in such devices [60]. While in conventional III-V compound semiconductors like gallium arsenide or indium phosphide, the dislocation density must be less than $10^3 \cdot \mathrm{cm}^{-2}$ to achieve high efficiencies, InGaN devices are less sensitive to dislocations. A very nice study with the picoCL could be to image a dislocation in an InGaN or GaN film by the CL imaging mode of the system, and then to collect the time resolved emission from different points around it in order to investigate the electron-hole recombination around this non-radiative centre.

The equilibrium structure of GaN is wurtzite (hexagonal). Anyway it has been demonstrated that it is possible to produce layers of the metastable zinc-blende (cubic) phase and to grow micrometer-size nominally undoped h-GaN and c-GaN crystals [61]. Carrier recombination in GaN is strongly influenced by the presence of electric field due to piezoelectricity induced by lattice-mismatched layers and, in the case of the wurtzite phase also by a strong spontaneous polarization. The electric field separates the electron and hole wavefunctions with an increase of the radiative lifetime. PicoCL experiments on hexagonal and cubic-GaN microcrystals could be helpful in studying the properties of this material.

PicoCL can be used to investigate the carbon nanotubes properties. A room-temperature transistor based on a single semiconductor carbon nanotube was reported some year ago [62]. Single walled carbon nanotubes (SWNTs) can be used as building blocks for molecular electronics. Despite the predicted direct band gap character of semiconductor SWNTs, experimental observation of band-gap photoluminescence and electroluminescence was not easy to obtain. Still the radiative and nonradiative relaxation pathways in SWNTs remain poorly understood [63].

The strengths of PicoCL can be further improved. A SEM produces a small electron probe at the specimen by demagnifying the gun crossover. A way to improve the performances of PicoCL is to develop an electron optical column optimized for the picosecond electron gun. The crossover axial position of a thermionic gun varies in a different way with respect to the picosecond electron gun. More than this, in modern SEMs, user has no access to the currents circulating in the microscope column lenses and so to focal lengths. Electron lens stages designed for the PicoCL set up may improve the system performances.

The picosecond gun brightness could be increased by using other photocathode materials like K_2CsSb or Cs_2Te. These materials are anyway very sensitive to contamination and require in situ deposition. At present in our laboratory we are testing a fiber based electron gun. The photocathode is a gold film deposited on a fiber core. Even if the gun brightness cannot be higher than that of the present electron gun, using a fiber should simplify the gun alignment procedure and maybe allow for a better electron beam quality (for instance a less astigmatic spot size).

Finally a He cryostat will soon replace the LN_2 one, to perform experiments in the 10 K – 300 K temperature range.

A Algorithm for the diffusion model

This appendix is devoted to the algorithm developed to solve the equations system for the diffusion model. The algorithm was written and compiled in the MATLAB environment. Symbols used here are the same of section 5.5.1 with the following exceptions:

$I_{QWR} = L$
$I_{VQWR} = V$
$u(x,0) = \mathrm{f}$
l QWR lenght (nm)
T $[0, T(ps)]$ time interval that is simulated

% Program begins here %

$function[u, n, N, L, V] = Model(f, l, T, D, p, m, N_{sat}, \tau, \tau_1, \tau_2)$

% We define a function $Model$ of arguments $(f, l, T, D, p, m, N_{sat}, \tau, \tau_1, \tau_2)$ that returns the populations in the wires and the intensities emitted by them (u, n, N, L, V). %

```
$h = l/(p-1);$            % Spatial step %
$k = T/(m-1);$            % Temporal step %
$r = D * k/h^2;$
$b = c * k/h;$
$d = k/\tau_1;$
$o = k/\tau;$
$s = 1 - 2 * r - d;$
$a = 1 - o;$
$q = 1 - k/\tau;$
$u = zeros(n, m);$        % $u$ is a matrix $(nxm)$ initialized to zero %
$n = zeros(n, m);$        % $n$ is a matrix $(nxm)$ initialized to zero %
$N = zeros(1, m);$        % $N$ is a matrix $(1xm)$ initialized to zero %
$L = zeros(1, m);$        % $L$ is a matrix $(1xm)$ initialized to zero %
$V = zeros(1, m);$        % $V$ is a matrix $(1xm)$ initialized to zero %
```

% Carriers are generated in the reservoir %
$u(2 : n-1, 1) = feval(f, h : h : (n-2) * h)';$

```
% Boundary conditions: reflecting wall (at time zero) %
$n(1,1) = n(2,1);$

% Boundary conditions: absorbing wall (at every time) %
$n(p,1:m) = 0;$

% Electron-hole pairs eventually present in the VQWR when the next excitation pulse arrives onto the pyramid %
$N(1,1) = \mathbb{N}_0;$

$for\ j = 2:m$
$for\ i = 2:p-1$

% Carriers from the reservoir are trapped in the QWR %
$u(i,j) = a * u(i,j-1);$

% Carriers diffuse in QWR towards the central structures. (This is equation 5.13) %
$n(i,j) = s * n(i,j-1) + r * (n(i-1,j-1) + n(i+1,j-1)) + o * u(i,j-1);$

$end$        % first $for$ cycle%

% Boundary conditions: reflecting wall (at time j) %
$n(1,j) = n(2,j);$

% Rate equations for the VQWR population. (This is equation 5.9) %
$N(1,j) = q * N(1,j-1) + (1 - N(1,j-1)/N0) * b * U(p-1,j-1);$

% Fraction of carriers reflected back in the QWR %
$n(p-1,j) = n(p-1,j) + (N(1,j-1)/N0) * b * (n(p-1,j-1))/h;$

$end$        % second $for$ cycle %

$for\ j = 2:m$
$for\ i = 2:p-1$

% We compute the number of photons emitted by the QWR in the time interval $t, t+dt$ (This is equation 5.10) %
$L(1,j) = L(1,j) + U(i,j) * h * k/\tau_1;$

$end$        % first $for$ cycle%
```

```
$end$      % second $for$ cycle %

% We compute the number of photons emitted by the QWR in the time interval
$t, t + dt$ (This is equation 5.11) %
$V = N * k/\tau_2;$

  $u = u';$     % Matrix are transposed %
  $n = n';$
  $N = N';$
  $L = L';$
  $V = V';$


% End of the program %
```

B Complementary results for the diffusion model

In this section we report two other results relative to the diffusion model. First of all we show why we were forced to introduce the hypothesis of the VQWR saturation. If we run our algorithm by setting $N_{sat} \gg N_0$ (no saturation possible) we cannot fit the data relative to the excitation point located on top of the pyramid (fig. B.1). In this case we are not able to reproduce the intensities ratios observed in the QWR and in the VQWR temporal responses. Notice also that the decay time for the QWR is much faster than that we observe experimentally.

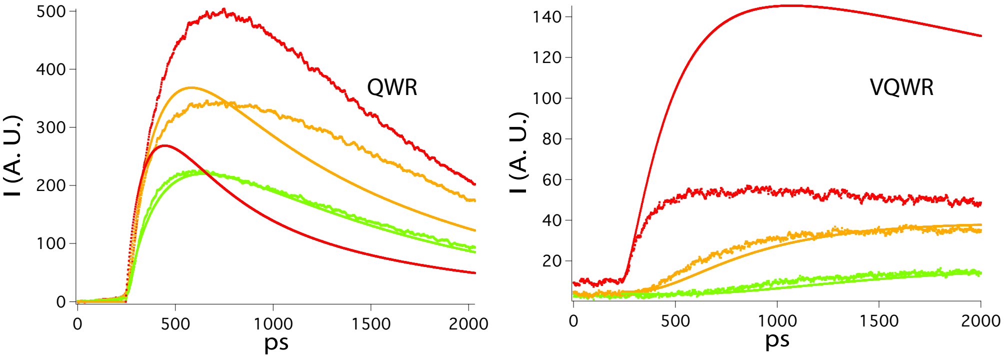

Figure B.1: We are forced to introduce the hypothesis that we saturate the VQWR in order to explain the temporal profile of the luminescence emission when we excite the top of the pyramid.

It is also interesting to compute the temporal profile of the luminescence for a time interval corresponding to the laser repetition rate (12 ns). In particular, in the case of one population dynamics, the subtraction of the mono-exponential signal, corresponding to the 6-8 ns temporal window, gives a non zero-intensity emission of the VQWR even after 12 ns. (At least in theory, this result is exact.) In our simulations the VQWR intensities at t =12 ns match those at t = 0 ns (fig. B.2).

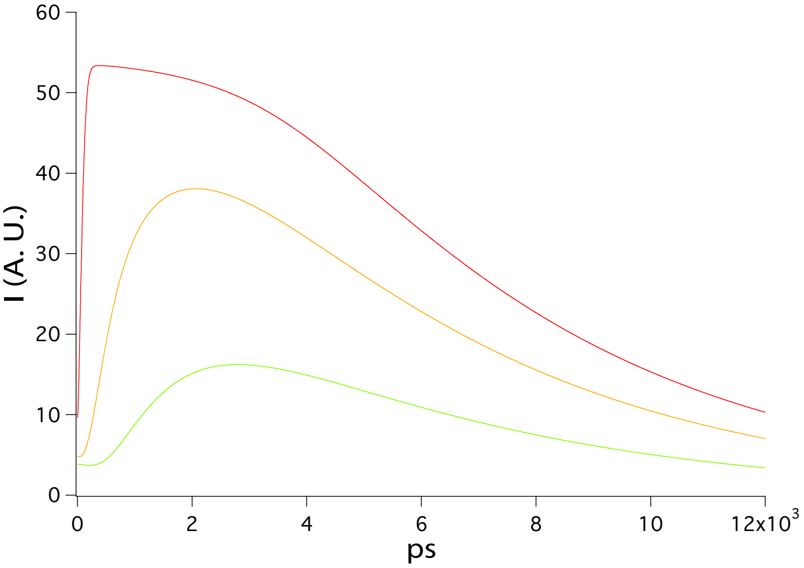

Figure B.2: Temporal profile of the VQWR luminescence over a period of the laser system.

References

[1] D. Bimberg, *Quantum Dot Heterostructures.* WILEY, first ed., 1999.

[2] A. Imamoglu *Physica E-Low-Dimensional Systems and Nanostructures*, vol. 16, no. 1, pp. 47–50, 2003.

[3] D. Loss and D. P. DiVincenzo *Physical Review A*, vol. 57, no. 1, pp. 120–126, 1998.

[4] I. Robert, E. Moreau, M. Gallart, J. M. Gerard, and I. Abram *Physica E-Low-Dimensional Systems and Nanostructures*, vol. 16, no. 1, pp. 51–58, 2003.

[5] O. Benson, C. Santori, M. Pelton, and Y. Yamamoto *Physical Review Letters*, vol. 84, no. 11, pp. 2513–2516, 2000.

[6] J. M. Gerard and B. Gayral *Journal of Lightwave Technology*, vol. 17, no. 11, pp. 2089–2095, 1999.

[7] A. Gustafsson, M. E. Pistol, L. Montelius, and L. Samuelson *Journal of Applied Physics*, vol. 84, no. 4, pp. 1715–1775, 1998.

[8] J. Shah, *Ultrafast Spectroscopy of Semiconductors and Semiconductor Nanostructures.* Springer, 1996.

[9] A. Bell, S. Srinivasan, C. Plumlee, H. Omiya, F. A. Ponce, J. Christen, S. Tanaka, A. Fujioka, and Y. Nakagawa *Journal of Applied Physics*, vol. 95, no. 9, pp. 4670–4674, 2004.

[10] S. Khatsevich, D. H. Rich, X. Zhang, W. Zhou, and P. D. Dapkus *Journal of Applied Physics*, vol. 95, no. 4, pp. 1832–1842, 2004.

[11] U. Vetter, H. Hofsass, and T. Taniguchi *Applied Physics Letters*, vol. 84, no. 21, pp. 4286–4288, 2004.

[12] F. A. Ponce, S. Srinivasan, A. Bell, L. Geng, R. Liu, M. Stevens, J. Cai, H. Omiya, H. Marui, and S. Tanaka *Physica Status Solidi B-Basic Research*, vol. 240, no. 2, pp. 273–284, 2003.

[13] C. Diaz-Guerra, J. Piqueras, A. Castaldini, A. Cavallini, and L. Polenta *Journal of Applied Physics*, vol. 94, no. 12, pp. 7470–7475, 2003.

[14] A. Urbieta, P. Fernandez, C. Hardalov, J. Piqueras, and T. Sekiguchi *Materials Science and Engineering B-Solid State Materials for Advanced Technology*, vol. 91, pp. 345–348, 2002.

[15] V. Turck, S. Rodt, R. Heitz, M. Strassburg, U. W. Pohl, and D. Bimberg *Physica Status Solidi B-Basic Research*, vol. 224, no. 3, pp. 643–647, 2001.

[16] T. Riemann, D. Rudloff, J. Christen, A. Krost, M. Lunenburger, H. Protzmann, and M. Heuken *Physica Status Solidi B-Basic Research*, vol. 216, no. 1, pp. 301–305, 1999.

[17] D. H. Rich, Y. Tang, A. Konkar, P. Chen, and A. Madhukar *Journal of Applied Physics*, vol. 84, no. 11, pp. 6337–6344, 1998.

[18] Y. L. Khong, A. T. Collins, and L. Allers *Diamond and Related Materials*, vol. 3, no. 7, pp. 1023–1027, 1994.

[19] B. G. Yacobi and D. B. Holt, *Cathodoluminescence Microscopy of Inorganic Solids.* Plenum Press, first ed., 1990.

[20] L. Reimer, *Scanning Electron Microscope.* Springer-Verlag, first ed., 1985.

[21] D. Bimberg, H. Munzel, A. Steckenborn, and J. Christen *Physical Review B*, vol. 31, no. 12, pp. 7788–7799, 1985.

[22] D. Bimberg, J. Christen, A. Steckenborn, G. Weimann, and W. Schlapp *Journal of Luminescence*, vol. 30, no. 1-4, pp. 562–579, 1985.

[23] G. Mourou and S. Williamson *Applied Physics Letters*, vol. 41, no. 1, pp. 44–45, 1982.

[24] H. Ihee, V. A. Lobastov, U. M. Gomez, B. M. Goodson, R. Srinivasan, C. Y. Ruan, and A. H. Zewail *Science*, vol. 291, no. 5503, pp. 458–462, 2001.

[25] J. C. Williamson, J. M. Cao, H. Ihee, H. Frey, and A. H. Zewail *Nature*, vol. 386, no. 6621, pp. 159–162, 1997.

[26] H. E. Elsayedali and G. A. Mourou *Applied Physics Letters*, vol. 52, no. 2, pp. 103–104, 1988.

[27] H. E. Elsayedali and J. W. Herman *Review of Scientific Instruments*, vol. 61, no. 6, pp. 1636–1647, 1990.

[28] M. Aeschlimann, E. Hull, J. Cao, C. A. Schmuttenmaer, L. G. Jahn, Y. Gao, H. E. Elsayedali, D. A. Mantell, and M. R. Scheinfein *Review of Scientific Instruments*, vol. 66, no. 2, pp. 1000–1009, 1995.

[29] S. H. Kong, J. Kinrosswright, D. C. Nguyen, and R. L. Sheffield *Nuclear Instruments and Methods in Physics Research Section a-Accelerators Spectrometers Detectors and Associated Equipment*, vol. 358, no. 1-3, pp. 272–275, 1995.

[30] S. H. Kong, J. Kinrosswright, D. C. Nguyen, R. L. Sheffield, and M. E. Weber *Nuclear Instruments and Methods in Physics Research Section a-Accelerators Spectrometers Detectors and Associated Equipment*, vol. 358, no. 1-3, pp. 284–286, 1995.

[31] P. May, J. M. Halbout, and G. Chiu *Applied Physics Letters*, vol. 51, no. 2, pp. 145–147, 1987.

[32] T. Srinivasanrao, J. Fischer, and T. Tsang *Journal of Applied Physics*, vol. 69, no. 5, pp. 3291–3296, 1991.

[33] T. Anderson, I. V. Tomov, and P. M. Rentzepis *Journal of Applied Physics*, vol. 71, no. 10, pp. 5161–5167, 1992.

[34] R. H. Fowler *Physical Review*, vol. 38, no. 1, pp. 45–56, 1931.

[35] L. A. DuBridge *Physical Review*, vol. 43, no. 9, pp. 727–741, 1933.

[36] O. Klemperer, *Electron Optics.* Cambridge University Press, third ed., 1971.

[37] D. B. Langmuir *Proceedings of the Institude of Radio Engineers*, vol. 25, no. 8, pp. 977–991, 1937.

[38] P. Grivet, *Electron optics.* Pergamon Press, second ed., 1972.

[39] E. M. Purcell, *Electricity and Magnetism*, vol. 2 of *Berkeley physics course.* mcgraw-hill, 1965.

[40] M. E. Haine and P. A. Einstein *British Journal of Applied Physics*, vol. 3, no. FEB, pp. 40–46, 1952.

[41] M. Futamoto, M. Nakazawa, K. Usami, S. Hosoki, and U. Kawabe *Journal of Applied Physics*, vol. 51, no. 7, pp. 3869–3876, 1980.

[42] H. Ahmed and A. N. Broers *Journal of Applied Physics*, vol. 43, no. 5, p. 2185, 1972.

[43] D. W. Tuggle and L. W. Swanson *Journal of Vacuum Science and Technology B*, vol. 3, no. 1, pp. 220–223, 1985.

[44] L. Reimer, *Transmission Electron Microscopy.* Springer-Verlag, fourth ed., 1997.

[45] F. Füzesi, "Projet de cathodoluminescence résolue en temps: validation de l'appareillage expérimental, en mode continu, sur des structures de gan," tech. rep., EPFL, 2004.

[46] F. Bertram, T. Riemann, J. Christen, A. Kaschner, A. Hoffmann, K. Hiramatsu, T. Shibata, and N. Sawaki *Materials Science and Engineering B-Solid State Materials for Advanced Technology*, vol. 59, no. 1-3, pp. 117–121, 1999.

[47] M. H. Baier, S. Watanabe, E. Pelucchi, and E. Kapon *Applied Physics Letters*, vol. 84, no. 11, pp. 1943–1945, 2004.

[48] E. Kapon, E. Pelucchi, S. Watanabe, A. Malko, M. Baier, K. Leifer, B. Dwir, F. Michelini, and M. Dupertuis *Physica E*, vol. 25, pp. 288–297, 2004.

[49] E. Pelucchi, M. Baier, Y. Ducommun, S. Watanabe, and E. Kapon *Physica Status Solidi B-Basic Research*, vol. 238, no. 2, pp. 233–236, 2003.

[50] A. Hartmann, L. Loubies, F. Reinhardt, and E. Kapon *Applied Physics Letters*, vol. 71, no. 10, pp. 1314–1316, 1997.

[51] G. Biasiol and E. Kapon *Physical Review Letters*, vol. 81, no. 14, pp. 2962–2965, 1998.

[52] A. Hartmann, Y. Ducommun, K. Leifer, and E. Kapon *Journal of Physics-Condensed Matter*, vol. 11, no. 31, pp. 5901–5915, 1999.

[53] Y. Ducommun, *Semiconductor quantum dots grown in inverted pyramids.* PhD thesis, EPFL, 2001.

[54] K. Leifer, A. Hartmann, Y. Ducommun, and E. Kapon *Applied Physics Letters*, vol. 77, no. 24, pp. 3923–3925, 2000.

[55] D. Y. Oberli, M. A. Dupertuis, F. Reinhardt, and E. Kapon *Physical Review B*, vol. 59, no. 4, pp. 2910–2914, 1999.

[56] S. Chandrasekhar *Reviews of Modern Physics*, vol. 15, no. 1, pp. 1–87, 1943.

[57] F. Reif, *Statistical and thermal physics.* McGRAW-HILL, 1985.

[58] D. Kincaid and W. Cheney, *Numerical Analysis.* ITP, second ed., 1996.

[59] V. Emiliani, F. Intonti, C. Lienau, T. Elsaesser, R. Notzel, and K. H. Ploog *Physical Review B*, vol. 6415, no. 15, pp. art. no.–155316, 2001.

[60] S. Nakamura *Physics World*, vol. 11, no. 2, pp. 31–35, 1998.

[61] J. Menniger, U. Jahn, O. Brandt, H. Yang, and K. Ploog *Physical Review B*, vol. 53, no. 4, pp. 1881–1885, 1996.

[62] S. J. Tans, A. R. M. Verschueren, and C. Dekker *Nature*, vol. 393, no. 6680, pp. 49–52, 1998.

[63] F. Wang, G. Dukovic, L. E. Brus, and T. F. Heinz *Physical Review Letters*, vol. 92, no. 17, pp. –, 2004.

Publications and conferences

R. Bertacco, M. Merano, F. Ciccacci: "Spin dependent electron absorption in Fe(001)-p(1x1)O: a new candidate for a stable and efficient electron polarisation analyser." Appl. Phys. Lett. Vol. 72, 2050, (1998).

M. Merano, P. Renucci, J. D. Ganière, B. Deveaud-Pledran, "Picosecond Cathodoluminescence" Ultrafast processes in solid state nanostructures, Les Houches 2002, France. Talk.

M. Merano, P. Renucci, J. D. Ganière, B. Deveaud-Pledran, "Laser-driven metal photocathodes for picosecond time resolved cathodoluminescence" JMM Joint Microscope Meeting, Lille 2002, France. Talk.

M. Merano, S. Collin, P. Renucci, M. Gatri, J. D. Ganière, B. Deveaud-Pledran, "Picosecond Cathodoluminescence" Ultrafast Science with X-Rays and Electrons Montreux 2003, Switzerland. Poster.

M. Merano, S. Collin, P. Renucci, M. Gatri, J. D. Ganière, B. Deveaud-Pledran, "Picosecond Cathodoluminescence" Quantum State Engineering and Ultrafast Optical Interactions in Semiconductors, Toledo 2003, Spain. Talk.

M. Merano, S. Collin, P. Renucci, M. Gatri, S. Sonderegger, A. Crottini, J. D. Ganière, B. Deveaud-Plédran, "Picosecond Cathodoluminescence" Annual meeting of the Swiss Physical Society, Neuchatel 2004, Switzerland. Talk.

Ferenc Füzesi, Denis Martin, Jérôme Napierala, Michele Merano, Andrea Crottini, Samuel Sonderegger, Jean-Daniel Ganière, Marc Ilegems, Benoît Deveaud-Plédran, "Cathodoluminescence observation of GaN defects on layers grown by HVPE" Annual meeting of the Swiss Physical Society, Neuchatel 2004, Switzerland. Poster.

Curriculum Vitæ

MICHELE MERANO

Date of birth	:	February 28, 1972
Nationality	:	Italian

2001– 2004	Ph.D. student at the Institute of Quantum Electronics and Photonics, École Polytechnique Fédérale de Lausanne (EPFL).
05-12 2000	Stage at Biomedical photonics group DMT - EPFL in microarray technology.
02-04 2000	Stage at Università degli studi di Pavia on material science.
1991–1998	Bachelor and Master Degree (Laurea) in Physics Final mark 110/110 summa cum laude.
June 1991	Secondary School Diploma (Maturità Scientifica) Final mark 60/60